FEASIBILITY STUDY TO DETERMINE METHODS OF MEASURING THE TEMPERATURE OF A MOLECULAR BEAM

By J. E. Hueser and P. Fowler

FINAL REPORT

Prepared Under Contract No. NAS1-8223-2
NORTON RESEARCH CORPORATION
Cambridge, Massachusetts
for
NATIONAL AERONAUTICS AND SPACE ADMINISTRATION

ERRATA

Final Report
Contract NAS1-8223-2

FEASIBILITY STUDY TO DETERMINE METHODS OF MEASURING THE TEMPERATURE OF A MOLECULAR BEAM

By J. E. Hueser and P. Fowler
October 27, 1970

Title Page: Upper right hand corner, CR-66950

Page 14: Section 2.2.1 - line 4 "...of final energy states or electronic".

Page 27: Line 12 "... that of the $B^3\pi_g$ maximum, ...".

Page 50: Line 3 "...kinetic emission, ...".

Page 56: Second paragraph - line 18 "... or both. The resonance...".

Page 59: Last line "... can extrapolate the exponential decay...".

Page 63: Second paragraph - line 6 "... beam can be described in...".

Page 68: Line 20 "... to the metastable state is $U\Delta t_e$, where...".

Page 85: Footnote section - line 3 "... from the true mean for...".

Page 88: Equation (3.1.3-7) should read:

$$[\dot{dN}(t)]_{max} = \frac{i_e}{e\pi^{3/2}} n\sigma K\gamma\lambda_e \Delta t_e \rho d\omega \frac{S^3 U}{\ell (1 - 8/S^2)} e^{-4/S^2} dt \qquad (3.1.3\text{-}7)$$

Page 90: Equation (3.1.3-8) should read:

$$[\dot{dN}(t)]_{max} = 1.25 \times 10^5 \text{ counts/sec.} \qquad (3.1.3\text{-}8)$$

TABLE OF CONTENTS

TABLE OF CONTENTS (CONT.)

TABLE OF CONTENTS (CONT.)

LIST OF FIGURES

LIST OF FIGURES CONT.

LIST OF FIGURES CONT.

LIST OF FIGURES CONT.

LIST OF TABLES

FEASIBILITY STUDY TO DETERMINE METHODS OF MEASURING THE TEMPERATURE OF A MOLECULAR BEAM

By J.E. Hueser and P. Fowler
Norton Research Corporation

SUMMARY

A basically different approach to the measurement of planetary atmospheric parameters, for example, the temperature of the Earth's thermosphere, is presented. The measurement utilizes a molecular beam sampling inlet together with techniques for establishing the temperature based on the properties of the beam. The choice of a particular instrument geometry as well as the selection of specific experimental apparatus are discussed in relation to three detection systems: 1) the metastable time-of-flight, 2) the flux angular distribution, and 3) the retarding potential energy distribution analysis techniques.

Theoretical predictions are presented for the measurement sensitivity of the detection systems as well as discussions of simultaneously occurring noise signals, for example, the signals due to photon flux and neutral background flux. Data are presented for computer calculations of the theoretically predicted signal, which indicate that temperature measurements are possible at atmospheric densities of 10^{10} cm^{-3} which corresponds to measurements in the thermosphere at an altitude of about 170 km.

It is concluded that the results are sufficiently encouraging that experimental verification under simulated conditions of the high speed probe be undertaken.

1. INTRODUCTION

Thermospheric neutral gas molecular temperatures have been established from analyses of satellite and rocket-borne mass spectrometer data in either of two ways:

1) from analysis of the amplitude modulation of the density of one of the atmospheric constituents in a cavity, alternately experiencing ram and wake entrance conditions due to the spin of the instrument, or

2) from a comparison of the measured density versus altitude to that obtained theoretically by integrating the hydrostatic equation for an ideal gas in equilibrium.

In the latter case, determination of the actual temperature distribution requires either assuming a value of the temperature at some altitude or comparing the density gradient for several assumed temperatures to an accepted model of the atmosphere, or a combination of both. These methods suffer from errors due to horizontal gradients, effects caused by departure of the profiles from those corresponding to the assumed model, and to non-equilibrium effects.

In the former case, the temperature distribution is derived by comparing the measured cavity density with that expected for a cavity, usually having an ideal aperture entrance, moving with known speed and angle of attack through a Maxwellian gas.

Temperature measurements inside a cavity with a small entrance orifice have been discussed by Schultz, Spencer and Reifman (ref. 1) and by Patterson (ref. 2). Analyses of density measurements made with semi-open mass spectrometer ion sources have been presented by Hedin, et.al. (ref. 3) and by Niemann and Kreick (ref. 4). Nier, et.al. (ref. 5) and Hedin and Nier (ref. 6) have discussed the method of deriving temperature from knowledge of the density variation with altitude.

In the case of density measurements with a nearly closed cavity, the molecular flux comes into temperature equilibrium with the cavity walls. For measurements with a semi-open type ion source, there is partial accommodation of the molecules with the ion source surfaces; the gas-surface interaction varying from one gas to another in a way that is not, at present, well understood. Niemann and Kreick (ref. 4) have defined and analyzed six different input contributions of molecules to the mass spectrometer ion current. Their analysis indicates, for large instrument speeds relative to the atmospheric thermal molecular speeds, that the number of molecules ionized in a semi-open source which have not experienced a previous surface collision is negligible compared with those that have had at least one surface collision.

Because of the uncertainty in the prediction of the gas-surface interaction processes, coupled with the high probability for surface collisions in the ion source and the requirement for assuming an atmospheric model or a boundary temperature to derive atmospheric temperature from density data, it is advantageous to explore other techniques for gas sampling and atmospheric temperature measurement. In a previous feasibility study on

methods of sampling planetary atmospheres (ref. 7), it was concluded that the method which avoided most of the above problems utilized an inlet which provided the sample in the form of an unscattered molecular beam.

In this report, discussions will be presented of three methods for determining the atmospheric temperature based on measurements utilizing a molecular beam inlet system:

- The first technique discussed is the metastable time-of-flight (MTOF) detection system, in which the temperature is derived from comparisons of the measured TOF signal wave form with that predicted from theoretical considerations of the drifting Maxwellian velocity distribution.

- The second method is based on the measurement of the spatial distribution of the molecular flux transmitted through the inlet system.

- The third method is based on the measurement of the energy distribution of the transmitted molecular flux using a retarding potential ion energy analyzer.

Although no actual flight data was found, similar techniques to the ones to be discussed have been proposed for measuring the temperature in the Earth's atmosphere. For example, a method utilizing the time-of-flight measurement was proposed in 1963 by Leonas (ref. 8) and later by Locke and French (refs. 9 and 10) in 1966 and 1969; a method based on the flux distribution has been proposed by UTIAS (ref. 11) and, although not proposed for a flight experiment, the retarding potential ion energy analyzer has been used by Heil and Scott (ref. 12) to measure the temperature of ion beams.

2. GENERAL STATEMENT OF THE PROBLEM

Having established that a beam experiment is to be preferred over the ram probe (thermal equilibration volume), it is appropriate to discuss, in general terms, a typical experimental arrangement. Presented in Fig. 1 is a schematic representation of a typical flight experiment showing the three main sections of the temperature measurement portion of the total instrument package. There will, of course, be additional instrumentation (such as electronics, pumps, telementry) complementing this measurement as well as additional apparatus for the measurement of necessary auxiliary parameters for the final determination of the temperature. These will include instruments to determine the vehicle speed, angle of attack, density, and composition.

The temperature measurement apparatus is composed of three main sections: 1) the inlet, which provides a collimated beam of neutral atmospheric molecules, 2) the interaction region, which is the source of excited or ionized particles to be used in the identification, analysis and discrimination process, and 3) the detector, which, together with the necessary electronics, converts the incident flux of particles from the source into an identifiable signal which is later transmitted to Earth for analysis.

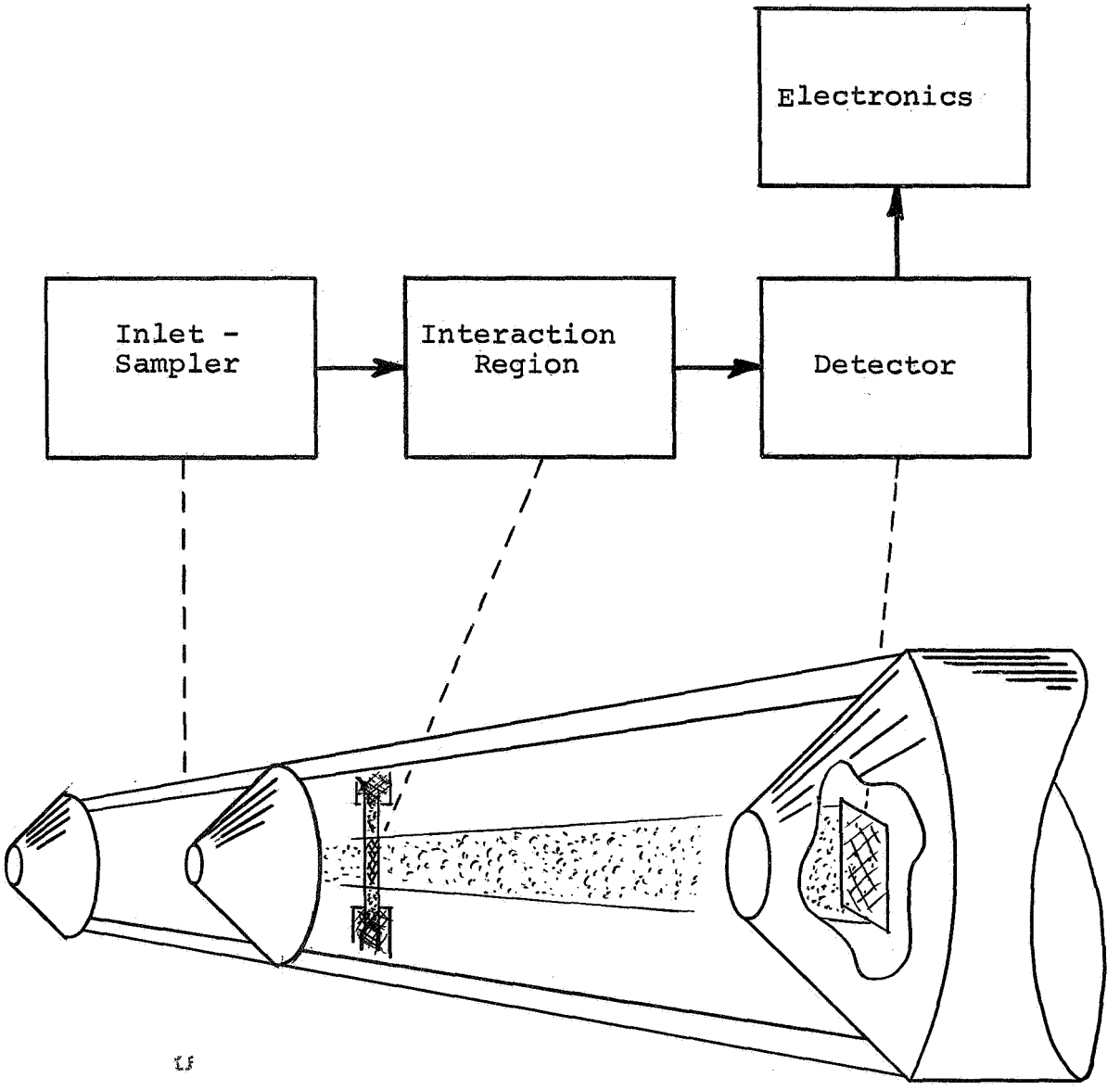

Fig. 1.- Schematic representation of a typical flight experiment.

In considering these three major divisions, emphasis will be placed on discussions of processes occurring in the interaction region and at the detector; the inlet will be considered with less detail, since it was evaluated in a previous report (ref. 13). Discussion of the detection and transmission electronics will be deferred until the detection scheme has been more selectively defined.

Since all of the measurement schemes have one component in common, the molecular beam forming inlet, the pertinent properties and operating conditions appropriate to the inlet will be described first and then the assumed conditions on which the calculations and discussions of the various detection system sensitivities are based will be presented.

2.1 INLET SYSTEM

2.1.1 General Discussion of a Low Density Beam Forming Inlet System

The geometrical dimensions and the design considerations which are incorporated in the choice of a sampling system are influenced rather strongly by the range of densities to be encountered and the range of speed ratios (this parameter being influenced both by the range of gas temperatures and vehicle speeds). After consideration of these multiple requirements and in an attempt to satisfy the operating conditions of the majority of the anticipated systems, it has been concluded that the most appropriate inlet system would consist of a number of thin conically shaped collimators, rigidly positioned

into a coaxial assembly by support webs as shown schematically in Fig. 1. This type of inlet was chosen because the majority of the measurements are to be made at rather low density and it will, therefore, be required that the inlet diameter be large so that a measurable total flux enters the system. The use of a tube or bundle of tubes for the inlet (considered as the appropriate inlet for the measurement discussed in refs. 7 and 13) is inappropriate in the case of a large diameter inlet because as the inlet diameter increases, at fixed length-to-diameter ratio, the attenuation of the primary flux increases due to the longer path length the molecules must travel through the diffuse scattered gas contained inside a tube. Therefore, the tube has been rejected in favor of a series of "orifices". In the case of the conical shaped skimmers, the majority of the gas which would have made up the diffuse gas density in the tube has either passed directly or has been deflected into the atmosphere through the aft facing annular shaped ducts. However, it is to be emphasized that, even though this type of inlet system will be assumed and discussed quite freely throughout this report, the final choice of the geometrical dimensions and configurations will be dictated by the specific requirements of the experiment selected.

2.1.2 Specific Properties Of The Inlet System

2.1.2.1 Collimation.- The inlet system described above provides a collimated, unscattered, free-molecular beam of neutral molecules entering the analysis section of the probe. The collimation is both necessary and expedient. It is necessary in order to reduce the required instrument cavity active pumping, an operation which is performed to avoid the at-

tenuation of the primary beam which would otherwise occur in passing through the rather dense scattered background gas. It is expedient because the flux which has been stripped away would be ineffective in the measurement, since it represents flux passing through the inlet orifice into solid angles greater than that subtended by the detector. The collimation, on the other hand, reduces the total system sensitivity since it requires physical separation of the inlet and the interaction region and it also limits the measurements to angles of attack which are less than the plane half angle corresponding to the solid angle subtended by the detector.

2.1.2.2 Angle of attack.-The trade-offs between the need to improve the collimation of the molecular beam and the desire to maintain a large total flux and, thence, signal will depend upon the detection system chosen and the conditions of the experiment to be performed. For the detection systems to be discussed, the measurement capability depends, in part, on the velocity of the vehicle relative to the stationary gas, and in the case of a high relative velocity there is a concentration of the transmitted flux along the axis of the vehicle velocity vector. It is, therefore, necessary that the instrument axis coincide with the vehicle velocity vector (i.e., zero angle of attack) if the signal is to be maintained at a measurable level. For those systems, such as the MTOF detection system, which utilize axial detectors subtending a small solid angle, the signal rapidly decreases as the angle of attack increases; and when the angle of attack exceeds the maximum transmission angle of the inlet system (approximately

14° for the inlets discussed in this report), the transmitted flux goes to zero. In addition, the openness of the venting ducts between the conical collimators permits exterior molecular flux to enter the instrument region as the angle of attack is increased. For these reasons, it is desirable that the angle of attack be maintained near zero and it will be assumed in further discussions that it is zero.

2.1.2.3 Flow properties. - The fact that the density remains quite low over the entire measurement range and also that the inlet is formed from a series of collimating orifices has reduced the calculation of transmission probability of the primary flux to evaluations of the geometrical transmission function. As pointed out by Ivanovskii (ref. 14), there is a rather strong radial dependence in the distribution of the primary flux (or density) for small values of L/D, as well as the axial variation which has a specific dependence upon the speed ratio $(S = U/v_m)$. However, as L/D increases (the solid angle subtended by the detector becomes smaller), the radial flux distribution for the detector solid angle becomes uniform. Nevertheless, there is still a strong radial dependence for larger solid angles even at large values of L/D, as will be pointed out in section 3.2. The expression derived by Ivanovskii for the axial density (n_1), due to the flux transmitted through a tube, as a function of the transmission angle $\theta_o (\theta_o \equiv \tan^{-1} R/L)$ and the speed ratio S $(S \equiv U/v_m)$, in terms of the atmospheric density (n_o), is:

$$n_1 = \frac{n_o}{2}\left\{1 + \mathrm{erf}(S) - \cos\theta_o\left[1 + \mathrm{erf}(S\cos\theta_o)\right]\exp - (S^2\sin^2\theta_o)\right\} . \qquad (2.1.2\text{-}1)$$

Data has also been generated (see ref. 13) for the geometrical transmission function using the approximations that $S^2 > 10$ and $\tan\phi \approx \sin\phi \approx \phi$, where $\phi \equiv \tan^{-1} D/L$. In this case,

$$T_g\ (S,X) \approx \left\{1 - \frac{4}{\pi}\int_o^{X^{-1}} X'\ e^{-S^2\phi^2}\ (1 - X'^2\phi^2)^{\frac{1}{2}}\ d\phi\right\} \qquad (2.1.2\text{-}2)$$

where $X \equiv L/D$. Presented in Fig. 2 are the data for the variation of the axial density normalized with respect to the undisturbed atmospheric density as a function of the separation from the inlet orifice expressed in terms of L/D. Curves for various values of S have been presented. The data presented are both that of Ivanovskii and also of the geometrical transmission function.

2.2 INTERACTION REGION

Having established the means for providing a sample of the atmosphere for analysis which has the same properties as the undisturbed atmosphere, it is appropriate to ask the question: What measured, temperature dependent parameter will yield an accurate determination of the gas temperature and yet will retain sufficient sensitivity for measurement over a significant range of densities? This inquiry is the basis of this feasibility study and the answer will provide the necessary directives for the design of an appropriate experimental apparatus for the measurement of this parameter. However, this choice is

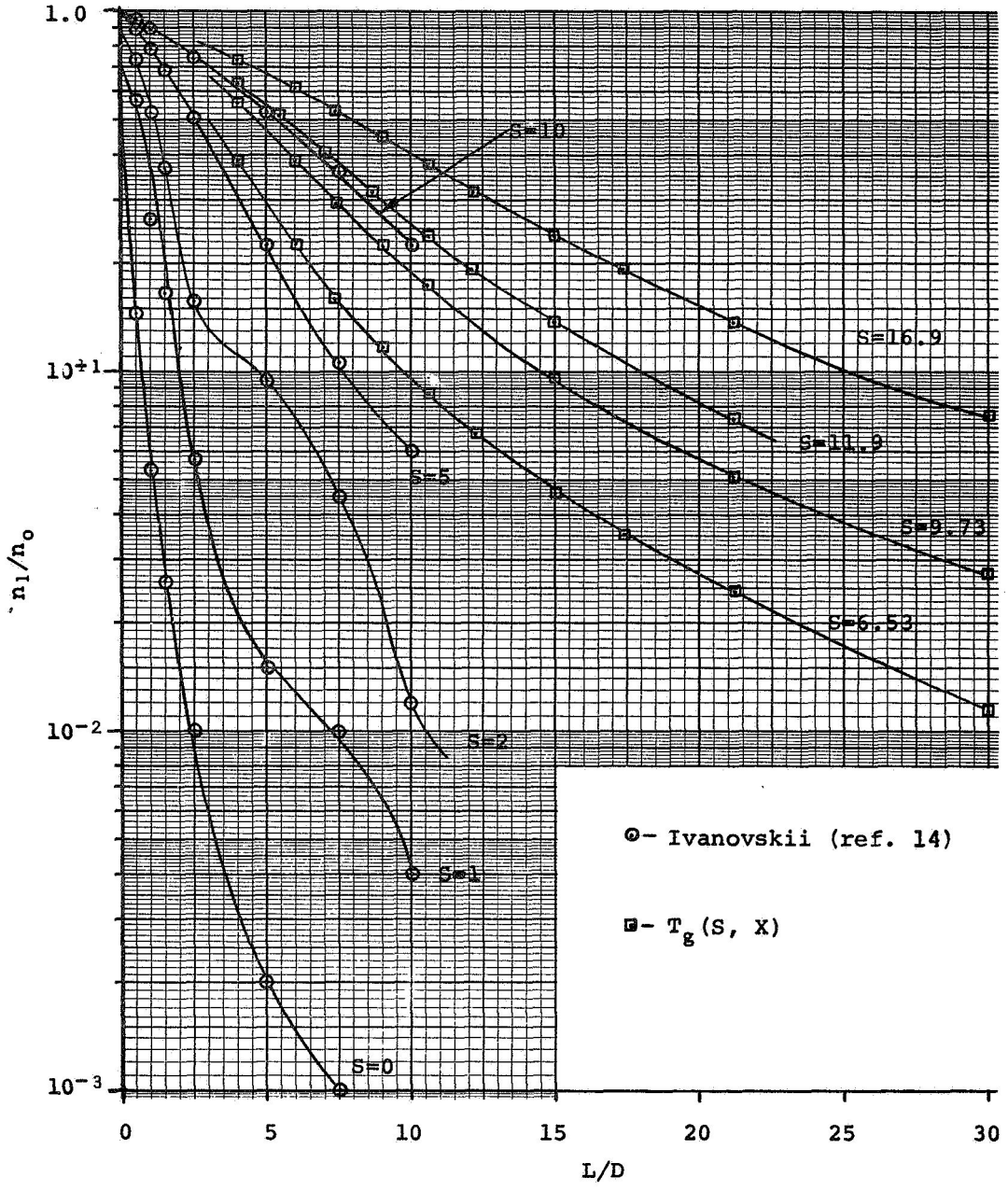

Fig. 2.- Normalized axial density vs length-to-diameter ratio.

not a straightforward elimination process because the measurement is to be made from a high speed vehicle (either a rocket, satellite, or entry probe). This relative motion imparts a high velocity bias to the particle energy or momentum and, therefore, the selection process is reduced to a relative evaluation of methods for separating this vehicle velocity bias from the molecular parameters or making the temperature measurement in terms of the dynamic flow properties of the gas which arise, in part, as a result of the velocity bias.

The flux which has passed through the inlet-sampling system enters the instrument cavity as a collimated beam of neutral particles. It has been assumed that some mechanism has been employed to remove the charged atmospheric species and that attempts have been made to minimize the photon flux so that the beam entering the instrument cavity is composed of ground state neutral molecular and atomic species (the primary Earth atmospheric constituents, for example, are atomic and molecular oxygen, molecular nitrogen, helium, and argon; the latter two being less than 1% of the total number density in the altitude range 120-300 km). Since it is not the primary purpose of this report to discuss the effects of different gas species, it will be assumed that the atmosphere is molecular nitrogen. In those cases where the gas species directly influences the particular result, the effects of gas composition will be considered in more detail.

The interaction region is considered as a spatially and temporally well-defined volume providing a source of particles whose physical characteristics are uniquely established and are directly related to measured system parameters. The interaction process provides the means of specifying the state of a

statistically representative fraction of the total number of particles which exist in the interaction volume at any instant in time. It is possible, therefore, with previous knowledge of this state of the particles which leave the interaction region, to select a suitable detector which can discriminate between the particles arriving on the basis of this known state. The choice of an experimental scheme which allows the necessary spatial definition and affords the means for specifying the state of the particles depends not only on the choice of the temperature dependent parameter and the ability of the experimental apparatus to accurately measure the parameter without introducing systematic errors but also depends, to some extent, on the suitability and applicability of the technique to flight hardware. It is, therefore, desirable to aim for compactness, simplicity, and ruggedness insofar as this can be achieved without sacrificing accuracy.

2.2.1 Interaction Processes

In most of the experimental measurements, the interaction process consists of some method of producing and specifying the final energy states of the emerging molecular or atomic particles. The three principal classes of final energy states or electro ic configurations to be discussed are ionic, radiating, and metastable. In the case of ion detection schemes, the fact that the particles are charged provides the necessary detection discrimination, and the internal energy of the particles is not of predominant importance; but in the other two cases, the internal energy state is the only means of discrimination. This imposes more stringent requirements on the detector and also on the source of excitation since energy spread becomes an important consideration. For example, in the case of a source with even minimal

energy spread, the number and the identity of excited states produced is difficult to predict because of uncertainties in the absolute energy of the electron source and because there are, in general, a number of energy levels whose spread is within the energy spread of the source. Additional discrimination is, therefore, necessary at the detector in order to isolate a particular energy state.

2.2.1.1 Photoexcitation.-Of those sources available which provide a method of producing excited or ionic energy states, the two most commonly used in low energy applications are electron impact excitation and photoexcitation, each having distinct advantages depending on the specific application. In those cases where resolution and precise energy definition are of primary consideration, photoexcitation is to be preferred because the source can be made nearly monoenergetic by using either narrow pass filters or a monochromator. It has been concluded, however, that the disadvantages are such that they exclude the use of a photoexcitation source. Some of these objections are listed below:

1. Photoproduction of metastable states can be accomplished only by second order phenomena such as radiationless collisional de-excitation or cascade transitions from upper allowed energy states. Therefore, the production efficiency is greatly reduced.

2. The efficiency of photoionization and photoexcitation is generally lower than that corresponding to the equivalent electron impact process. See Fig. 3, for example.

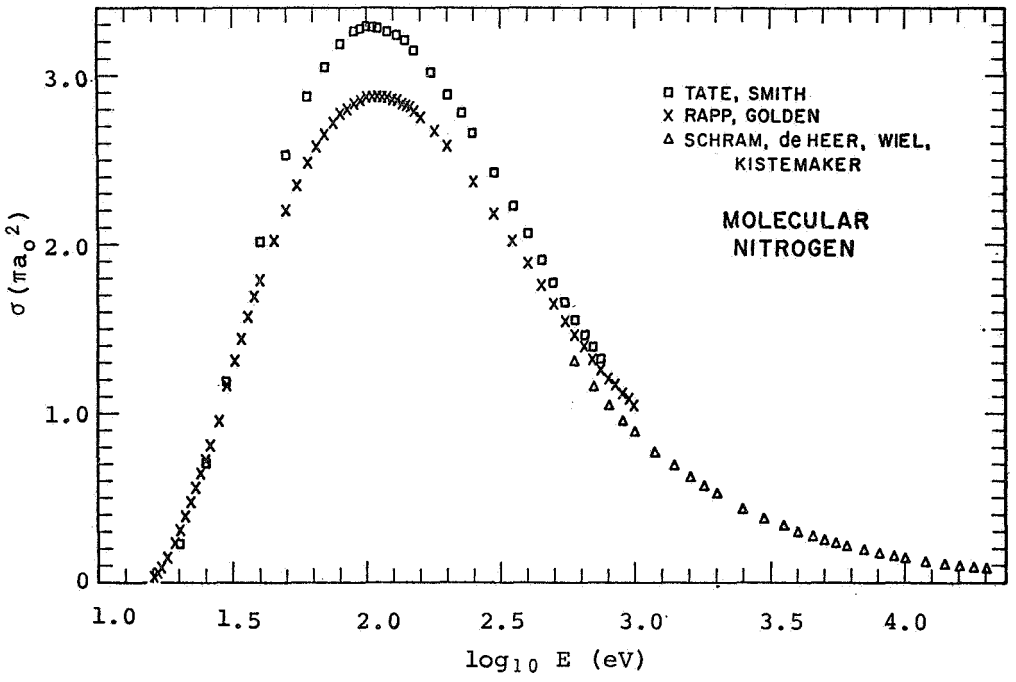

Total electron impact ionization cross section (ref. 15)

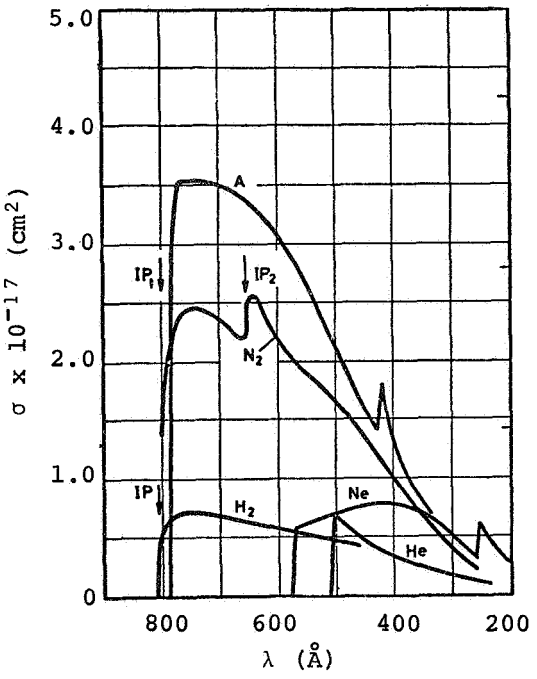

Photo-absorption cross-section (ref. 16)

Fig. 3.- Comparison of electron impact and photoionization cross-section.

3. For photoionization of the atmospheric gases, sources producing radiation in the wavelength region of 500-1000 Å are required. For the excitation of the lower lying radiating states, the source requirements are not quite so demanding; but the radiation necessary is generally still in the ultraviolet region. Sources of variable wavelengths in this region generally imply high pressure discharges and quartz or grating instruments. This fact, together with the inefficiency of such sources and the high power requirements make them unattractive for flight applications.

2.2.1.2 Electron impact excitation. - The use of electron impact ionization or excitation, on the other hand, should not be considered a secondary or alternate choice because of the nonapplicability of photoexcitation. It is, in fact, the most widely used and discussed method of investigating the structure and properties of atoms and molecules. In addition, it is more efficient, less demanding from an experimental standpoint, and is more suited to the specific requirements of the present problem, especially concerning the applicability to flight instrumentation. In considering the geometry of the electron impact source, it has been concluded, since a serious attempt has been made to avoid possible sources of scattering the primary beam of neutral particles which have passed through the probe up to this point, that the definition of the interaction region in terms of a volume whose spatial extent is determined by a grid structure, even though considered to be transparent, should be avoided. This motivation leads quite naturally to the choice

of a crossed-beam configuration. The geometrical configuration, operational parameters, and, in general, the detailed design of the electron source has not been attempted. However, some of the anticipated problems to be encountered in the design of the electron impact source are as follows:

1. The metastable source and detection system is critically affected by the operational parameters of the electron gun, since the requirements are for a low voltage, high electron flux density, minimal energy spread gun. These requirements tend to be mutually exclusive. Therefore, an appropriate balance must be achieved in the design of the source.

2. The measurement sensitivity of the detection systems is directly related to the electron flux density, so it is desirable to maximize this quantity.

3. The demands on the control of electron source parameters in the equivalent ion experiment are not so severe, since the energy definition is not as critical and the accelerating potential is considerably higher ($\approx$100 volts), thereby reducing the effects of electron space charge and increasing the electron flux density.

4. One of the necessary conditions for the meaningful prediction (and later, successful calibration and data correlation analysis) of the sensitivity and resolution of the measurements, as related to the

interaction processes, concerns the knowledge of the spatial extent or dimensions of the electron beam, having assumed that the neutral beam is well defined. In the calculations to be presented, it will be assumed that the electron beam is a parallel stream of monoenergetic particles. The extent to which this simplification can be approached in reality is largely a function of how well electronic space charge and energy spread can be controlled or suppressed.

2.2.1.3 Recoil effects. - In order to estimate the magnitude of the momentum recoil effects and the resulting perturbation of the molecular velocity distribution as a result of the electron impact excitation, calculations were made for the conditions of a high speed probe, assuming that the electron gun was operated near the threshold energy. Since the translational momentum of the neutral beam, in the case of a moving vehicle, is significantly increased in comparison with that of a thermal laboratory beam, the maximum recoil angle is reduced accordingly. It was concluded that the momentum recoil effects due to the electron impact excitation of the major atmospheric components of interest to this discussion are negligible, using the assumed parameters of the flight experiment to be discussed in section 3.

2.2.2 Products Resulting From The Interaction Process

As was mentioned earlier, the assumption has been made that the atmosphere is molecular nitrogen. In reality, the atmosphere to be probed is a multicomponent mixture and the separation of the components, so that a temperature measurement can be ac-

complished, is not a straightforward process. However, a complete discussion of a single component will display the relevant characteristics of the temperature measurement problem, and the extension of the analysis to include the other constituents can be made at a later time.

The main purpose of this section is to provide an estimate of the electron impact cross-section as a function of electron energy and of the lifetimes for those electronic energy states of molecular nitrogen which will enter into the measured signal at the detector. This data, when coupled with the detector sensitivity, will allow an estimate of the total detection system sensitivity at a specific electron energy. Since the electron impact cross-sections for the ionization of the atmospheric gases have been experimentally determined (see for example, Kieffer and Dunn, ref. 15), there is no need for additional discussion. This section will, therefore, consist of discussions concerning the electron impact cross-section for the production of neutral, excited energy states.

In order to maximize the signal, it is desirable to include as many of the electronic excited states as possible. However, in so doing, it must be established that those states included either radiate rapidly or are metastable (metastable in this context means that the lifetime is long compared to the flight time). The inclusion of excited states with intermediate lifetimes imposes a time dependence on the detector signal, since these molecules can arrive at the detector in the excited state or can radiate at some point along the flight path, depending on their velocity (distributed according to a Maxwellian distribution).

Since the total excitation cross-section as a function of electron energy is the parameter of interest, it is more appropriate to base the estimate of the cross-section on experimental results than to attempt an analytical solution, because complex cascade transitions become important as the electron energy is increased and there is little information available for the transition probabilities from the vibrational energy states. Towards this end, some of the experimental results of measured excitation functions for N_2 which have been established using the techniques of crossed-beam excitation and metastable detection will be evaluated. There are, however, significant differences between the excitation functions generally described in the literature and those to be expected in the flight measurement. Some will become evident as the results are presented; others will be discussed later.

Presented in Fig. 4 are some of the excitation functions for metastable molecular nitrogen beams which have appeared in the literature. These generally contain a variety of experimental conditions, a change in any one of which could cause noticeable differences in the data. The more important parameters are: 1) type of detector, 2) source conditions, such as electron energy spread, beam definition, beam density and electron flux density, 3) excitation source-to-detector separation, and 4) background effects.

A discussion of the detector sensitivity is contained in the following section of this report. However, it has also been discussed recently by Clampitt and Newton (ref. 20) and it is their conclusion that the secondary electron emission coefficient varies with the excitation energy of the interacting particle (in their case N_2 metastables), at least for a detector surface with an evaporated cesium layer. It can be postulated

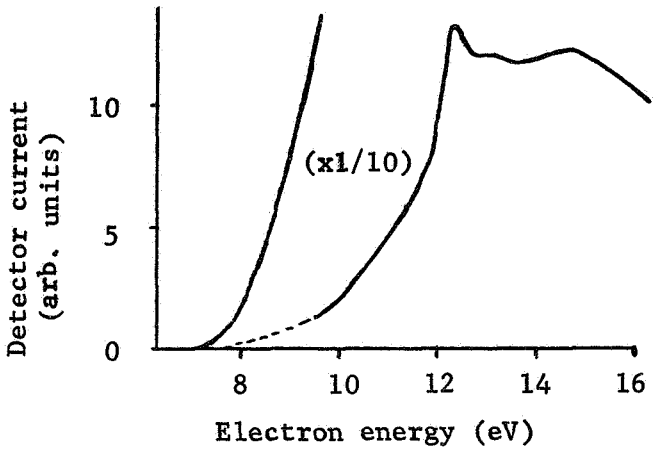

(a)

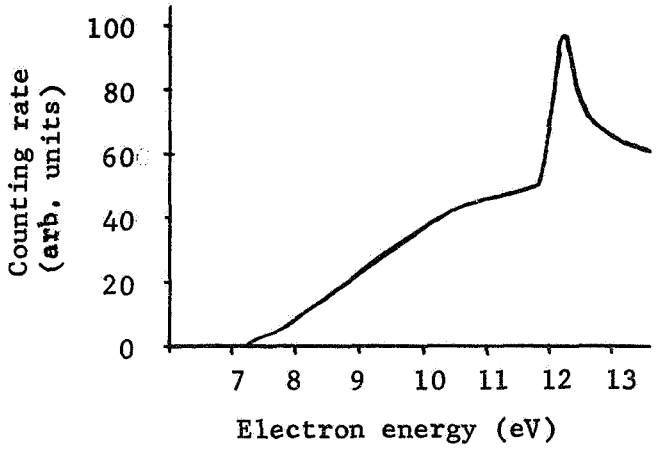

(b)

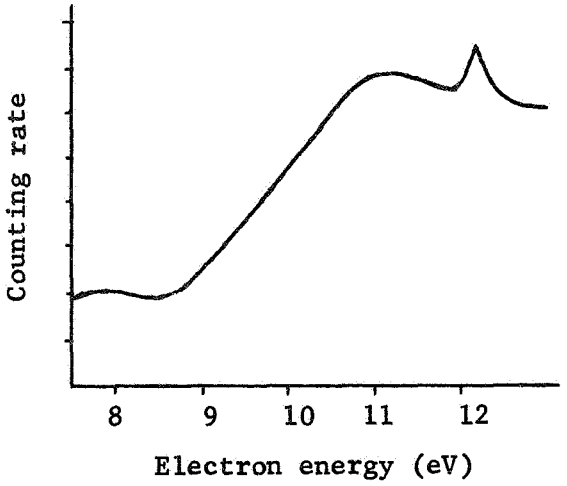

(c)

	Source - detector distance	Type of detector	Ref.
(a)	5 cm	Mg	17
(b)	22 cm	16 stage EM Ag-Mg cathode	18
(c)	- -	9 stage EM Cs_3Sb cathode	19

Fig. 4.- Excitation functions for metastable nitrogen (N_2) beams.

that similar differences could be caused by almost any film deposit or adsorbed gas layers. It is, therefore, quite difficult to correlate the literature data for excitation functions of N_2, since in no cases were procedures discussed for establishing or controlling the conditions of the detector surface.

In establishing the absolute cross-section, it is, of course, necessary to know and control the conditions in the source. The details of the source will not be discussed except to say that the parameters must be controlled and measured on an absolute basis, which is realized to be a difficult task. The electron energy spread probably affects the shape of the excitation function more than any other parameter, since it establishes the resolution which is attainable. Because of the energy spread, the peaks become blended into a generally smooth curve which results from the overlapping of the individual peaks (see the curves of Fig. 4).

One of the basic differences between the observed excitation curves derived in metastable time-of-flight systems is the excitation source-to-detector separation. If the source conditions are kept constant and the separation increased (average flight time increased), the effects of cascade from the radiating states to the metastable states is quite pronounced, since only the "long lived" states remain upon arrival at the detector. This effect has been demonstrated by Freund (ref. 21) and his results are presented in Fig. 5. Rather than change the separation, he has presented the excitation functions for various delay times after excitation. The features of these curves which affect the present discussions are the decaying peaks at 12.3 eV and 14.5 eV, which Freund associates with the $E^3 \Sigma_g^+$ and the $a^1\pi_g$ states, respectively. (The tail of the 500 μsec curve is due to He metastables, arising from the "seeded" beam

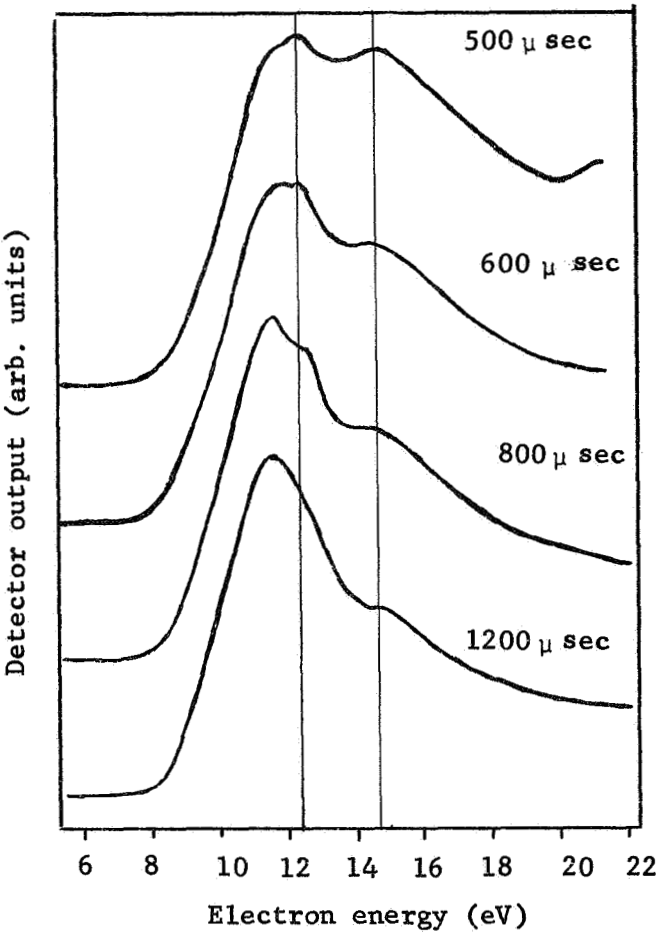

Fig. 5.- Variation of N_2 excitation functions with flight time (ref. 21).

used in the generation of this curve.) Since the radiative lifetimes of these states are considerably shorter than the minimum delay curve presented, it is probably safe to assume, for flight times much shorter than 500 μsec, that the structure will be dominated by these and possibly other "short lived" states. This, in fact, is the situation for the flight experiment, since the average flight time is of the order of tens of microseconds due to the velocity bias. This, of course, requires a redefinition of the meaning of metastable, since some of those states which are normally considered as radiating must now be considered as metastable.

Since there are no experimental data available to accomplish this extension of Freund's analysis, the discussion and conclusions will be based on those states which were predominant in his interpretation of the "normal" metastable excitation function, namely the $A^3\Sigma_u^+$, $B^3\pi_g$, $C^3\pi_u$, $E^3\Sigma_g^+$, and $a^1\pi_g$ states. Presented in Fig. 6 is a simplified energy level diagram for molecular nitrogen which shows the relative positions of these electronic energy states with respect to the ground state.

Freund's discussion and interpretation includes some of the above factors influencing the shape of the observed excitation functions. Based on his excitation functions derived from metastable detection, excitation functions derived from optical emission spectra (ref. 23), and knowledge of the lifetime of the states involved, he assigned specific energy states or cascade transitions to each of the observed peaks. These results, together with the apparent excitation cross-section measurements of Stanton and St. John (ref. 24) and those of Zapesochyni and Skubenich (ref. 25), allowed the estimate of the maximum value of the cross-section for the $B^3\pi_g$ and $A^3\Sigma_u^+$ states. Freund

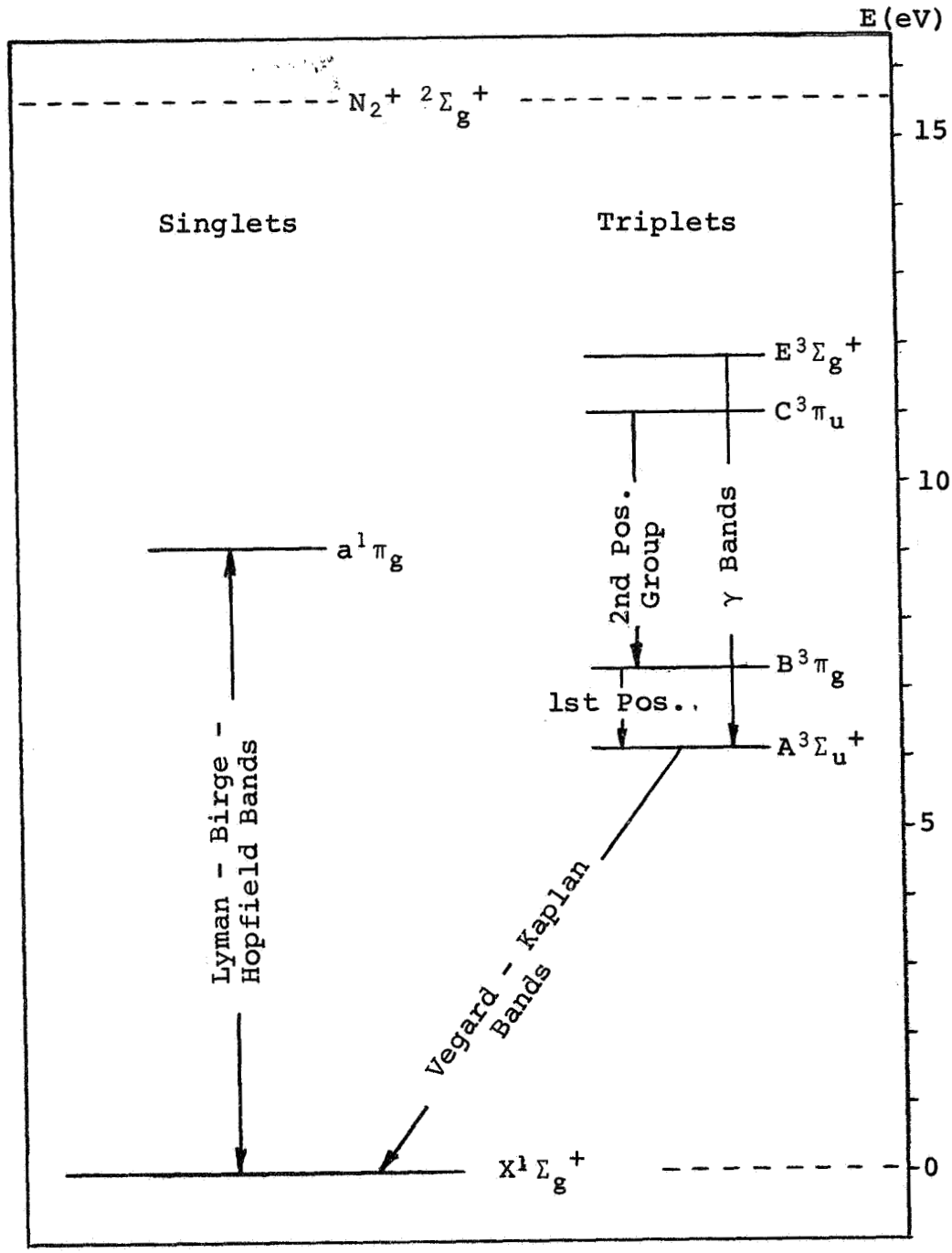

Fig. 6.- Energy level diagram for molecular nitrogen showing only the levels of interest (ref. 22).

concluded that the cross-sections are of the same order of magnitude and approximately equal to 10^{-16} cm^2. Presented in Table I are the pertinent data for the energy states of molecular nitrogen relevant to this analysis.

Since the $E^3\Sigma_g^+$ state has decayed substantially in the "normal" metastable detection system, it is difficult to assess the excitation cross-section for flight times appropriate to the flight detection system. The trapped electron excitation spectra of Rempt (ref. 27) have, therefore, been taken as an indication of the relative cross-section of the $E^3\Sigma_g^+$ and the $B^3\pi_g$ states. It is concluded that the cross-section for the $E^3\Sigma_g^+$ state is approximately twice that of the $B^2\pi_g$ maximum, the $E^3\Sigma_g^+$ state being a sharp resonant peak occurring at approximately 11.9 eV.

The apparent excitation cross-sections of the $B^3\pi_g$ and $C^3\pi_u$ states reported by Stanton and St. John (ref. 24), Zapesochyni and Skubenich (ref. 25), and McConkey and Simpson (ref. 28) are in fair agreement with those calculated by Green and Barth (ref. 29) and by Stolarski et. al (ref. 30). See Fig. 7. There is also partial confirmation of Stolarski's calculated cross-section for the $a^1\pi_g$ state by the high energy measurements of Holland (ref. 31).

Based on these experimental data for the excitation cross-sections and lifetimes of the predominant energy states of molecular nitrogen, the following observations with regard to the proposed metastable detection system can be made:

TABLE I

DATA FOR THE ELECTRON IMPACT EXCITATION OF N_2

ENERGY STATE	THRESHOLD ENERGY* (eV)	PEAK ENERGY** (eV)	LIFETIME	MAX. CROSS-SECTION ($\mathring{A}^2$)	REMARKS
$A^3\Sigma_u^+$	6.14	11.12	10-20 sec (a)	.4 (h)	calculated cross-section
$B^3\pi_g$	7.3	11	7 μsec (b)	.65 - 1.0 (d,e,f)	absolute cross-section based on optical emission spectra
$C^3\pi_u$	11.03	15	48 nsec (b)	.3 - .5 (d,e,f)	absolute cross-section based on optical emission spectra
$E^3\Sigma_g^+$	11.87	12.2	270±100 μsec (b)	$> \sigma(B^3\pi_g)$ - (g)	relative cross-section based on trapped electron spectra
$a^1\pi_g$	9.1	14.5	5-170 μsec (c)	.15 (h)	Holland estimates τ_{max} <80 μsec calculated cross-section

*data taken from ref. 30
**data taken from ref. 21

(a) see ref. 26
(b) see ref. 23
(c) see ref. 31
(d) see ref. 24
(e) see ref. 25
(f) see ref. 28
(g) see ref. 27
(h) see ref. 30

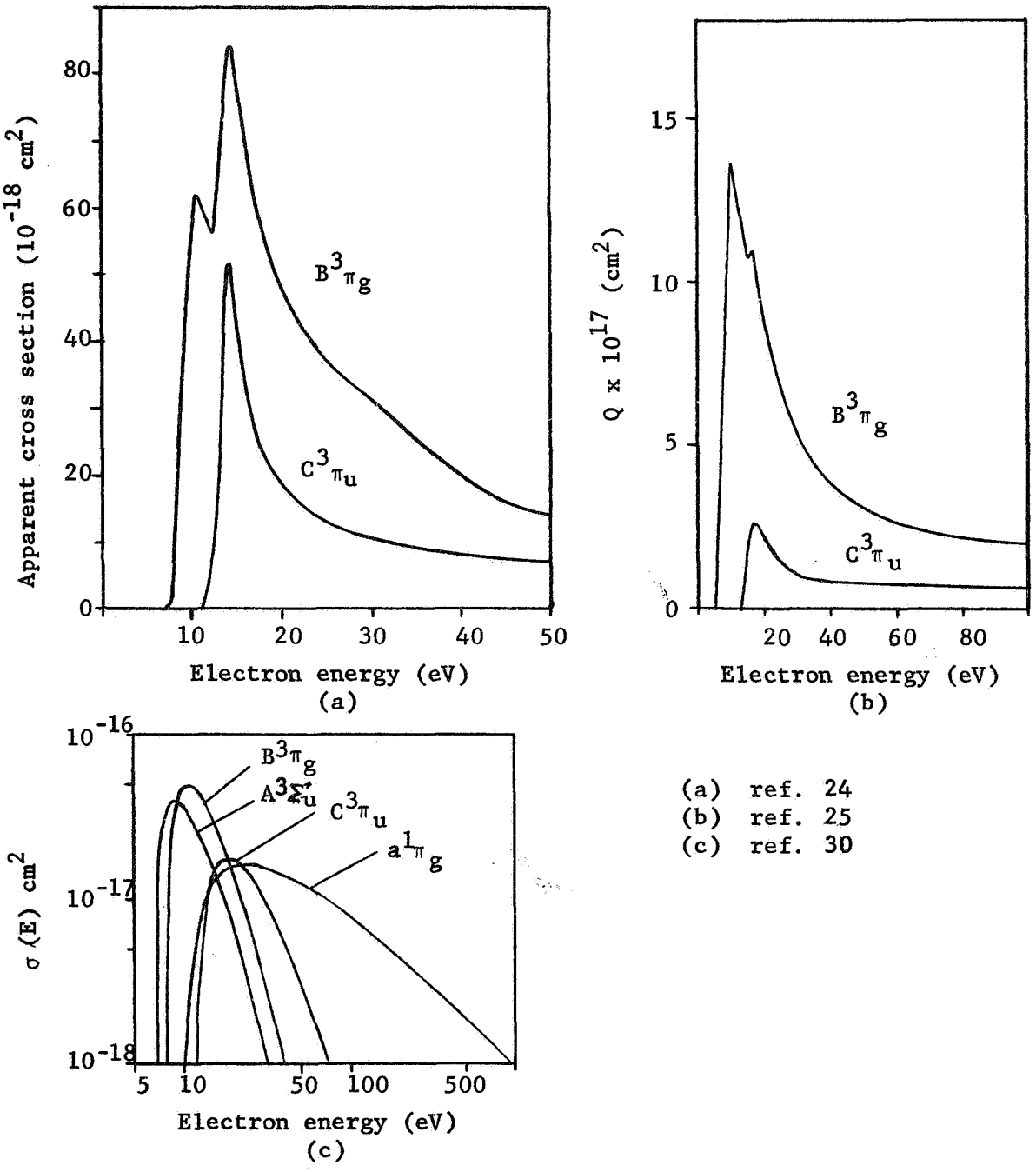

(a) ref. 24
(b) ref. 25
(c) ref. 30

Fig. 7.- Excitation cross-sections for molecular nitrogen.

1. Assuming that the average flight time is 30 μsec (the flight time depends primarily on the vehicle velocity), the $A^3\Sigma_u^+$, $E^3\Sigma_g^+$ and $a^1\pi_g$ states are metastable. The $C^3\pi_u$ state is a rapidly decaying peak which cascades into the $B^3\pi_g$ state. The $B^3\pi_g$ state is to be considered in the intermediate category; those molecules which radiate will contribute to the $A^3\Sigma_u^+$ state through cascade transitions.

2. Since the excitation cross-section of the $B^3\pi_g$ and $E^3\Sigma_g^+$ states are the greatest, it is appropriate to choose an electron energy which maximizes the two and, hence, the total excitation cross-section. The $E^3\Sigma_g^+$ being a resonant peak means that the electron energy should be peaked on it; thus, approximately 12 eV is the desirable value. This effectively reduces the population of the $C^3\pi_u$ state and, hence, reduces the photon flux.

3. The total excitation cross-section can be conservatively estimated as 5×10^{-17} cm^2, considering that the $B^3\pi_g$ state is a partially decaying state and also that there is some uncertainty in the cross-section of the $E^3\Sigma_g^+$ state.

2.3 DETECTOR

At this point in the generalized discussion of the apparatus, a sample of the undisturbed atmosphere has passed through the inlet system and with a suitable skimming process was formed into a well defined molecular beam. The resulting beam passed an inter-

action region, formed by the intersection of the neutral beam and the electron beam, which served to initialize or specify a state or parameter of a definite group of particles. The beam subsequently arrives at the detector. The purpose of the detector is to isolate and register the beam of particles according to a specific process, exclusive of all other competing processes. This discrimination is possible through the correct choice of the specified parameter and detection scheme.

For the present discussions, the topic to be considered is an evaluation of the secondary electron yield for the various combinations of particle-surface interactions together with the effects of adsorbate and angle of incidence on the yield. Since the estimated secondary electron yield and conditions affecting these estimated yields are of primary interest, it will be assumed that the detector consists of a simple target or electrode, knowing that in reality it will probably consist of a more complex geometry such as a shielded Faraday collector or an electron multiplier. The topics covered will be limited to discussions of metastable-surface interactions although competing processes, for example, photoemission and secondary electron emission due to neutral particle bombardment, will also be considered. Discussions of ion-surface interactions have been omitted, since in the usual ion detection scheme one is concerned only that the collection efficiency is such that all the ions are collected, the secondary electrons being suppressed by a small negative bias potential and other secondary processes being negligible for the ion energies of concern ($\approx$100 eV). Ion interaction processes will, however,

be included whenever they arise as a natural consequence of the other discussions, either directly or for comparison purposes. For a more complete discussion of these topics, see Kaminsky (ref. 32) or Krebs (ref. 33).

2.3.1 Secondary Processes

Quantitative experimental data for the secondary electron yield of incident metastable particles have been generated in experiments with noble gases on a variety of surfaces both in the "clean" condition and with specified adsorbed species. There is little data available for the evaluation of the equivalent experiment performed with the atmospheric gases. It is, therefore, possible only to establish estimates of the expected yields for the latter gases together with predictions of probable areas of concern.

A distinction must be made between two separate modes of producing secondary electrons. In one case, the energy transferred at the detector is provided by the translational kinetic energy of the incident particle; this is referred to as kinetic emission. In the other case, the energy transferred is supplied by the internal energy of excitation of the incident particle, no change in translational energy being necessary. This process is referred to as potential emission. In the following sections, 2.3.1.1 through 2.3.1.3, both the kinetic and potential emission process will be discussed in detail.

2.3.1.1 Auger Processes. - The process of de-excitation of metastables at the detector with the subsequent potential emission of secondary electrons can occur, on an energetic basis, in several different ways. In a collision of the first kind, in which energy is transferred to the metastable, the de-excitation process results in an upward transition to a radiating state followed by a transition to the ground state with the emission of a photon. Subsequent absorption of this radiation at the detector may cause electron ejection. The more probable process, both on a theoretical basis and as far as secondary electron emission is concerned, is a collision of the second kind in which the internal energy of the metastable is transferred (radiationless transitions) to the detector with the subsequent ejection of electrons. This electron emission process can result from two different transition mechanisms (Auger transitions), subject to the condition that the ionization energy of the incident particle is greater than the work function of the metal.

2.3.1.1.1 Auger de-excitation. - The first of these transitions is the one-step process of Auger de-excitation and can be represented as

$$X^m + Ne_m^- \rightarrow X + e^- + (N-1)e_m^- \qquad (2.3.1\text{-}1)$$

where X^m represents the incident neutral particle in a metastable energy state, X the ground state, Ne_m^- the number of metal electrons, and e^- the secondary electron ejected from the metal surface.

Presented in Fig. 8 is a schematic representation of the potential energy and energy levels of a typical Auger de-exitation process. The metastable particle has approached to within a distance s from a clean metal surface having an average work function ϕ. The potential energy and the energy levels represent those resulting from the combined fields of the metastable particle and the metal surface. As a result of this interaction, there is some perturbation of the energy levels of the incident particle; these levels are designated as effective energy levels (such as E_x' and E_i')*. The energies of the metal electrons are distributed as a Fermi-Dirac gas from the bottom of the conduction band up to the Fermi level ε_F. Therefore, the minimum energy required to eject an electron is $(\varepsilon_o - \varepsilon_F)$, which is just the work function (ϕ) of the surface. Providing that E_x' is greater than ϕ, an electron can be ejected from the surface. However, not all excited electrons can escape from the surface due to elastic back scattering.

As a result of the interaction, there are two mechanisms whereby an electron can be ejected. In the first, represented in Fig. 8 by the solid transition arrows, a metal electron undergoes an Auger transition into the ground state of the incident particle with the excess energy $(E_x' - \beta)$ being provided to the ejected, excited atomic electron. In the second process,

---

* Hagstrum's notation has been adopted in this report; for a complete discussion of these perturbations and the theory of the Auger processes in general, see ref. 34.

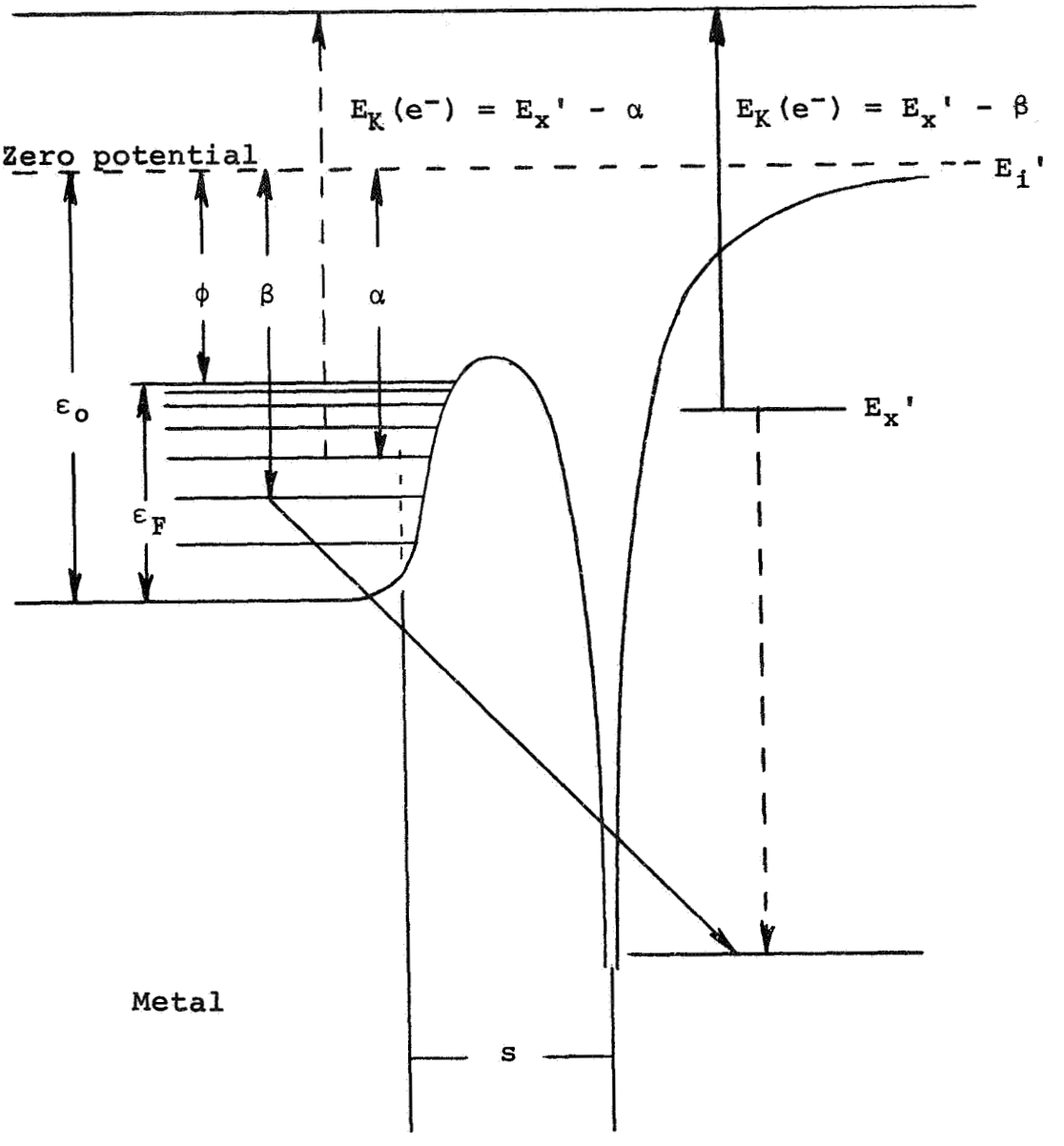

Fig. 8.- Schematic representation of Auger de-excitation.

represented by the dashed transition arrows, the excited atomic electron drops to the ground state and the excess energy ($E_x' - \alpha$) is provided to a metal electron ejected from one of the Fermi levels. It is, in general, not possible to distinguish the two processes since the energy of the ejected electrons has the same extremes. However, in some cases the direct (non-exchange) transition has a low probability of occurrence (such as the helium $2^3S_1 \rightarrow 1^1S_o$) since the transition requires a change of electron spin. In these cases, only the exchange transition need be considered. In Hagstrum's treatment, only exchange transitions were considered.

The extremes of the kinetic energy for the ejected electrons (in either process above) are

$$E_K(e^-)_{max} = E_x' - \phi \qquad (2.3.1\text{-}2)$$

and

$$E_K(e^-)_{min} = E_x' - \varepsilon_o \quad . \qquad (2.3.1\text{-}3)$$

It is clear from Eq. (2.3.1-2) that the secondary electron yield is zero for those systems in which $E_x' < \phi$. This occurs, for example, in the case of the 2^1S_o or 2^1D_2 atomic oxygen metastables incident on most metals, except perhaps the alkalis.

The probability of secondary electron emission occurring as a result of the Auger de-excitation process is greatest under "resonance" energy conditions; that is, when $\phi < (E_i' - E_x') < \varepsilon_o$. If $(E_i' - E_x') < \phi$, the more probable process is that of resonance ionization followed by Auger neutralization. However, as will be discussed later, the effective energy levels are shifted as the particle approaches the surface, the effective energy levels being related to the energy levels at infinite separation as follows:

$$E_x'(s) = E_x + E(m-M) - E(n-M) \qquad (2.3.1\text{-}4)$$

and

$$E_i'(s) - E_x'(s) = E_i - E_x + E(i-M) - E(m-M) \qquad (2.3.1\text{-}5)$$

where $E(m-M)$, $E(n-M)$ and $E(i-M)$ represent the interaction energies of the metastable, neutral and ion with the metal surface, respectively.

2.3.1.1.2 Resonance ionization - Auger neutralization. - The second process whereby an incident metastable particle can eject an electron is a two-step process. The metastable first undergoes resonance ionization which is then followed by Auger neutralization. The process is represented by

$$X^m + Ne_m^- \rightarrow X^+ + (N+1)e_m^- \quad \text{(resonance ionization)} \tag{2.3.1-6}$$

$$X^+ + Ne_m^- \rightarrow X + e^- + (N-2)e_m^- \quad \text{(Auger neutralization)} \tag{2.3.1-7}$$

where the notation is the same as in the previous section and X^+ represents the ion.

Presented in Fig. 9 is a schematic representation of the potential energy and energy levels for the two processes. In the resonance ionization processes (transition ①), the atom electron is ejected and captured into a vacant Fermi level. The probability of this process is greatest when $(E_i' - E_x') < \phi$. The ion thus formed is immediately neutralized by an Auger transition (transition ②) to the ground state of the atom. The excess energy is sufficient to eject a metal electron (transition ③).

The kinetic energy extremes of the ejected electrons are

$$E_K(e^-)_{max} = E_i' - 2\phi \tag{2.3.1-8}$$

and

$$E_K(e^-)_{min} = E_i' - 2\varepsilon_o \ . \tag{2.3.1-9}$$

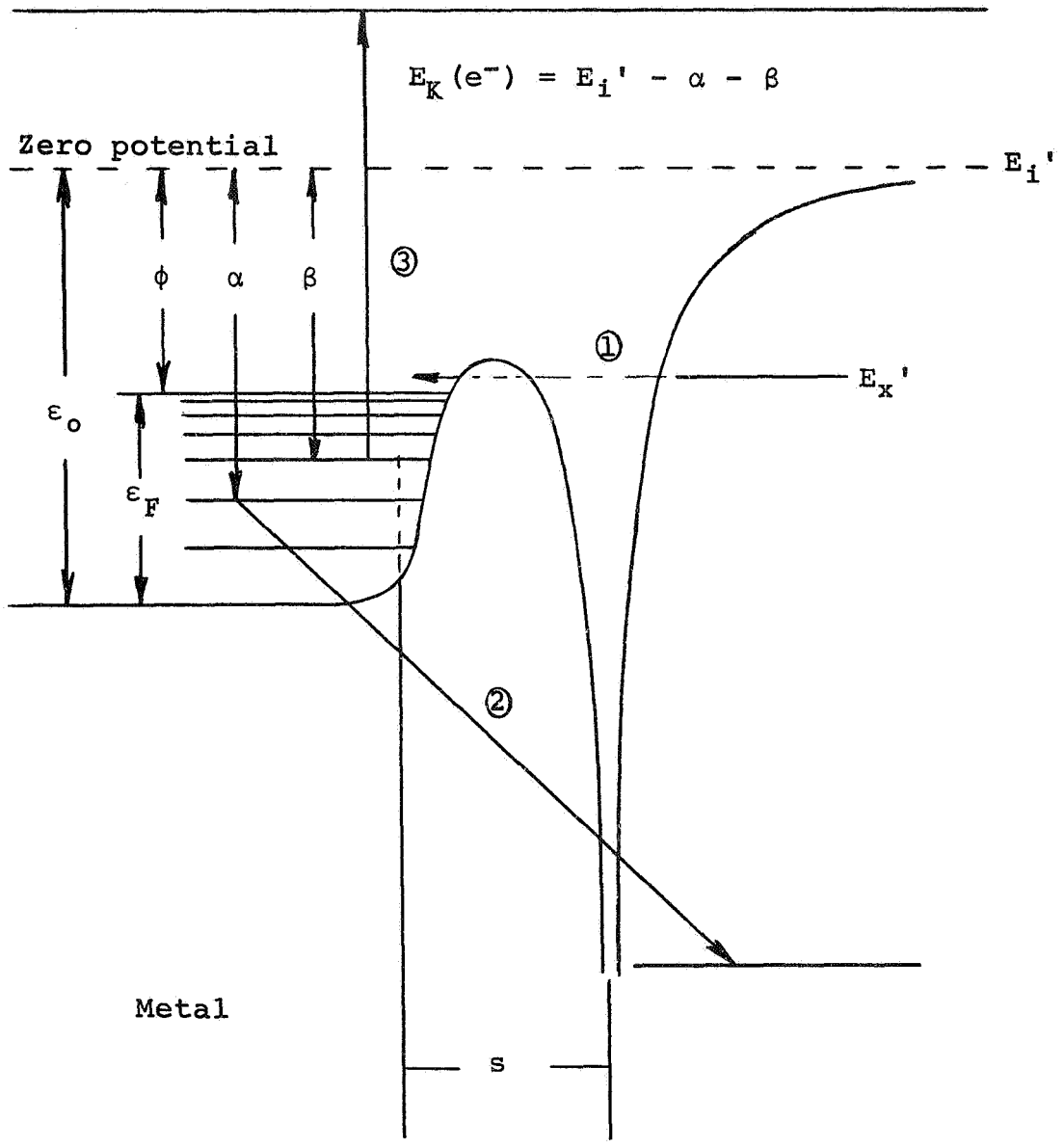

Fig. 9.- Schematic representation of resonance ionization Auger neutralization.

As in the case of Auger de-excitation, the resonance ionization process is highly improbable for systems such as the 2^1S_o or 2^1D_2 atomic oxygen metastables incident on most metals, since in this case $(E_i - E_x) >> \phi$.

The probability that the metastable de-excitation will proceed via the resonance process in favor of Auger de-excitation is not simply dependent upon the magnitude of $(E_i' - E_x')$ with respect to ϕ since the effective energies are involved, the effective energy being a function of the separation s. Because of this dependence, there will be a shift in the energy levels as the particle approaches the surface and it is possible, under certain circumstances, that one process being more probable for a given separation can become less probable as the particle approaches the surface. As shown in Fig. 10, there is a critical value of s, denoted as s_c, for which the energy levels of He^m and Ne^m are shifted upward so that resonance ionization is the more probable process, since now $(E_i' - E_x') < \phi$. For Ar^m, Kr^m and Xe^m, the energy levels are such that for any value of s resonance ionization is more probable. It has been concluded by Hagstrum, based on calculations of the transition probabilities for the various processes (these transition probabilities being functions of s and the particle velocity), that as the particle approaches the surface, the probability for resonance ionization is always greater than the probability for Auger de-excitation, the reason being that the probability for Auger de-excitation becomes appreciable only at values of s less than the critical separation for resonance ionization.

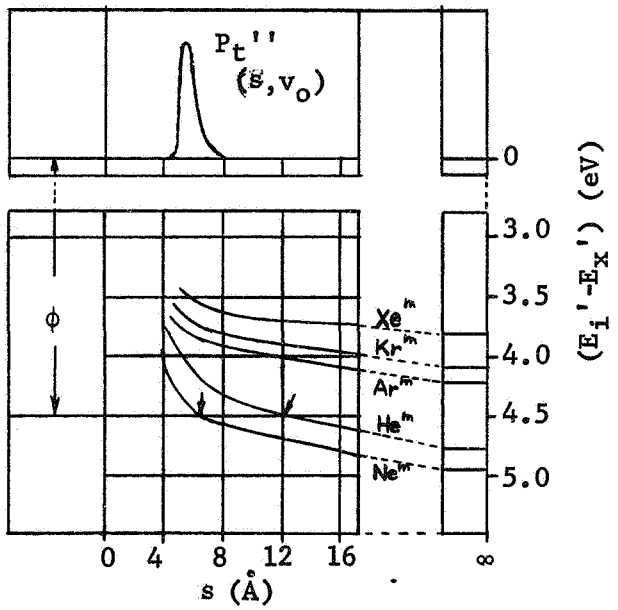

s_c is marked by arrows.
$P_t''(s,v_o)$ is the probability function for resonance ionization; v_o is the particle velocity.

Fig. 10.- Variation of metastable energy levels with distance from a tungsten surface (ref. 34).

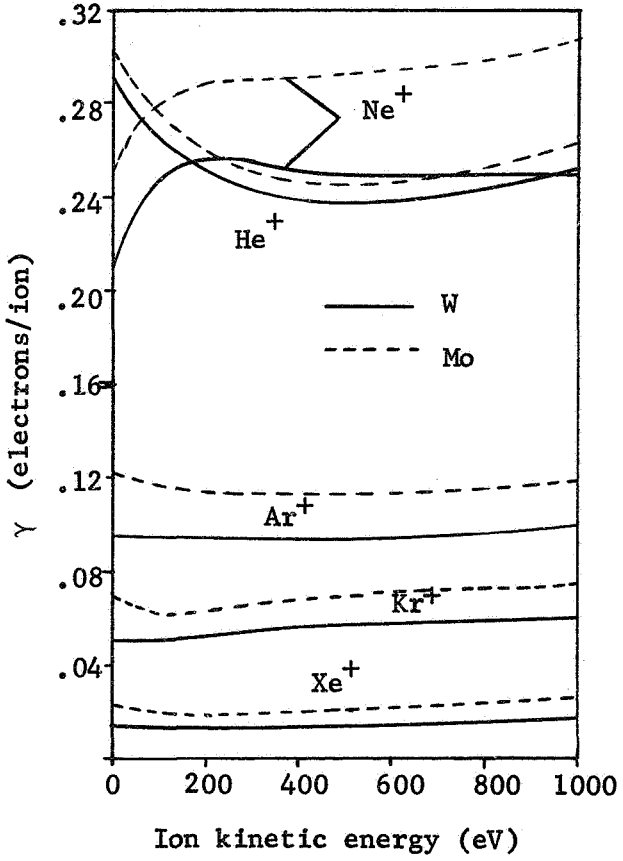

Fig. 11.- Secondary electron yield vs energy for noble gas ions incident on clean tungsten and molybdenum (ref. 35).

Since these conclusions are based primarily on the data for the noble gases, it is not obvious that the same conditions are appropriate for the atmospheric gases.

Based on a series of experiments, Hagstrum has concluded that since resonance ionization is the most probable first process, it is not possible to distinguish between processes involving neutral metastable particles and ions. Therefore, most of his data are for singly and multiply charged noble gas ions incident on tungsten and molybdenum. It is clear from his discussions that a meaningful interpretation of the processes involved is possible only if the energy distribution of the ejected electrons is known. It is probable, then, that some provision for this measurement should be made in the experiment. Presented in Fig. 11 are data for the secondary electron yield for the singly charged noble gas ions incident on clean tungsten and molybdenum for ion energies in the range 10 eV to 1 keV.

Based on the discussions of the potential emission processes and the data of Fig. 11, the following observations can be made:

1. The secondary electron yield is fairly constant over a wide range of incident particle energies as it should be for potential emission.

2. As predicted by the theory, the yield decreases as the work function increases, which is reasonable since the electron escape probability is greater for the lower work function.

3. As $(E_i - 2\phi)$ decreases, the yield decreases.

However, there are some discrepancies which are not directly explainable. For example, as $(E_i - 2\phi)$ decreases, the ratio of the yield for Mo and W increases. It is likely, therefore, that additional factors contribute to the yield of clean surfaces. As shown by the data of Parker (ref. 36) for A^+ on clean platinum (ϕ_{Pt} = 5.3 eV) and clean Ta(ϕ_{Ta} = 4.9eV), the yield for Pt is higher than Ta despite the fact that $\phi_{Pt} > \phi_{Ta}$. Another, more convincing experiment was conducted by MacLennan and Delchar (ref. 37), which shows that other factors than the work function, per se, are involved in the observed yield. In their experiment, metastable helium and argon beams were directed onto the (111) and (110) planes of a single crystal tungsten sample, the stated values for the work function of the two crystal planes being $\phi(111) = 4.3$ eV and $\phi(110) = 5.6$ eV. One would, therefore, expect a significant difference in the yield for the different crystal planes. However, the results showed the electron yield for the (111) plane to be .300 for helium and .091 for argon; for the (110) plane, about 1.5% lower for helium and about 4% lower for argon. The explanation for this result, according to the authors, is that the work function difference between the crystal planes arises from a surface topography effect and as the ion approaches the surface (assuming resonance ionization of the metastables), the interaction potential causes electrons to tunnel out and neutralize the positive "hills", thereby reducing the surface topography effect and reducing the effective work function difference to almost zero.

Up to this point, only the secondary electron yield of clean metal surfaces as a result of incident metastable particles has been considered. There is, however, emanating from the source a flux of neutral particles in the ground state and photons together with the metastables. Therefore, the role of each of these intermingled fluxes must be considered, since they are not separable nor is it possible to completely discriminate against them in the time-of-flight measurements.

2.3.1.2 Photoemission. - Since a complete analysis of the effect of photoemission from the detector and the role it plays in obscuring the secondary yield of the metastable flux is not possible without complete knowledge of the excitation cross-sections of each of the radiating states of all the major atmospheric constituents as a function of the electron beam energy, and even if they were known, the calculation would be an enormous task, it is considered more meaningful to cite the results of experiments which have been performed under operating conditions similar to those which will be encountered in the flight apparatus.

In prior investigations, in general, no mention is made of the surface conditions of the detector. Although the bulk detector material is specified, surface films such as diffusion pump oil or layers of adsorbed gas will influence, to a great extent, the yield resulting from photon absorption. Another point of concern is that even though some of the atmospheric constituents such as atomic and molecular oxygen will not be effective in the metastable detection scheme, they do possess radiating states which will contribute to the total photon flux. Because of the wide range of contributing band spectra and discrete atomic spectra, there is an almost continuous distribution of wavelengths contributing a rather broad band of energies incident at the detector. To limit

the extent of the radiating spectrum as much as possible, a low value for the exciting electron energy is desirable.

It is, in general, considered that the emitted radiation emanating from the region of the electron impact source is isotropic; thus, by reducing the solid angle subtended at the detector, the undesirable secondary electron current due to the photon flux can be diminished. This isotropy may be assumed and the decrease with solid angle will occur as long as the lifetimes of the radiating states are short enough that the drift of the excited particles is negligible. If this is not the case, then the region from which radiation is emitted expands toward the detector. Consider a thermal N_2 beam experiment in which there is a range of lifetimes for the radiating states involved. Those states which are short-lived (<10 μsec) contribute nearly isotropic radiation emanating from the region of the electron beam. Those states which are long-lived (>500 μsec) reach the detector and are counted as incident metastables. For the states with intermediate lifetimes, the excited particles drift towards the detector and can emit a photon from any position along the flight path. The region from which radiation emanates, thus, has considerable extent and the radiation incident upon the detector may not be considered as isotropic. In addition, as the excited particles drift towards the detector, the solid angle subtended at the detector increases so that when they radiate, the probability that the photon will intercept the detector increases.

If we extend these same ideas to the case of the flight experiment, a re-definition of the effective lifetimes is necessary because of the velocity bias. The term metastable becomes somewhat ambiguous because the average flight time is now reduced to the order of microseconds (depending on the vehicle speed and the flight length). It is, therefore, not possible to dis-

criminate so easily between photon flux and neutral "metastable" flux. The effect of these intermediate radiating states (depending on the intensity) is to smear out the distribution of metastable arrival times or to mask the time of flight distribution, especially at the onset, since the overlap will occur at the shorter flight times (higher particle velocities).

Briglia (ref. 38), in investigations of the lifetime of excited molecular nitrogen states, used an apparatus somewhat analogous to the one considered for flight application. A molecular beam, crossed by a pulsed electron beam, passed through a quadrupole and was incident on an electron multiplier with Cu-Be dynodes. The flight length from the electron beam to the multiplier was 28.5 cm. Phase sensitive detection allowed for discrimination between the photon and metastable flux. Shown in Fig. 12 are his results for the excitation function of N_2 together with the signal resulting from the photon flux. No estimates were given for the beam density, only that the system pressure was 5×10^{-5} Torr. The multiplier aperture was 6 mm x 18 mm which, together with the flight length of 28.5 cm, yields a solid angle of approximately 1.3×10^{-3} sr. (assuming that there is an entrance aperture to the quadrupole and, therefore, the source can be considered a point source). At an electron excitation energy of 12eV, the photon signal is greater than the metastable signal.

In a similar experiment, Lichten (ref. 17) used a molecular N_2 beam formed by a series of collimating slits, crossed by a continuously operating electron beam. The resulting beam was then incident upon a magnesium collector. The effects of the photon flux were directly measured and it was found that the detector current due to photoemission was 10% or less for all exciting energies between 8.5 and 16 eV. No mention of the solid angle is made and there is no way to estimate it from the data presented.

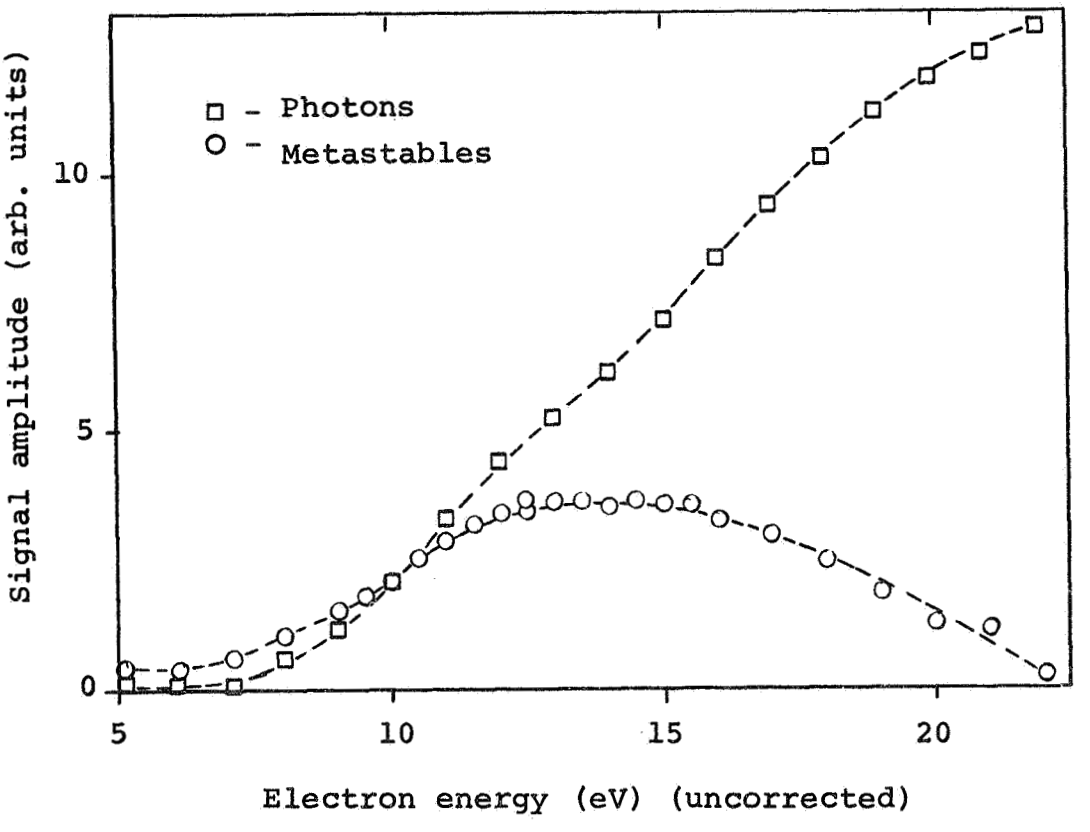

Fig. 12.- Comparison of photon and metastable nitrogen signals (ref. 38).

From these results, it is obvious that the effect of radiating states and the role they play in the final analysis of the detector output is not negligible. It would be desirable to use as long a flight path as possible so that at least the rapidly decaying states are distinguishable. This of course, is accomplished with a corresponding loss in sensitivity.

2.3.1.3 Kinetic emission. Of the major constituents in the molecular beam after it has passed through the electron beam, consideration has been given to the detector response of two of the major reaction products, namely, metastables and photons. There is, however, a large percentage of neutral ground state particles which remain in the beam. The effect of these neutral particles on the detector signal must also be evaluated.

In general, the total secondary electron yield (γ) is composed of two parts: one due to the potential energy of the particle (γ_{Pot}), which has already been considered, and another due to the kinetic energy (γ_{kin}). It was concluded that the condition for emission of electrons due to potential emission alone, as a result of incident ions (assuming that resonance ionization is the most probable process), is $E_i > 2\phi$. It was also seen that γ_{Pot} was independent of the kinetic energy of the incident ion, at least up to 1 keV. The equivalent condition for the ion impact production of electrons by kinetic emission alone is that $E_i < \phi$ and that the incident ion possess kinetic energy greater than a certain threshold value (E_{th}). In the case of incident neutrals, the only necessary condition is that the particle possess kinetic energy greater than E_{th}. In those cases where $E_i < 2\phi$ and the incident ion also has sufficient kinetic energy, the total yield becomes $\gamma = \gamma_{Pot} + \gamma_{kin}$. Presented in Fig. 13 are the data of Arifov et. al. (ref. 39) for the secondary electron yield of Ar^+ and Ar° incident on a clean Mo target. The inci-

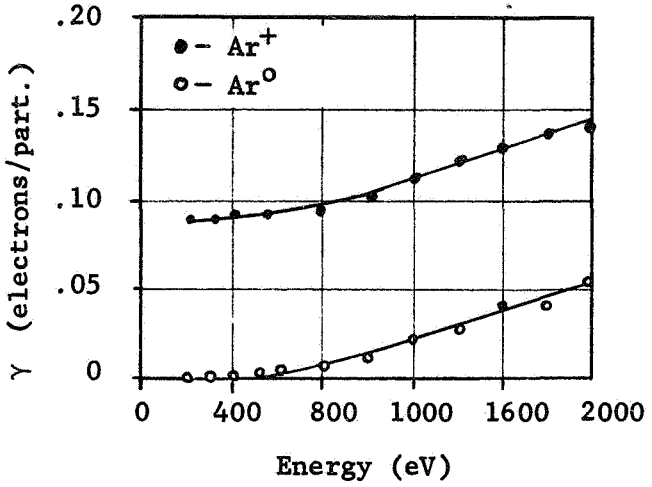

Fig. 13.- Secondary electron yield for Ar^+ and Ar^o incident on clean molybdenum (ref. 39).

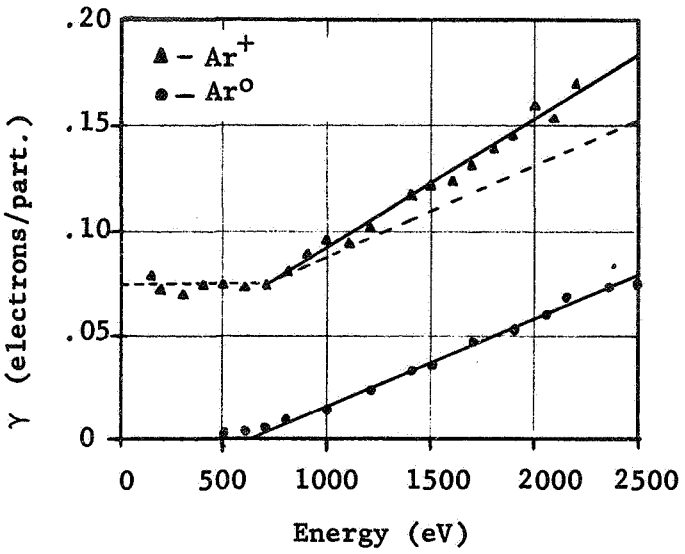

Fig. 14.- Energy dependence of γ_{pot} and γ_{kin} for Ar^+ and Ar^o incident on clean molybdenum (ref. 40).

dent particle energy was varied from 200 eV to 2 KeV. It can be seen that the ascending portions of both curves have the same slope representing kenetic emission, the Ar^+ curve levels off to a constant value representing potential emission, and the Ar° curve goes to zero at approximately 400 eV representing the threshold energy for kinetic emission due to neutrals.

In a similar experiment, Medved et. al. (ref. 40) shows somewhat the same results for γ_{Pot} and E_{th} but the energy dependency (E > 1 keV) of the yield for incident ions is different than for incident neutrals; see Fig. 14. Medved suggests that this divergence shows that there is a dependence of γ_{Pot} on energy (avove E_{th}, at least). This contradicts the results of Hagstrum, as presented in Fig. 11.

These data indicate the general characteristics of secondary electron yield at low energies. However, the region of interest to this discussion is the energy region near the threshold and below. Unfortunately, this region has not been experimentally investigated to the degree that the higher energy regions have, the majority of the work being done from 1 keV up to hundreds of keV and extending into the MeV region. This, together with the fact that no unified theory has been developed which successfully accounts for the experimental data over the entire energy range, which is likely due to the variety of ejection mechanisms which can occur when considering the energies involved, means that the necessary conclusions must be inferred from that data which is available, together with extrapolations and trends of existing data. For a more complete discussion of the experimental results and theory at higher energies, reference can be made, for

example, to Kaminsky (ref. 32).

One of the questions to be discussed is the dependence of E_{th} on the particle mass and the target material. It is difficult to draw anything but a qualitative conclusion since the majority of the available data is for ion impact at higher energies (1 keV < E < 1 MeV). That data which is available at the lower energies for neutral particles represents a mixture of surfaces, surface conditions, and angle of incidence. However, based on the data for γ_{kin} for Ne^+, Ar^+, and Kr^+ on Mo (Arifov and Rakhimov ref. 41), in the energy range 2 - 10 keV, it can be seen that the kinetic yield is inversely proportional to the ion mass. It can be concluded further, based on the data of Magnuson and Carlston (ref. 42) for Ar^+ incident on Ni, Al, Cu, Mo, Ta, and Zr, that γ_{kin} is rather insensitive to the target material. However, some degree of skepticism should be exercised with regard to this latter conclusion, for Magnuson and Carlston (ref. 43) have also shown that the γ vs. energy curves for the three low-index planes of a single crystal copper target diverge from a common value at 1 keV, until at 10 keV the ratio of $\gamma(111)$ to $\gamma(110)$ is approximately 2.5.

With these generalized conclusions, it is now possible to examine the available data and attempt a plausible conclusion concerning the degree to which the neutral kinetic yield will influence the measurement of the metastable potential yield. Shown in Fig. 15 are data for the kinetic yield of H°, He°, and Ar°. Although they represent a variety of conditions, each of which could influence the magnitude and shape of the curves, the conditions under which the experiments were conducted can be examined and, thereby, some valid conclusions can be drawn.

The H° results reported by Fleischmann and Young (ref. 44) are somewhat questionable in regard to their correlation with

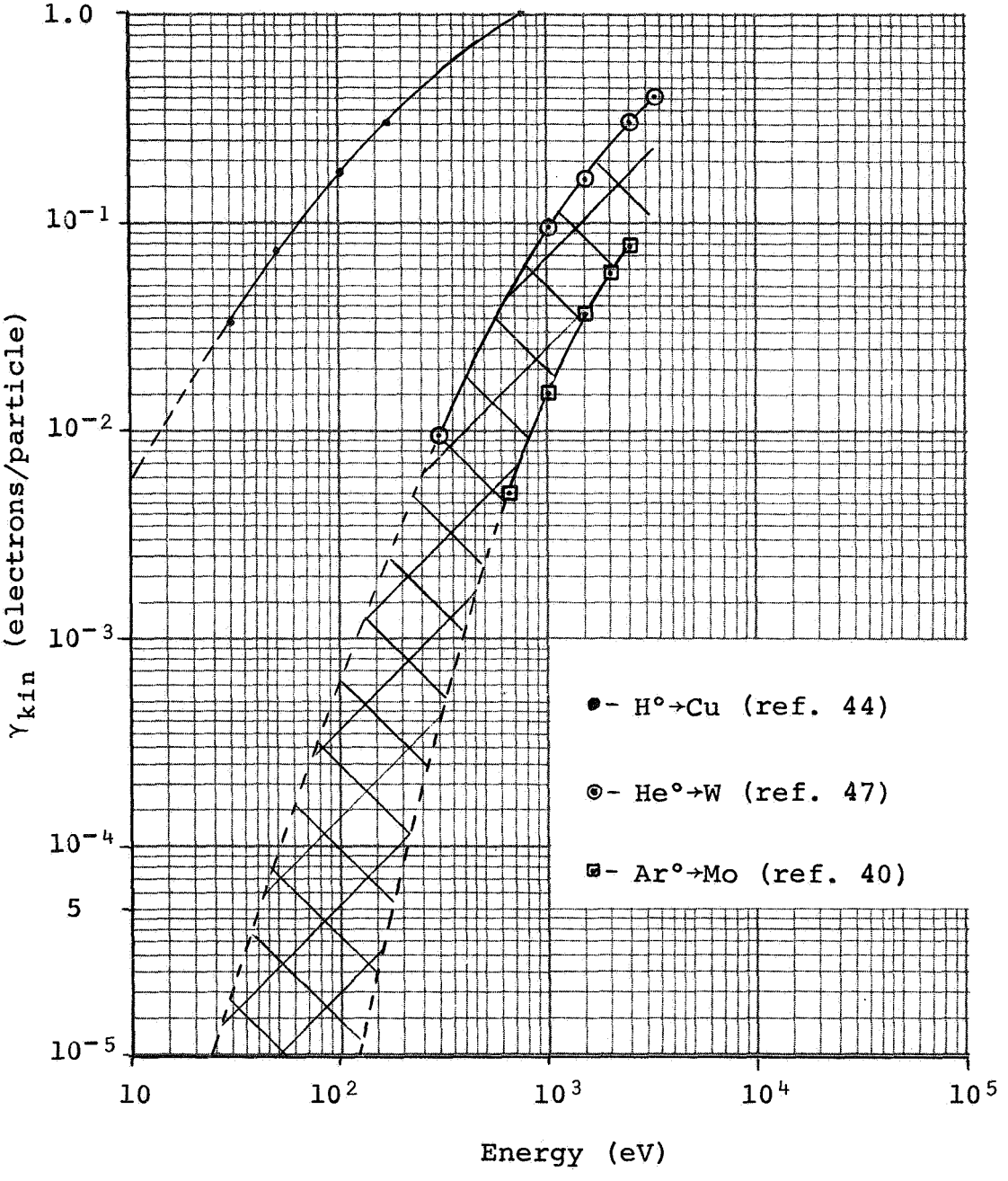

Fig. 15.- Kinetic yield for H°, He°, and Ar°.

the He° and Ar° data. The target was "cleaned with hydrochloric acid and alcohol" and, therefore, was probably covered with a residue and adsorbed gases, which will be shown, in the next section, has a drastic effect on the yield. The He° and Ar° data, on the other hand, are results taken after the targets were flashed to 2200°K and should be somewhat consistent. Since hydrogen is a minor constituent in the atmosphere for the ranges of interest, the absolute magnitude of this curve is not of great concern; it has been included for comparison and to indicate that the inverse relationship between yield and mass is still preserved at threshold. Since the angle of incidence is not given in the case of Ar° , it has been assumed that the shift in the yield curve caused by the possible differences in α is negligible (this point will be discussed later). The effect of the different target material is not known; however, it should be pointed out that differences in the yield curves presented by various observers for the same incident particle-surface combination differ markedly, on the one hand, while the data of a single observer for the same incident particle on various surfaces produce almost identical results, on the other. Since these results are contradictory, it will be concluded that surface contamination is the dominant consideration and, therefore, the He° and Ar° data are consistent, since the surface preparation was similar in the two experiments.

It will be remembered that the range of molecular weights to be encountered in the atmosphere lies within those of He and Ar and, therefore, the yield curves can be assumed to lie within the band as indicated on Fig. 15. This assumption requires that the functional dependence of $\gamma(E)$ on the molecular weight is not just fortuitous, but the theory of Von Roos (ref. 45) which

explains quite well the interaction of low energy ions at metal surfaces, both with respect to reflection and kinetic emission, expresses the yield for constant energy as

$$\gamma \propto \frac{(1 + \mu)^4}{\mu} \qquad (2.3.1\text{-}10)$$

and for constant velocity as

$$\gamma \propto \frac{(1 + \mu)^4}{\mu^3} \qquad (2.3.1\text{-}11)$$

where μ is the ratio of the mass of the incident ion to the mass of the target atom. Since μ is generally much less than 1, Eq. (2.3.1-10) implies an inverse relationship of γ with molecular weight. It has, therefore, been assumed that the yields will lie within the band of Fig. 15.

Since the major fraction of the kinetic energy of the particles arises from the vehicle velocity, the heavier particles will be the most energetic. Considering 10 km/sec to be the maximum vehicle speed and Ar to be the highest molecular weight component, approximately 20 eV is the maximum translational energy to be encountered.

It is, therefore, possible to expect the yields, based on extrapolated values of the band, to be of the order of 10^{-6} or 10^{-7}.

However, when it is recalled that the ratio of metastables-to-neutrals can be of the order of 10^{-4} - 10^{-5} (depending on the source conditions), it is not obvious that the secondary electron yield due to neutrals is negligible when compared with the yield for metastables, which was shown above to be <0.1.

2.3.2 Effects of Adsorbate

In the previous discussions of secondary electron emission, an attempt has been made to include only those data representative of clean surfaces (in the atomic sense), since only under these conditions can one arrive at a consistent and valid conclusion. This has meant the omission of much of the available data for specific incident particle-surface combinations which are necessary for a complete analysis. However, it was felt that the inclusion of data for surfaces which were either not specified or for those with unknown surface preparation or coverage would lead to greater errors than have likely arisen otherwise.

It is appropriate to reexamine the various secondary electron yields to see exactly what effect surface contamination or, more definitively, controlled and known adsorbates at specified relative surface coverage would have on the results. This evaluation is necessary since, due to the high molecular collision frequency density, the detector will be covered with at least a partial monolayer of gas even at the lower atmospheric densities, in spite of attempts to preserve its cleanliness.

As an example of the effect of adsorbate on the potential yield, the data of Parker (ref. 36) for Ar^+ on platinum both in the "clean" (flashed to 1400°C) condition and gas covered (5 minute exposure at a few Torr) condition are presented in Fig. 16. It can be seen that oxygen reduces the yield by more than an order of magnitude.

Although the results are not directly comparable due to different gas-surface combinations, Delchar et. al. (ref. 46) observed that the yield decreased by 42% in the case of metastable helium atoms incident on N_2 covered polycrystalline tungsten ribbon. Similarly, the decrease in the secondary yield for CO coverage was 63%. The general results and conclusions of Delchar et. al. enforce the hypothesis that the yield, based on evaluation of the electron energy distribution, is not simply related to the work function but is rather the result of a complex interation between the incident particle and the adsorbed gas-metal surface. Delchar et. al. suggest that the most important variable is the surface density of the adsorbed species, with particular emphasis placed on the binding mechanism of the adsorbed gas atom to the lattice. They postulate that the mechanism, which describes their results, involves the formation of an energy level above the ground state of the adsorbed gas atom. The ejected electrons can then come from either this energy state, the Fermi sea, or both. The resonance ionization-neutralization process is shown schematically in Fig. 17. The energy distribution of ejected electrons is now strongly influenced by both the adsorbate species and the coverage, the coverage influencing primarily the number of electrons ejected from the metal. This process effectively describes the observed decrease in the number of ejected high energy electrons with adsorbed gas on the sample as well as some of the anomalies observed with their single crystal experiments.

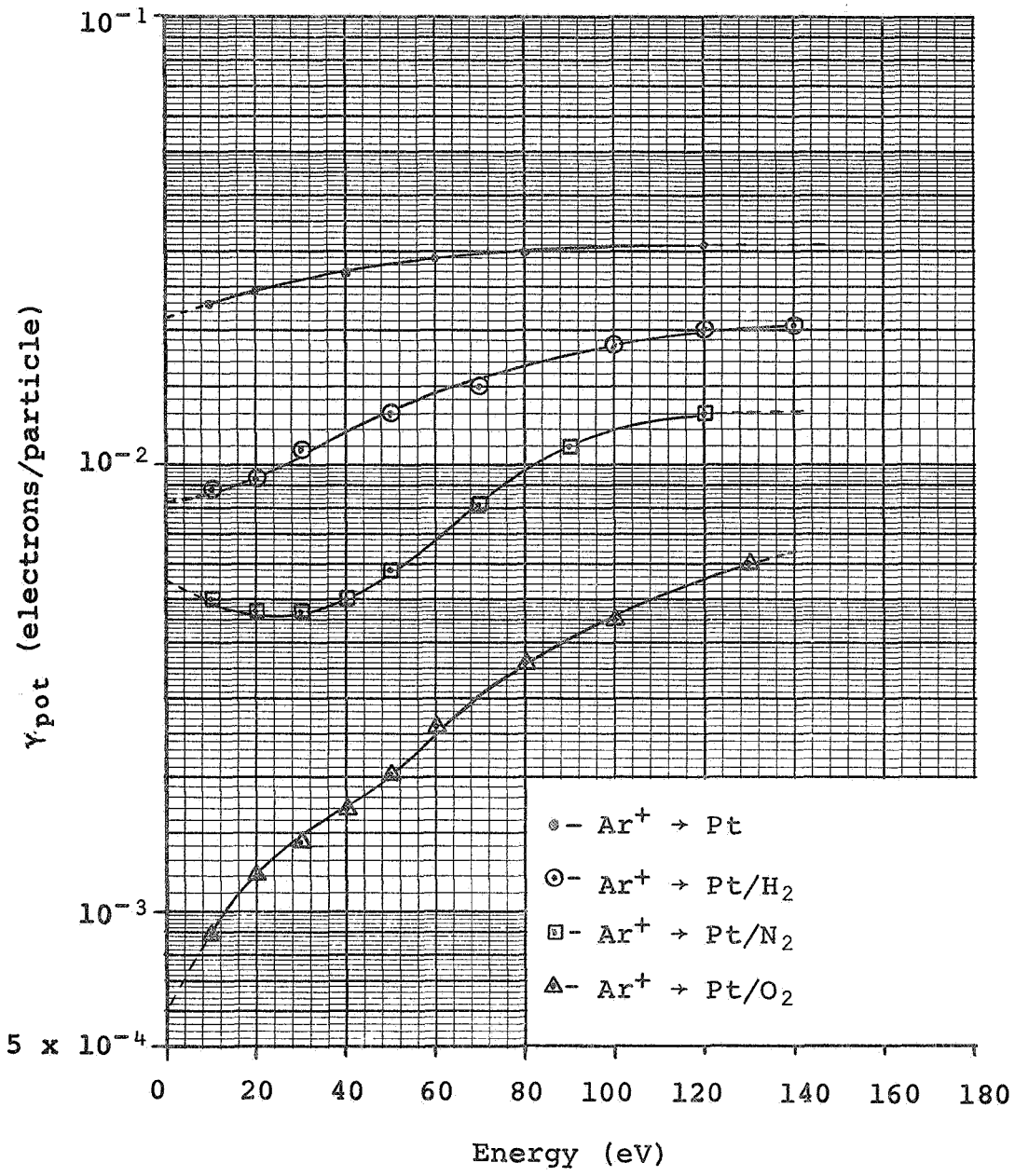

Fig. 16.- Potential yield for Ar^+ incident on degassed platinum and platinum with various adsorbates (ref. 36).

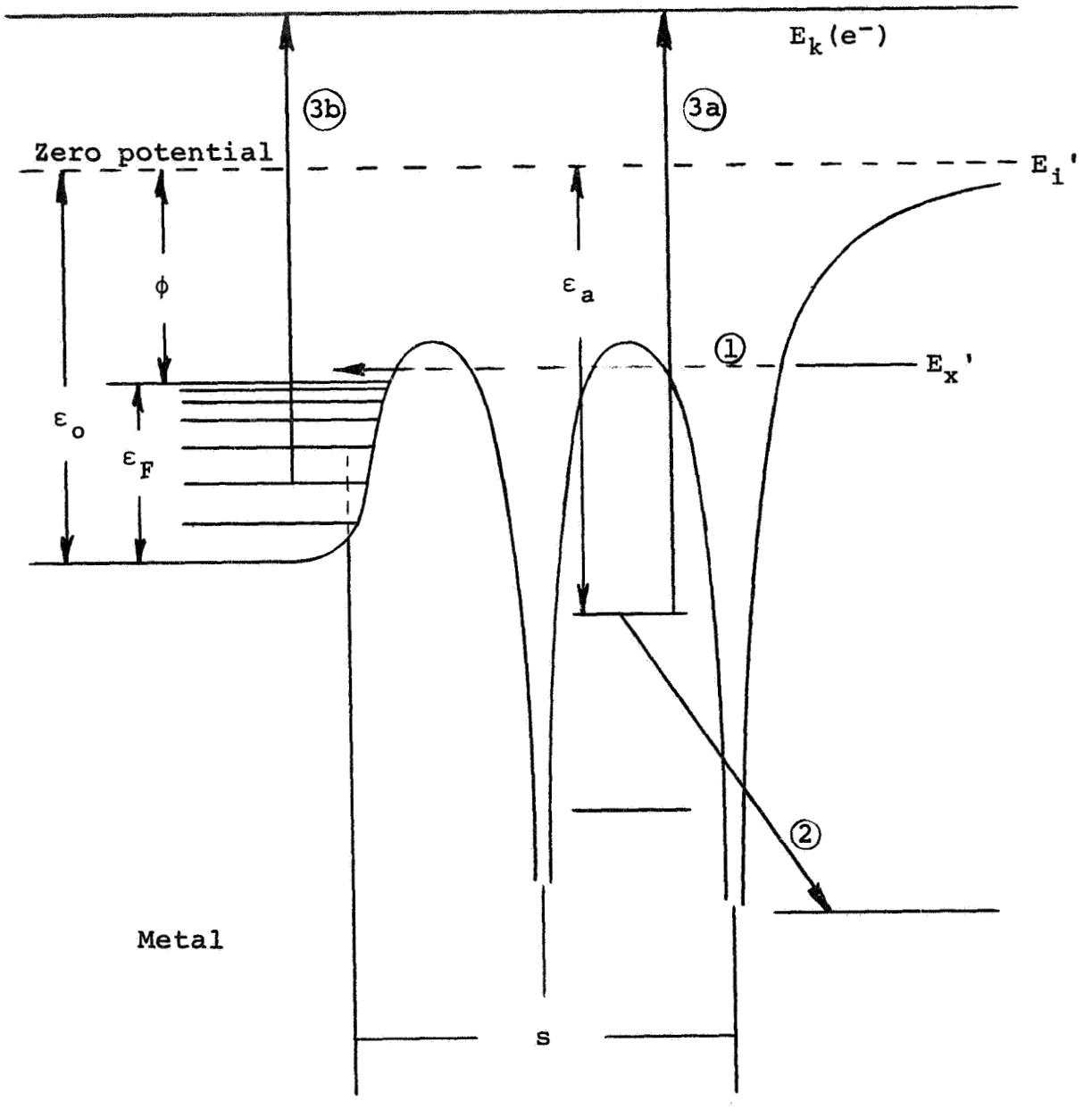

Fig. 17.- Schematic representation of the resonance ionization-neutralization process for a gas covered surface (ref. 46).

These data show that there is a general degradation of the potential yield which is a rather strong function of the adsorbed species. Aggravating this problem is a dependence of the kinetic yield which tends to increase with gas coverage. For example, shown in Fig. 18 are the data of Berry (ref. 47) for the kinetic ejection of electrons from both degassed and undegassed tungsten targets as a result of incident helium ions and neutral atoms.

The problem now is obvious. Considering the ratio of $\gamma_{Pot}/\gamma_{kin}$ to represent the signal-to-noise ratio, then as gas is adsorbed on the detector, the S/N ratio decreases both because γ_{Pot} is decreasing and simultaneously γ_{kin} is increasing. It is, therefore, advantageous to keep the detector as clean as possible. This becomes a rather difficult problem, since the three major constituents of the atmosphere for the intended measurements are O_2, O, and N_2, which are chemically active gases in contrast to the noble gases which have been used in most of the literature data.

There is still the problem of estimating the yield for incident N_2^m. If resonance ionization-Auger neutralization is assumed to be the mechanism by which the excitation energy of the nitrogen metastable is transferred to the detector surface, the ion ejection yield data of Parker (ref. 36) can be used to get an order of magnitude estimate for the secondary electron yield. Presented in Fig. 19 are data for γ_{Pot} for nitrogen ions incident on nitrogen covered platinum. The ion beam consisted of N^+ and N_2^+ in unknown proportions. The increased yield at the lower ion energies was concluded to be due to recombination of N^+ at the surface, which, of course, is not possible for incident N_2^m. One can extrapolate the expotential decay of the

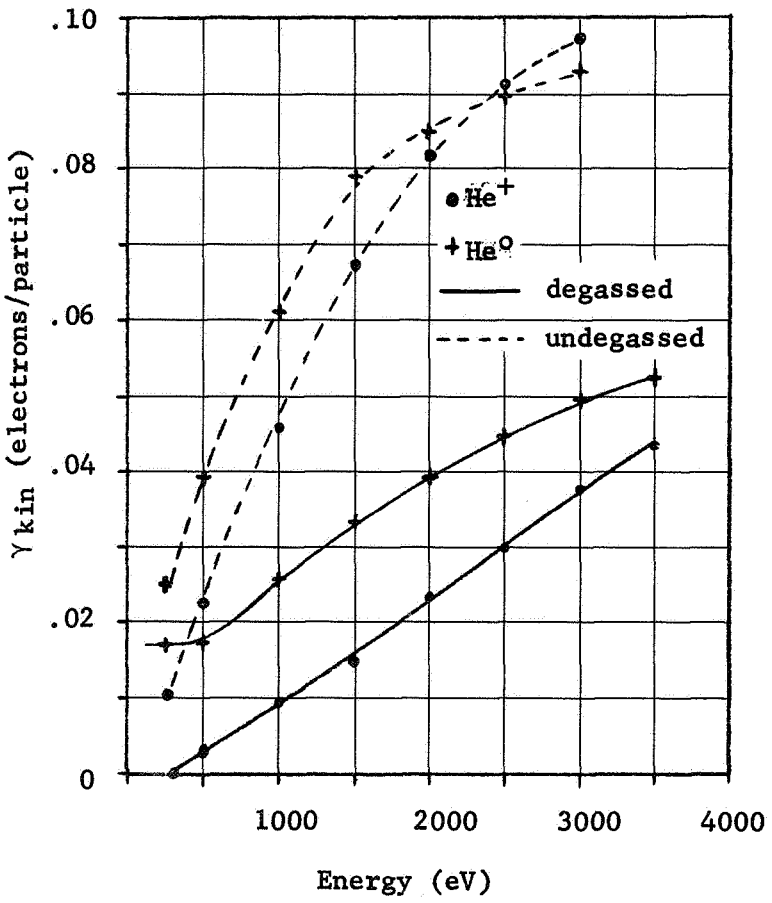

Fig. 18.- Kinetic yield for He^+ and He^o incident on degassed and undegassed tungsten (ref. 47).

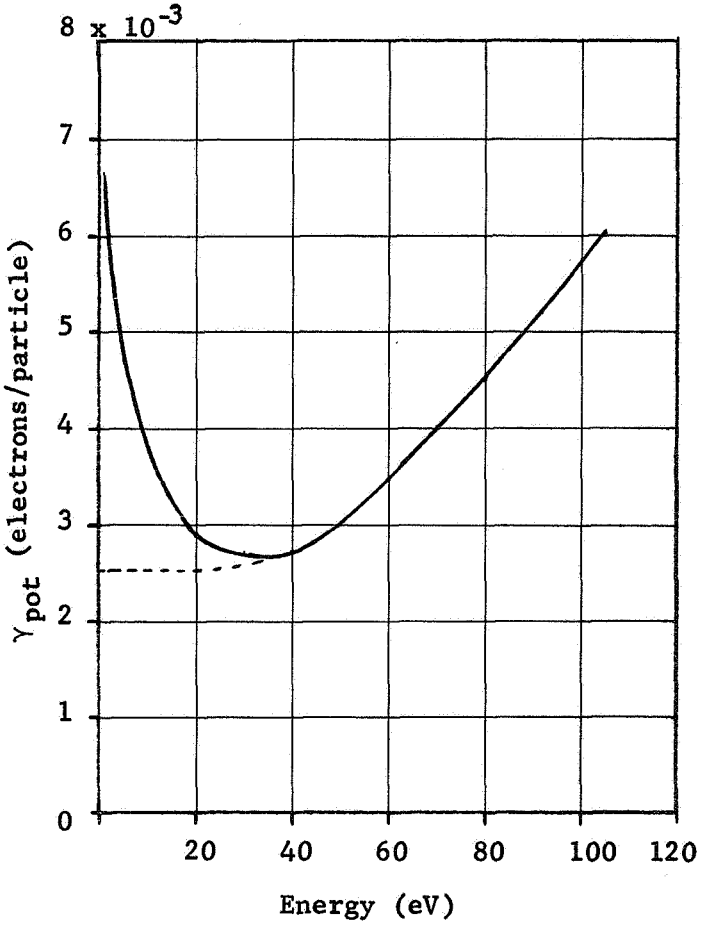

Fig. 19.- Potential yield for nitrogen ions on nitrogen covered platinum (ref. 36).

curve (neglecting recombination) and arrive at 2.5×10^{-3} for the yield. Based on the similarities of the data for the yield of Ar^+ on nitrogen covered platinum ($Ar^+ \rightarrow Pt/N_2$) and $Ar^+ \rightarrow Pt/O_2$ with the data for $N_2^+ \rightarrow Pt/N_2$ and $O_2 \rightarrow Pt/O_2$ (a result which is not too surprising since the energy available after neutralization of the ion is comparable in all three cases $(E_i)_{N_2} = 15.58$ eV, $(E_i)_{Ar} = 15.76$ eV, and $(E_i)_{O_2} = 12.2$ eV), one can estimate that the yield for $N_2^+ \rightarrow Pt$ would be approximately 0.009. Furthermore, using the yield data for $Ar^+ \rightarrow Pt$ (.02) and $Ar^+ \rightarrow W$ (.095) and assuming again that the similarity analogy is valid, the yield for $N_2^+ \rightarrow W$ would be 0.043. This value is in good agreement with the value of .06 electrons/ metastable estimated by Zorn and Pearl (ref. 48).

If there is any validity to this type of argument, then the yield values could be expected to range from 0.043 for $N_2^m \rightarrow W$ to 1.2×10^{-3} for $N_2^m \rightarrow W/O_2$.

2.3.3 Angle of Incidence

Since some angle other than normal incidence will probably be chosen to reduce the amount of back scattering into the incident beam, it is appropriate to say something about the angle of incidence of the molecular beam on the detector and its effect on the yield.

For kinetic emission, it has been found that the experimental data for the variation of secondary electron yield as a function of angle of incidence can be expressed as:

$$\gamma(\alpha) = C\,\gamma_o \sec\alpha \qquad (2.3.3\text{-}1)$$

where α is the angle between the incident beam direction and the surface normal, γ_o is the yield at normal incidence, and C is a proportionality constant which is dependent on the incident particle-surface combination. However, since most of the data which substantiates the above relationship was obtained at higher energies, it is not known whether this relationship holds at the lower energies. For example, at the higher energies where there is substantial penetration into the lattice, it would be expected that the yield be a function of α. However, based on the independence of γ_{Pot} on energy, it can be assumed that the interaction occurs primarily at the surface and, therefore, one would not expect a substantial dependence on α for either γ_{Pot} or γ_{kin} at the low energies of interest to this analysis.

3. SPECIFIC TEMPERATURE MEASUREMENT TECHNIQUES

In the previous sections, the parameters which influence the sensitivity of molecular beam measurements have been considered with respect to excitation and detection processes, as well as those processes which must be discriminated against since they contribute to that signal which is attributable to background or noise. In this section, specific methods for deriving temperature information from the molecular beam will be described and analyzed.

Since measurements are to be made under conditions of free molecular flow, it is appropriate that the physical properties of the gas (including that of temperature) be deduced from the statistical properties of the flow. The theoretical formulation of the problem is based on the assumption that the properties of the molecular beam can be descrived in terms of a drifting Maxwellian gas, an infinitesimal sample of which contains a group of molecules with a velocity distribution characteristic of the volume of space from which the beam was derived. Several methods of temperature measurement will be presented to determine their respective sensitivities and resolutions.

In the following sections, three variations of establishing the temperature in terms of parameters related to the velocity distribution function will be discussed: 1) the metastable time-of-flight (MTOF) detection system, 2) the flux angular distribution method, and 3) the retarding potential energy distribution method. The MTOF system is analogous to a mechanically chopped beam detection system except that the modulation is accomplished electronically and the beam modulation and molecular

excitation occur simultaneously. The flux angular distribution method does not explicitly yield the distribution function. However, it is indirectly implied since the differential flux per unit solid angle is directly related to the distribution function. Likewise, the retarding potential energy distribution method does not directly establish the distribution function but the data displayed as ion current vs. retarding potential may be directly interpreted in terms of the temperature.

3.1 TIME-OF-FLIGHT (TOF) VELOCITY DISTRIBUTION ANALYSIS

3.1.1 General Discussion of TOF Detection Systems

The early successes of the kinetic theory and its general acceptance were due in part to the various experimental investigations of the distribution of velocities from oven beams and the general agreement of the results with that described by the Maxwell-Boltzmann distribution function. That distribution, defined as

$$f(v) = \left(\frac{m}{2\pi kT} \right)^{3/2} e^{-\frac{mv^2}{2kT}} \qquad (3.1.1\text{-}1)$$

may be seen to be represented in terms of a characteristic temperature which may be thought of as the temperature of the walls of an isothermal volume in which the gas in question is contained. The majority of these early experiments used some mechanical means for modulating the beam and, in general, utilized either molecular condensation or surface ionization detectors. Later modifications of these experiments to measure $f(v)$ and, thus, T employed multi-disc velocity selectors or TOF correlation measurements, which yield, in a very elegant manner, the inverse

of the velocity distribution f(v), allowing immediately the extraction of T. In the TOF method, a representative sample of the gas to be analyzed is introduced into the system through a gating chopper and allowed to drift and, thus, separate in time, depending on the various speeds represented by the molecular ensemble. A review of many of these experimental techniques and a thorough analysis of the mechanical chopper-electron impact ionizer system, applicable to thermal beams, has been presented, among others, by Scott (ref. 49). Similar analyses of both chopper-ionizer and chopper-velocity filter detection systems, applicable to supersonic beams, have been presented by Knuth and Kuluva (ref. 50) and by Alcalay and Knuth (ref. 51).

The problem in the case of TOF measurements of a nonstationary gas is to produce a time dependent signal, representing the velocity distribution, which is not influenced by the relative motion of the sampler with respect to the gas nor by usual instrumental effects. Further, the beam chopping or modulation process must have negligible effect on the measured molecular drift times. As will be seen later, this condition requires that the chopper open time be less than 1 μsec for the system parameters normally met in high speed vehicle probes of planetary atmospheres. Since this corresponds to chopper rotational speeds about 10 times greater than normally used and is approaching the speed where the material strength and the chopper stability come into question, it is obvious that mechanically chopped systems are not feasible.

3.1.2 Metastable Time-Of-Flight Detection System

In the MTOF detection scheme, simultaneous gating of the beam and excitation of beam molecules is accomplished using a pulsed electron beam situated orthogonal to the molecular beam axis. A schematic representation of a MTOF detection system is presented in Fig. 20. The flight of the excited metastable neutrals is not affected by stray or unknown electric or magnetic fields, as ions would be in a similar TOF scheme. Detection and discrimination are accomplished by time domain signal averaging with a multi-channel analyzer, the time reference being correlated with the gating pulses controlling the electron beam pulse duration. The TOF signal, representing the molecular velocity distribution of the undisturbed gas, is stored in differential form. The purpose of this section is to discuss the conditions influencing the TOF signal wave form and to estimate the MTOF system sensitivity.

The following assumptions have been made in calculating the system sensitivity:

1) The neutral molecular flux density passing through the interaction volume is uniform (see section 2.1.2).

2) The electron flux density is considered as uniform and monoenergetic. The electron pulse is considered to be rectangular and of variable duration.

3) The lifetimes of the metastables are considered to be long compared to the flight time (see section 2.2.2).

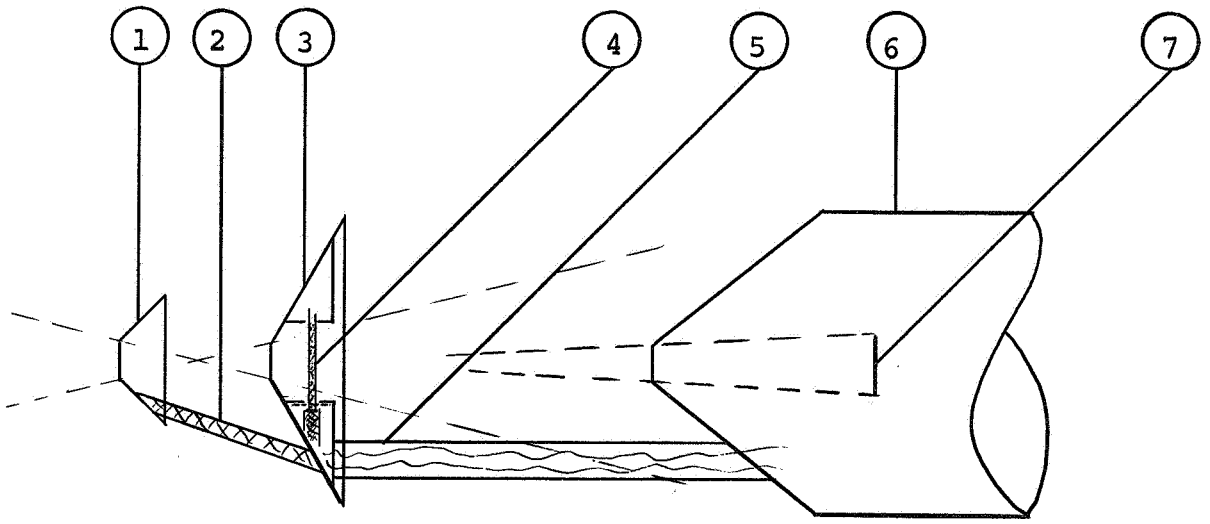

1. Inlet
2. Support web (typ.)
3. Skimmer
4. Electron beam
5. Hollow support (instrument leads)
6. Interface to vehicle
7. Detector

Fig. 20.- Schematic representation of the MTOF detection system.

4) Both elastic and inelastic scattering of the metastable beam are considered to be negligible.

5) The distribution of molecular velocities is described in terms of a drifting Maxwellian gas.

6) Multiple, inelastic electron collisions with any given molecule are assumed negligible.

The basis for the validity of these assumptions, together with a discussion of other parameters (see, for example, sections 2.3.1.2, 2.3.1.3, and 2.3.2) which might influence the MTOF signal, are presented in other sections of the report.

Consider the production rate of metastables within the interaction volume. The molecular velocity is negligible with respect to the velocity of the exciting electrons, and since a very small fraction of the beam molecules is excited, the excitation probability is independent of the electron pulse duration and the molecular drift. However, the electron pulse duration does affect the axial extent of the region containing excited molecules. Consider, for example, an electron pulse of duration Δt_e. The axial extent (at the source) of the region of the beam in which molecules are excited to the metastable state is $U\Delta T_e$, where U is the relative velocity of the sampler with respect to the gas being sampled. This spatial uncertainty directly influences the temporal resolution of the detector signal, the uncertainty being in direct proportion to the ratio of the flight time (ℓ/U) to the electron pulse duration (Δt_e) (this effect will be discussed in more detail in section 3.1.3). Other factors influencing the axial extent of the excitation region must also be minimized and, for this reason, the axial dimension of the electron beam has been limited to a value much smaller than the flight length

(the value chosen was 1%).

The rate of production of metastables can be expressed as

$$\dot{dN^*} = \frac{i_e}{e} P_c \, dx \qquad (3.1.2\text{-}1)$$

where i_e/e is the electron flux passing through the interaction volume and P_c is the electron collision probability per unit path length. Integrating this expression over the total electron path length (λ_e),

$$\dot{N^*} = \frac{i_e}{e} \int_0^{\lambda_e} P_c \, dx \qquad (3.1.2\text{-}2)$$

or

$$\dot{N^*} = \frac{i_e}{e} \int_0^{\lambda_e} \sigma \, n \, dx \qquad (3.1.2\text{-}3)$$

where σ is the total excitation cross-section and n is the molecular density in the interaction volume. Since both σ and n are independent of electron path length (assuming uniform density), Eq. (3.1.2-3) becomes

$$\dot{N^*} = \frac{i_e}{e} \sigma \, n \, \lambda_e \quad . \qquad (3.1.2\text{-}4)$$

Upon multiplying by the electron pulse length (Δt_e), the total number of metastables produced per electron pulse is

$$N^* = \frac{i_e}{e} \sigma n \lambda_e \Delta t_e \ . \qquad (3.1.2\text{-}5)$$

The distribution of speeds represented by this group of N^* metastables is desired, so the number of metastables with velocities between v' and $v' + dv'$ must be determined. The particle velocities are describable as a drifting Maxwellian gas, for which the differential flux density ($d\hat{F}$) into a solid angle $d\omega$ at an angle ϕ with respect to the beam axis is

$$d\hat{F} = n\, v'^3\, f(v) dv'\, d\omega \cos\phi \qquad (3.1.2\text{-}6)$$

where n is the molecular density at the interaction region, v' is the molecular velocity with respect to a frame of reference travelling with the vehicle, and $f(v)$ is the Maxwell-Boltzmann distribution function. The analysis will be limited to small solid angles along the instrument axis for a forward facing probe at zero angle of attack. Under these conditions, the differential flux density is

$$d\hat{F} = \frac{n d\omega}{\pi^{3/2} v_m^3} v'^3 e^{-\left(\frac{v' - U}{v_m} \right)^2} dv' \qquad (3.1.2\text{-}7)$$

where v_m ($v_m \equiv [2kT/m]^{\frac{1}{2}}$) is the most probable thermal molecular speed and U is the vehicle speed. Upon dividing by the relative velocity (v'), the number of particles per unit volume with speeds between v' and $v' + dv'$ which have passed out of the interaction region and are contained in a solid angle $d\omega$ along the axis is found to be

$$dn(v') = \frac{nd\omega}{\pi^{3/2} v_m^3} \; v'^2 \, e^{-\left[\frac{v' - U}{v_m}\right]^2} \; dv' \qquad (3.1.2\text{-}8)$$

Since the time dependence of the signal measured in the MTOF scheme is desired, $dn(v')$ will be transformed from velocity space to the time domain. Letting $v' = \ell/t$, where ℓ is the flight path length, the molecular density for molecules arriving at the detector in the time interval t to $t + dt$ is found from Eq. (3.1.2-8) to be

$$dn(t) = \frac{nd\omega\ell^3}{\pi^{3/2} v_m^3 t^4} \; e^{-\left[\frac{\ell^2}{t^2 v_m^2} - \frac{2\ell U}{t v_m^2} + \frac{U^2}{v_m^2}\right]} \; dt \; . \qquad (3.1.2\text{-}9)$$

Combining Eq. (3.1.2-9) and (3.1.2-5), the number of metastables per electron pulse arriving at the detector, which subtends a solid angle $d\omega$, in time t to $t + dt$ is

$$dN^*(t) = \frac{i_e n\sigma\lambda_e \Delta t_e d\omega\ell^3}{e\pi^{3/2} v_m^3 t^4} \; e^{-\left[\frac{\ell^2}{t^2 v_m^2} - \frac{2\ell U}{t v_m^2} + \frac{U^2}{v_m^2}\right]} \; dt \; . \qquad (3.1.2\text{-}10)$$

Implicit in this equation is the condition that $\Delta t_e << t$. Finally, multiplying by the electron pulse repetition rate (ρ) and the secondary electron emission coefficient (γ), the number of electrons ejected from the detector per unit time is calculated to be

$$\dot{dN}_e(t) = \frac{i_e}{e} n\sigma\gamma\lambda_e \Delta t_e \rho d\omega \frac{\ell^3}{\pi^{3/2} v_m^3 t^4} e^{-\left[\frac{\ell^2}{t^2 v_m^2} - \frac{2\ell U}{t v_m^2} + \frac{U^2}{v_m^2}\right]} dt.$$

(3.1.2-11)

If the detector is the cathode of an electron multiplier used in conjunction with a multi-channel pulse height analyzer, the magnitude of the signal (at the output of the analyzer) is subject to some further constraints. The energy distribution and angular distribution of the electrons ejected from the cathode are such that only a fraction of the total number can be focused into the electron multiplier. Therefore, the signal is dependent on the shape and geometrical arrangement of the cathode with respect to the electron multiplier as well as the experimental operating conditions of the analyzer and electron multiplier. Considering these electrode geometry and electron dispersion effects as an attenuation factor between the cathode and analyzer output and referring to this attenuation factor in terms of detector sensitivity, the counting rate per channel can be written as

$$\dot{dN}(t) = \frac{i_e}{e} n\sigma\eta\lambda_e \Delta t_e \rho d\omega \frac{\ell^3}{\pi^{3/2} v_m^3 t^4} e^{-\left[\frac{\ell^2}{t^2 v_m^2} - \frac{2\ell U}{t v_m^2} + \frac{U^2}{v_m^2}\right]} dt$$

(3.1.2-12)

where $\eta \equiv K\gamma$, η being the detector sensitivity and K the attenuation factor.

3.1.3 MTOF Detection System Sensitivity

In order to calculate the sensitivity of the MTOF detection system, realistic values must be established for the parameters appearing in Eq. (3.1.2-12), which represents the counting rate of the detection system. The discussions to be presented in this section provide the basis for the selection of the numerical values assigned to these parameters, which are collected in tabular form at the end of the section.

Using the data of Holt and Krotkov (ref. 52) for a magnetically focused, space charge limited planar diode, the calculated effective electron current density at the interaction region, for an accelerating potential of 12 V, is 4.65×10^{-3} A/cm^2. The term "effective" current density is used to refer to that portion of the total electron current which actually passes through the interaction region to produce excited molecules.
The resultant value of i_e is, therefore, 7×10^{-4} amperes.

For the MTOF detection system shown schematically in Fig. 20, the following parameters apply:

1. The atmosphere is assumed to be nitrogen gas, the temperature 300°K, and the vehicle velocity (U) 5×10^5 cm/sec.
2. The ratio of the source density to the undisturbed density (n/n_o) is 0.5.
3. The molecular beam diameter is 1 cm.
4. The solid angle subtended by the detector ($d\omega$) is 10^{-2} sr.
5. The flight path length (ℓ) is 15 cm.

6. The equilibrium particle density in the detector region with no pumping is $\simeq 2.5\ n_o$. It is, therefore, probable that some active pumping will be required.

In choosing suitable values for the electron beam pulse duration (Δt_e) and the detector delay gating width or channel width (dt), it is necessary to maximize both since they directly affect the system sensitivity. However, choosing too large a value for either will distort the TOF signal wave form and, hence, the resolution. It is necessary, therefore, to characterize these parameters by a numerical evaluation of the integral representing the time dependent detector signal, taking into consideration the drift of molecules from the interaction region after the start of the electron beam pulse. By considering a finite electron gating pulse length, Eq. (3.1.2-10) may be rewritten to yield the rate of production of metastables with velocities between v' and v' + dv' which were produced during the electron beam pulse of duration Δt_e (where $\Delta t_e < t$ but not necessarily negligible) and which arrive at the detector at time t within dt. The result can be expressed as

$$\dot{dN}^*(t) = \frac{i_e n \sigma \lambda_e d\omega}{e\pi^{3/2} v_m^3} \int_o^{\Delta t_e} \frac{\ell^3}{(t-t')^4} e^{-\left[\frac{\ell^2}{(t-t')^2 v_m^2} - \frac{2\ell U}{(t-t')v_m^2} + \frac{U^2}{v_m^2}\right]} dt' \qquad (3.1.3\text{-}1)$$

where (t-t') is the metastable flight time, t' representing the drift time of the metastable after formation. Eq. (3.1.3-1), therefore, is an evaluation of the effect of the electron pulse duration on the signal wave form. It has been assumed that the electron beam pulse can be represented by a rectangular pulse.

After integration, Eq. (3.1.3-1), representing the number of metastables per sec arriving at the detector at time t within dt, having been produced during an electron pulse of duration Δt_e, becomes

$$\dot{dN}^*(t) = \frac{i_e n \sigma d\omega \lambda_e}{e\ \pi^{3/2}} \left\{ \frac{\sqrt{\pi}}{2} \left(\frac{U^2}{v_m^2} + \frac{1}{2} \right) \left[\operatorname{erf}\left(\frac{U}{v_m} - \frac{\ell}{t v_m} \right) - \operatorname{erf}\left(\frac{U}{v_m} - \frac{\ell}{(t-\Delta t_e) v_m} \right) \right] \right.$$

$$\left. + \frac{1}{2}\left(\frac{U}{v_m} + \frac{\ell}{t v_m} \right) e^{-\left(\frac{\ell}{t v_m} - \frac{U}{v_m} \right)^2} - \frac{1}{2}\left(\frac{U}{v_m} + \frac{\ell}{(t-\Delta t_e) v_m} \right) e^{-\left(\frac{\ell}{(t-\Delta t_e) v_m} - \frac{U}{v_m} \right)^2} \right\} \qquad (3.1.3\text{-}2)$$

In the limiting case where $\Delta t_e \ll t$, Eq. (3.1.3-2) reduces to Eq. (3.1.2-10).

The signal amplitude is an increasing function of the beam pulse duration Δt_e. It is important, however, that the temperature information contained in the signal not be affected by the changes in Δt_e. Eq. (3.1.3-2) was evaluated numerically for values of Δt_e ranging from 10^{-9} sec to 2.5×10^{-5} sec so that the maximum value of Δt_e, consistent with the preservation of an undistorted signal wave form, could be deduced. The results are presented in Fig. 21 where the data has been multiplied by powers of 10, as noted in the key, so that all data may be included on the one graph. It can be seen that, although the magnitude of the pulse amplitude increases proportionally with Δt_e from 10^{-9} sec up to 10^{-7} sec, the pulse shape does not change so that

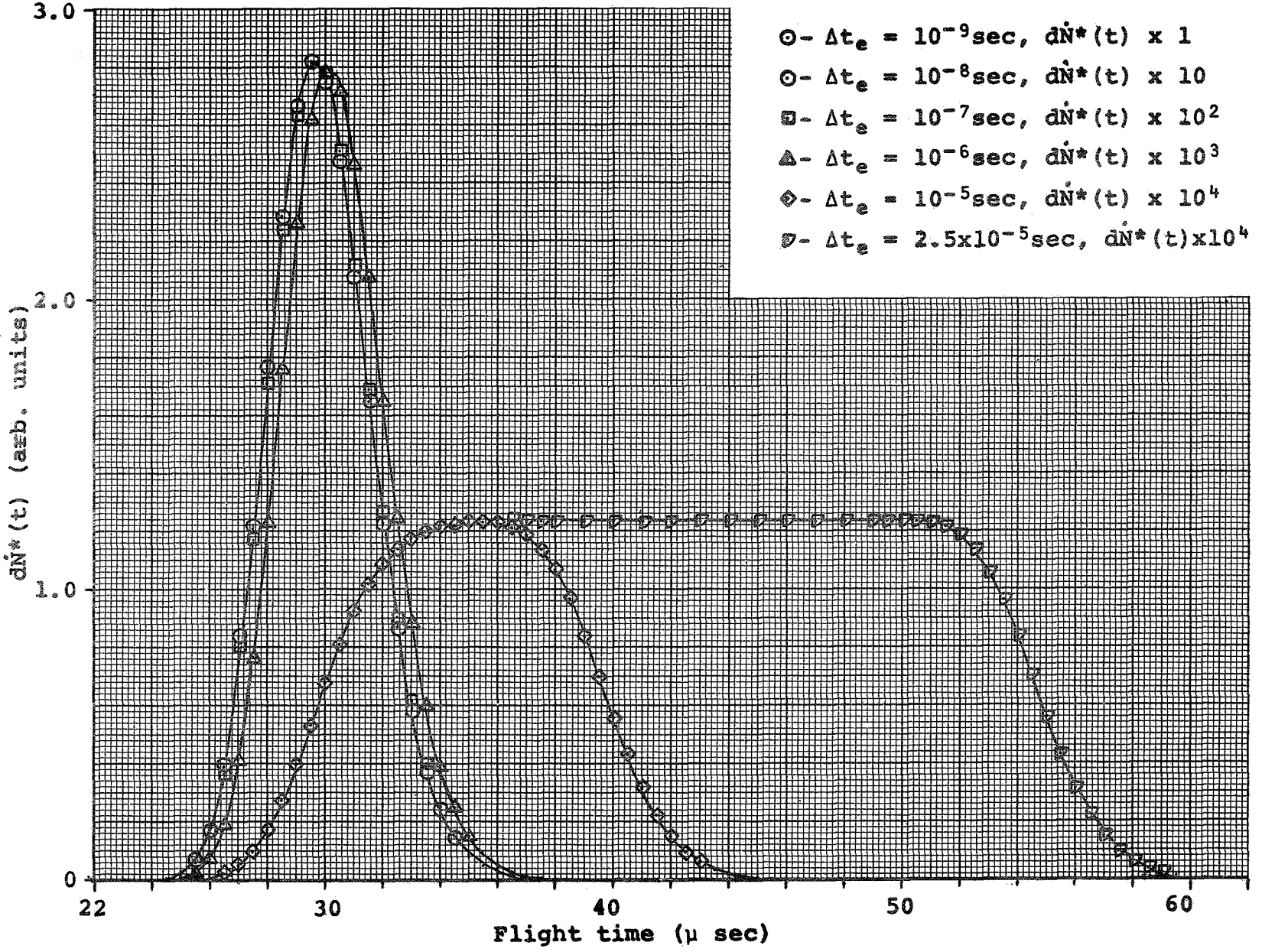

Fig. 21.- Variation of the time-of-flight signal with electron beam pulse duration.

the temperature information contained in the signal is not affected by changes in Δt_e over this range. As Δt_e is increased further, the pulse shape is distorted until finally the amplitude reaches a constant value representative of continuous rather than pulsed operation. Therefore, at some value around 10^{-6} sec, the direct measurement of temperature in terms of the signal wave form is beginning to be obscured. The maximized value chosen for the electron beam pulse duration (Δt_e) was 2×10^{-7} sec.

To investigate the manner in which the TOF signal wave form changes with temperature, data were generated for the pulse shape and amplitude at constant conditions except for a temperature increase of 30°K. The result, as shown in Fig. 22, is that the pulse shape is broadened and shifted slightly in time and the amplitude is decreased. It will be shown in a subsequent section that the peak shift is minor in comparison with the pulse broadening and amplitude change, so that peak shift is a less sensitive indicator of the temperature than the pulse shape. In addition, the detection of the peak shift requires a detector channel width smaller than the shift to be measured, which in the case cited in Fig. 22 is only 40 nsec. Not only would this reduced channel width (dt) decrease the measurement sensitivity, but also there is some question whether equipment to perform this rapid switching and counting is within the state of the art. On the other hand, both the pulse shape and peak height can be established accurately using presently attainable detector channel widths, thus increasing the sensitivity.

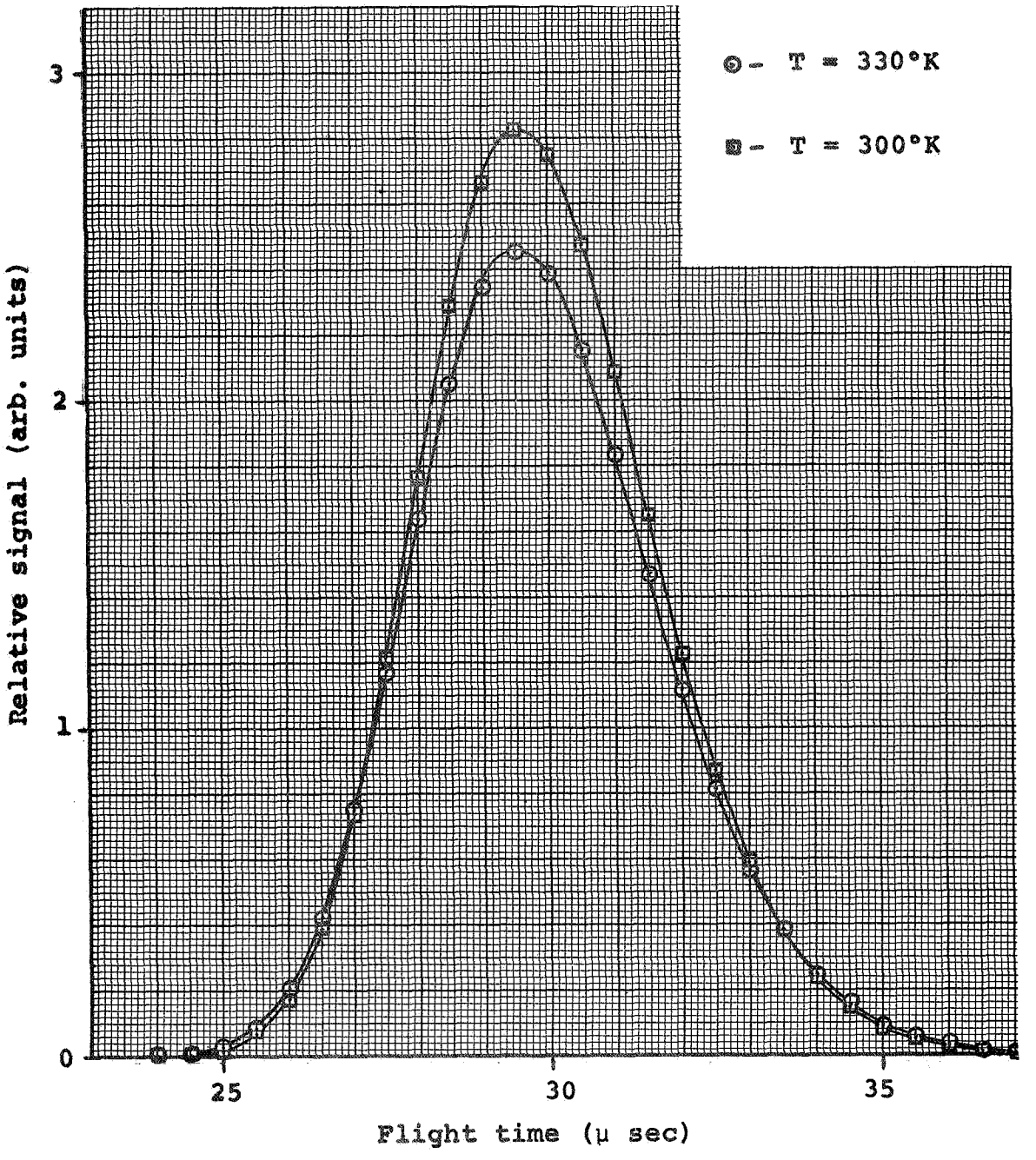

Fig. 22.- Variation of the time-of-flight signal with temperature

The data presented in Fig. 22 for the TOF wave form for a high speed probe can be compared with the TOF wave form for a thermal beam presented in Fig. 23. The influence of an increase in the gas temperature of 30°K is to be compared in the two cases. For the high speed case, the temperature increase and its effect on the speed ratio ($S \equiv U/v_m$ or $U[m/2kT]^{\frac{1}{2}}$) has a major influence on the shape of the TOF signal but little effect on the flight time. The TOF signal is broadened and decreased in amplitude. In the thermal beam case ($U = 0$), on the other hand, the increased temperature leads to not only a distortion in signal shape, including an increase in peak amplitude, but also a significant change in flight time measured with reference to the peak.

The TOF signal, given by Eq. (3.1.3-2), is a function of both vehicle speed U and ambient gas temperature through v_m. For the case of constant temperature and varying vehicle speed, the calculations of Zorn and Pearl (ref. 48), presented in Fig. 24, may be consulted. These data indicate the changes in the TOF wave form for molecular nitrogen at a constant temperature of 900°K, while the vehicle speed is varied such that the speed ratio changes from 2 to 15. These characteristics are suggestive of the results from a rocket experiment in that there are substantial changes in the vehicle speed along the trajectory, especially near the apex where the speed ratio is reduced almost to zero. On the other hand, for a satellite experiment, the vehicle speed remains rather constant while the speed ratio is altered by changes in the temperature. To indicate how the TOF wave form changes under these conditions, two typical values for the vehicle speed were chosen (5 and 8 km-sec^{-1}), and the relative TOF signals were calculated for molecular nitrogen temperatures from 300 to 900°K; the results are presented in Fig. 25. From the data of

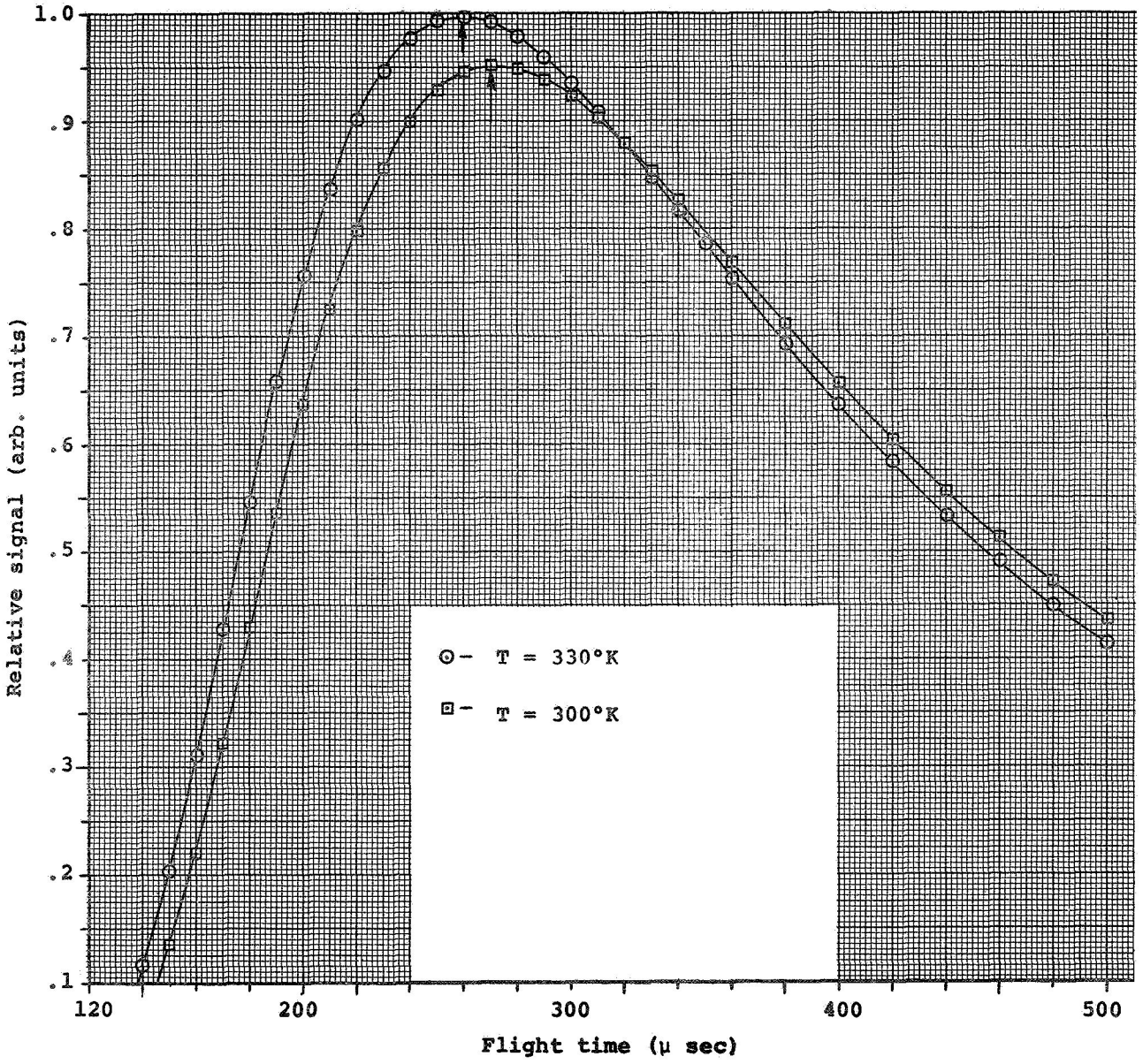

Fig. 23.- Variation of the time-of-flight signal with temperature for a U=0 beam.

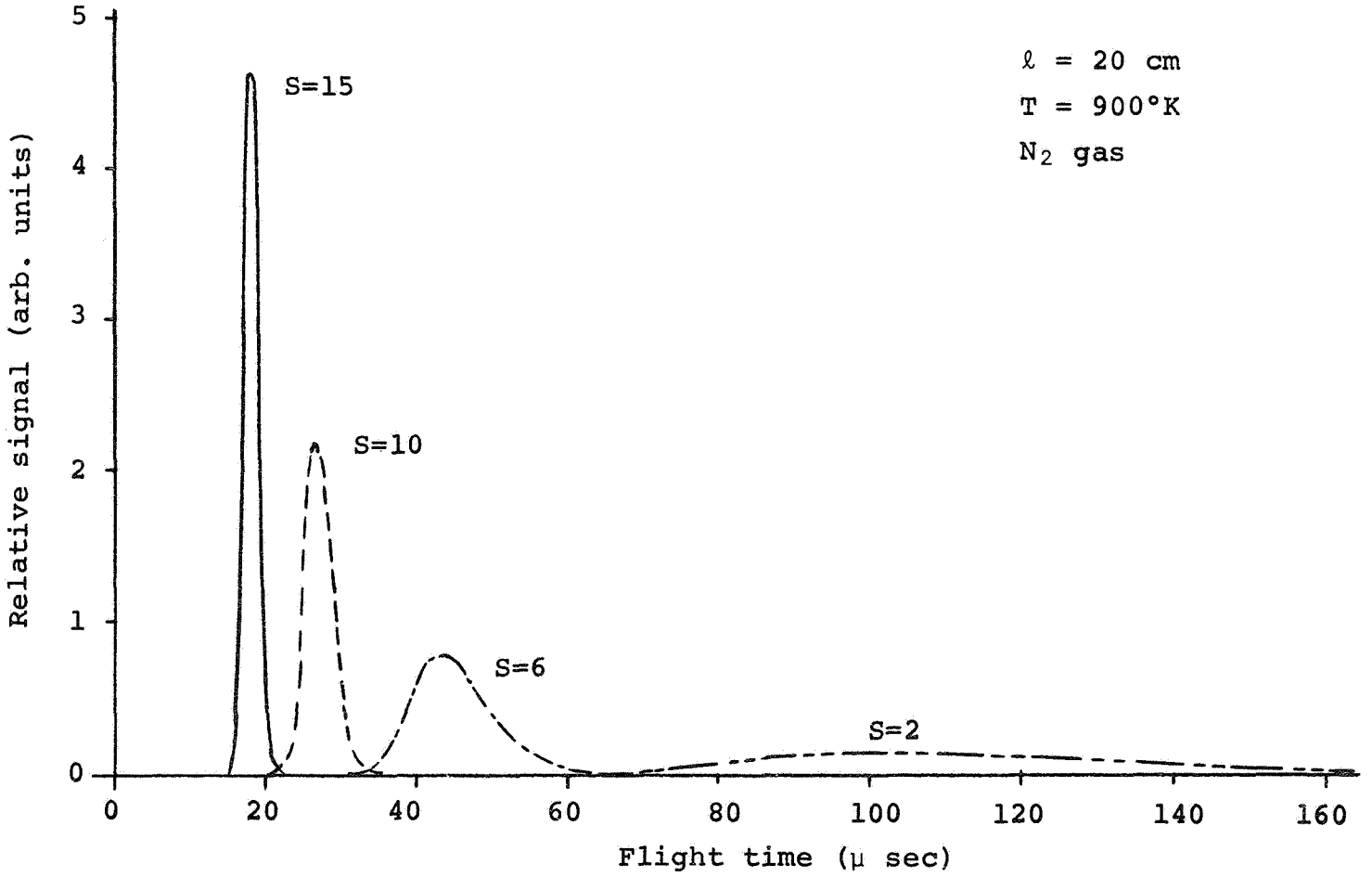

Fig. 24.- Variation of the time-of-flight distribution with speed ratio at constant temperature (ref. 48).

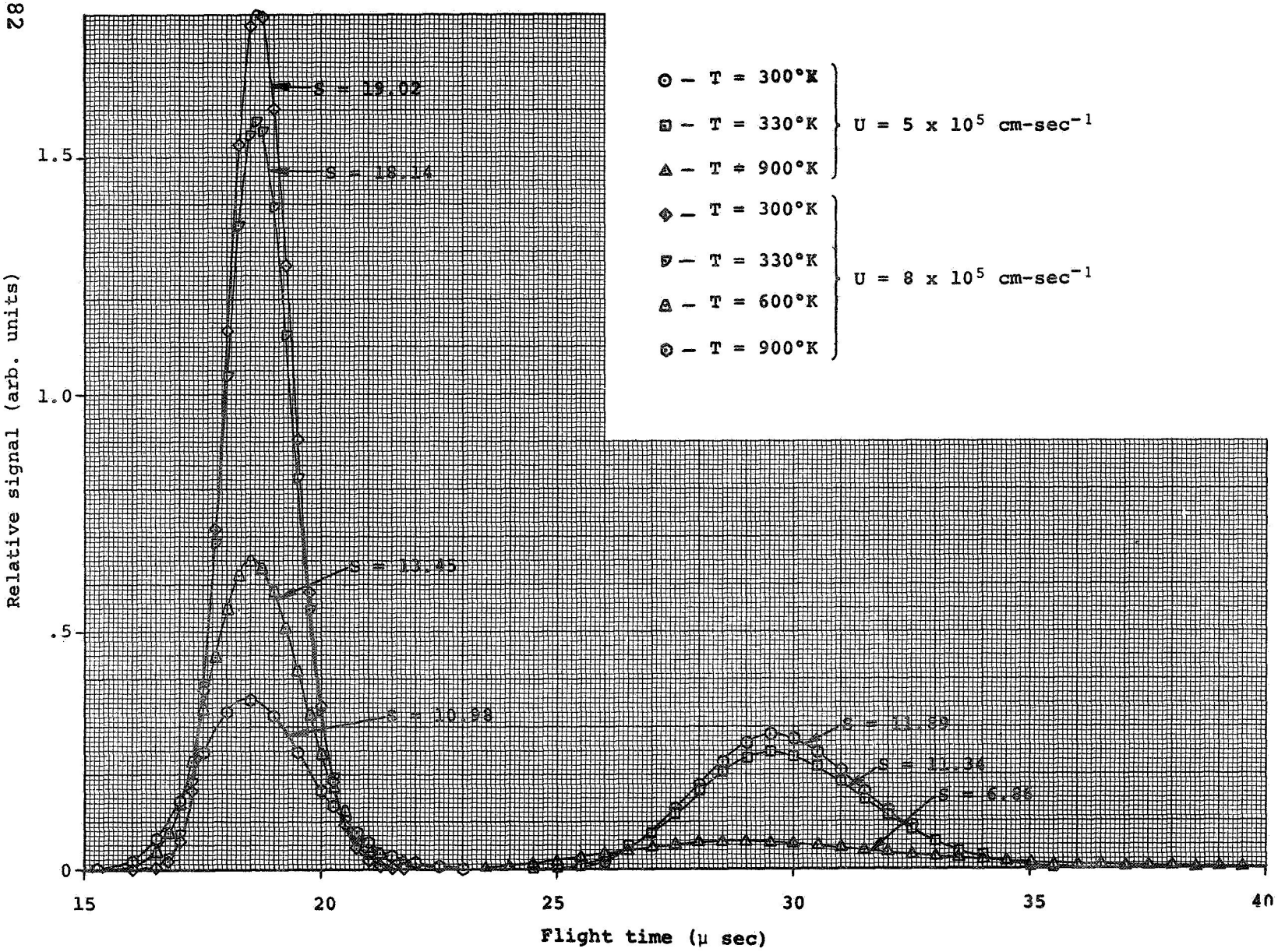

Fig. 25.- Variation of the time-of-flight distribution with speed ratio at constant vehicle speed.

Figs. 24 and 25, it can be seen that the flight time or position of the TOF signal in time space is primarily controlled by the vehicle speed, and the shape of the pulse is controlled by the speed ratio which, for a given vehicle speed, is only a function of the gas temperature. One can also obtain from the figures an appreciation of the extreme demands placed upon the time resolving electronic instrumentation in order to obtain sufficient signal resolution for a high speed vehicle measurement in comparison with that required, for instance, in the case of the thermal beam measurements by Locke and French (ref. 10).

From the data of Fig. 25, in which the TOF signals are shown for temperatures of 300 and 330°K, the temperature resolution provided by the TOF detection method may be obtained. Since the data analysis techniques for establishing the correlation between peak shape and temperature have not as yet been fully developed, a simplified approach was used to estimate the temperature resolution as a function of temperature. The estimate of the pulse shape used was the ratio of peak height to peak width at half maximum (referred to as S), and this data is plotted as a function of temperature; the results are presented in Fig. 26. The data in the region of interest for thermospheric temperature measurements are found to fit an equation of the form

$$\log S = 2\log T + C. \qquad (3.1.3\text{-}3)$$

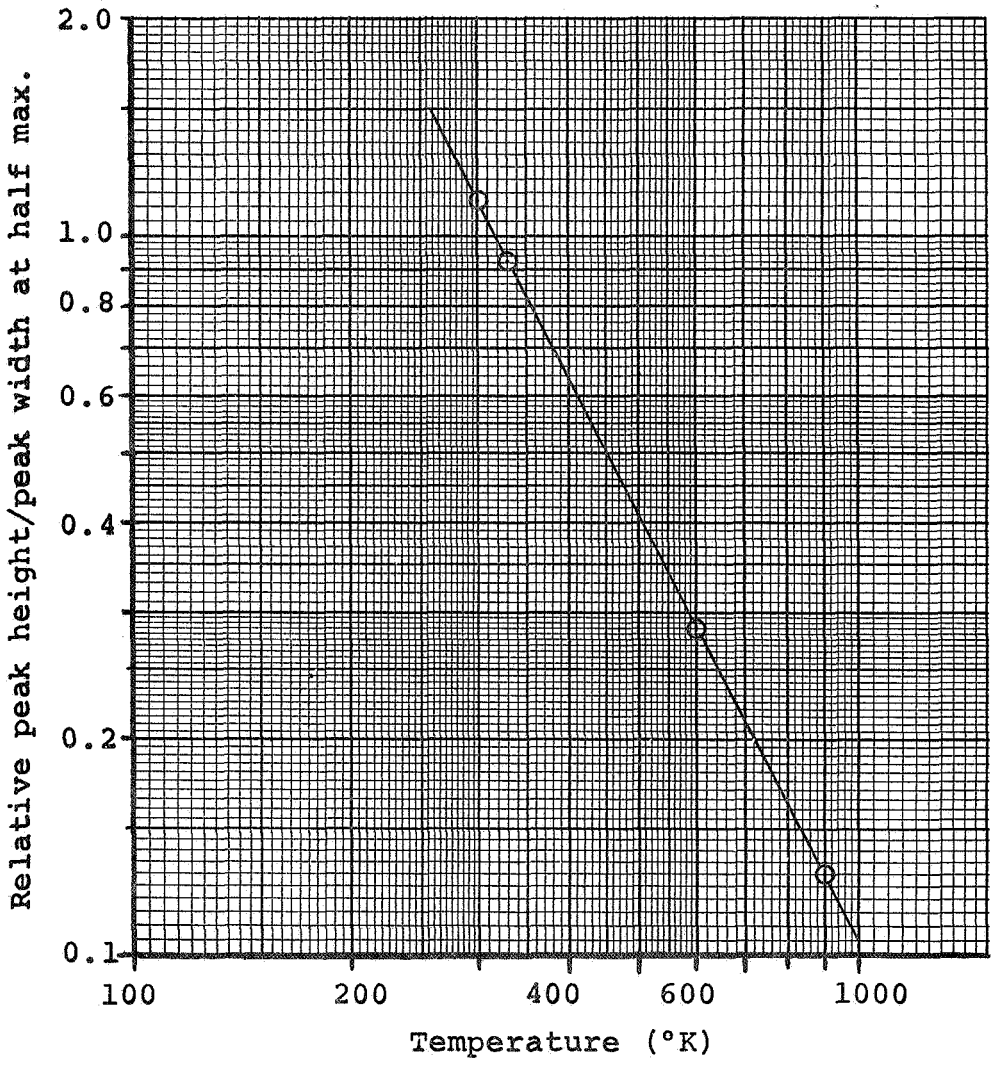

Fig. 26.- Variation of the relative ratio of peak height to peak width at half maximum with temperature.

It is estimated that the peak shape is known to within an accuracy of 11% with a confidence level greater than 99%.* To find the relative probable error in temperature ($\Delta T/T$) resulting from a relative probable error in the ratio of peak height to peak width at half maximum ($\Delta S/S$), Eq. (3.1.3-3) may be differentiated to yield

$$\left|\frac{dT}{T}\right| = \frac{1}{2}\left|\frac{dS}{S}\right| \quad . \qquad (3.1.3\text{-}4)$$

Thus, for the assumed 11% relative probable error in S, which would result from having no greater than 4550 counts at the one half peak amplitude point, it is seen that a relative probable error in temperature measurement of 5.5% is attainable with the MTOF detection scheme. Further analysis with other curve fitting schemes is necessary to establish whether greater accuracy can be attained.

---

*As shown by Evans (ref. 53), it may be concluded that a mean derived from n counts from a binomial distribution differs by no more than $270/\sqrt{n}\%$ from the tru mean for a confidence level greater than 99%. Thus, for a confidence level greater than 99%, the total number of counts required at each half peak amplitude point, for 4% relative probable error of each (total of 8%), is $n = (270/4)^2 = 4550$ counts.

As was indicated earlier, the shift of the peak of the distribution is a less sensitive measure of the temperature than the relative peak shape. Using 8×10^5 and 5×10^5 cm-sec^{-1} as typical vehicle speeds, calculations of the peak shift with temperature were performed. Presented in Fig. 27 are the data for the flight time at the peak of the TOF distribution as a function of temperature. The nearly linear relationship for $U = 8 \times 10^5$ cm-sec^{-1} yields a slope of 3.32×10^{-10} sec-°K^{-1} and although the curve for $U = 5 \times 10^5$ cm-sec^{-1} is not linear, it can be seen that the slope of this curve at any temperature is about four times greater than for the higher speed case. However, even for $U = 5 \times 10^5$ cm-sec^{-1}, which has the highest sensitivity, in order to measure T to an accuracy of 4% at 300°K, it would be required to measure a peak shift as small as 16 nsec, which is not possible using present state-of-the-art detecting and counting circuits.

Referring to Fig. 21, it can be seen that the entire TOF signal is only 14 μsec wide at the base and has a significant magnitude for only 8 or 9 μsec. The choice of a detector channel width (dt) which is narrow enough for the necessary time resolution will result in a compromise between the desirable resolution and the minimum channel width attainable. Intrinsic limitations involved in the final compromise will be the detector time constant, which results from the finite transit time of the electron pulse through the electron multiplier, and the time constant associated with the electronic switching from one detection channel to the next. The transit time and the switching time are functions of the actual hardware which will be chosen for the flight detection system, but for this analysis dt has been chosen to be representative of the smallest value achievable with present flight instrumentation.

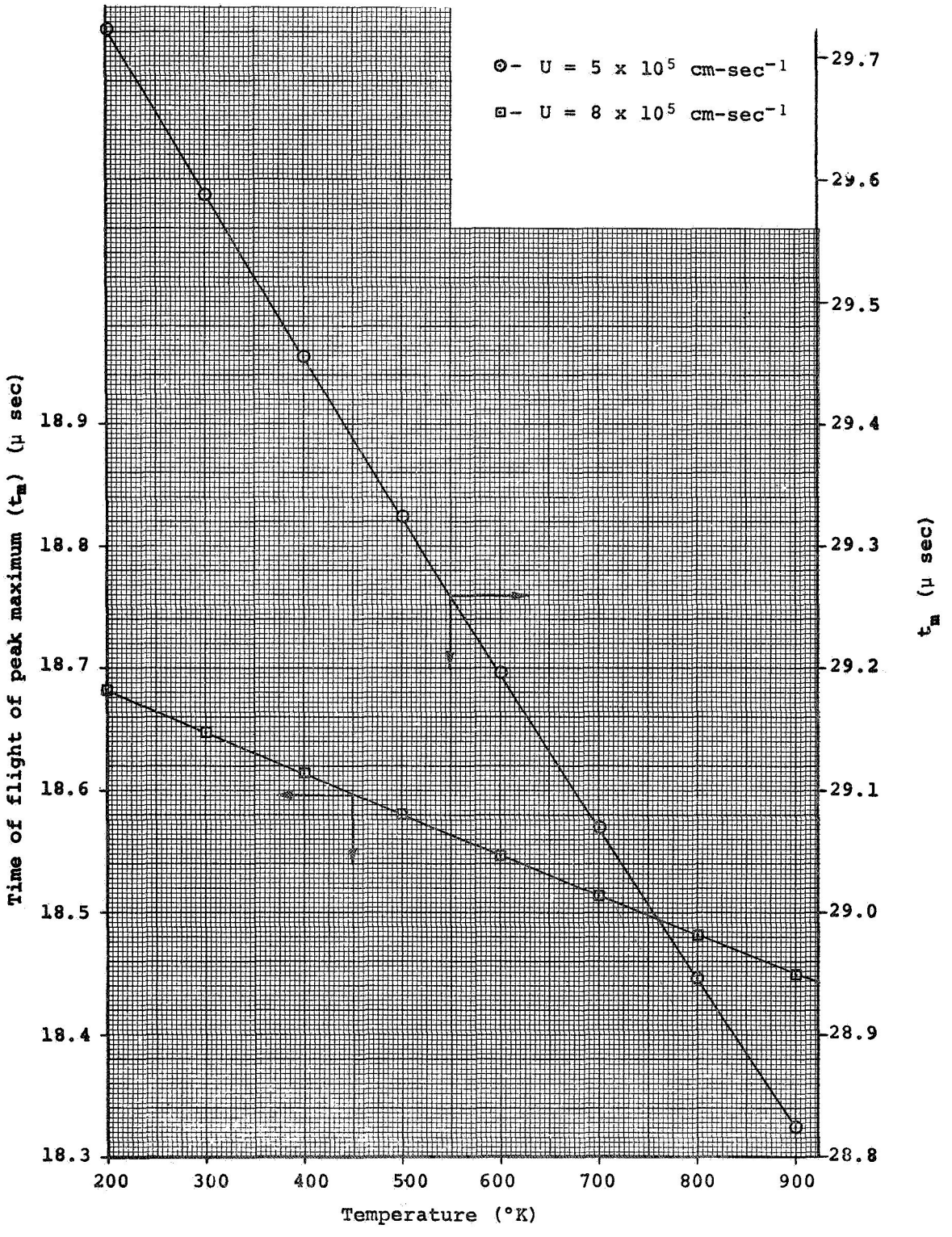

Fig. 27.- Variation of peak shift with temperature for vehicle speeds of 5 and 8 km-sec^{-1}.

Sufficient data is now available to estimate the system sensitivity by calculating the counting rates, based on the established estimates of the parameters appearing in Eq. (3.1.2-12). The counting rate at the peak of the TOF distribution will be used in defining the system sensitivity. The value of t corresponding to the peak is obtained by standard techniques of analytical calculus and yields:

$$t_m = \frac{\ell\left[- U \pm (U^2+8v_m^{\,2})^{1/2}\right]}{4v_m^{\,2}} \qquad (3.1.3\text{-}5)$$

which, for S>>1 , can be approximated as

$$t_m \approx \frac{\ell}{U}\left[1 - \frac{2}{S^2}\right] . \qquad (3.1.3\text{-}6)$$

Upon inserting this value of t_m in Eq. (3.1.2-12), the counting rate at the peak of the TOF distribution is found to be

$$[\dot{dN}^*(t)]_{max} = \frac{i_e}{e\pi^{3/2}}\, n\sigma K\gamma\lambda_e \Delta t_e\, \rho d\omega\, \frac{S^3 U}{\ell(1 - 8/S^2)}\, e^{-4/S^2}\, dt \qquad (3.1.3\text{-}7)$$

Maximized values of the parameters used to calculate the counting rate at the peak of the TOF distribution according to Eq. (3.1.3-7) are presented in Table II. In order to establish what a typical counting rate would be, a calculation was first

TABLE II

Estimated values of the parameters affecting the MTOF system sensitivity

PARAMETER	ESTIMATED VALUE	REMARKS
i_e	7.0×10^{-4} amperes	
n	$0.5\ n_o\ cm^{-3}$	
σ	$5 \times 10^{-17}\ cm^2$	N_2 gas*
γ	4×10^{-2} elect/metastable	W cathode**
K	0.5	Taken from ref. 10
λ_e	.785 cm	
Δt_e	2×10^{-7} sec	
ρ	$7 \times 10^{4}\ sec^{-1}$	
$d\omega$	10^{-2} sr	
ℓ	15 cm	
U	5×10^{5} cm/sec	
dt	10^{-7} sec	

*see section 2.2.2

**see section 2.3.2

made for a temperature of 300°K and for a vehicle speed of 5×10^5 cm-sec^{-1}. Since 300°K corresponds to the temperature of the thermosphere near 120 km, an atmospheric density of 5×10^{11} cm^{-3} was chosen, in accordance with the Spring/Fall Model (ref. 54). With these parameters, the counting rate at the peak of the TOF distribution is

$$[\dot{dN}^*(t)]_{max} = 1.25 \times 10^5 \text{ counts/sec.} \qquad (3.1.3\text{-}8)$$

Before extrapolating to lower densities, it is necessary to examine what the above counting rate implies and also to establish what counting rate is required in order to determine the distribution with sufficient accuracy that the temperature can unambiguously be determined. Following the argument in the footnote of page 85 , for greater than 99% confidence that there is a relative probable error no greater than 4% in the counting rate corresponding to the detection channel measuring the TOF distribution at half maximum, the counting rate at the peak of the distribution must be approximately 9000 counts/sec and the probable error associated with this counting rate will be about 3%. As stated earlier, this total error of 11% in TOF distribution shape leads to 5.5% error in temperature determination.

The upper altitude limit for operation of the system, with the latter estimated error, depends on both the ambient density and speed ratio, which decreases as altitude increases for the same vehicle speed. Calculations were made of the upper limit using the Spring/Fall Model (ref. 54) and are presented in Fig. 28 as a bar graph showing the range of operation of the MTOF temperature detection scheme. The lower altitude limit in these cases

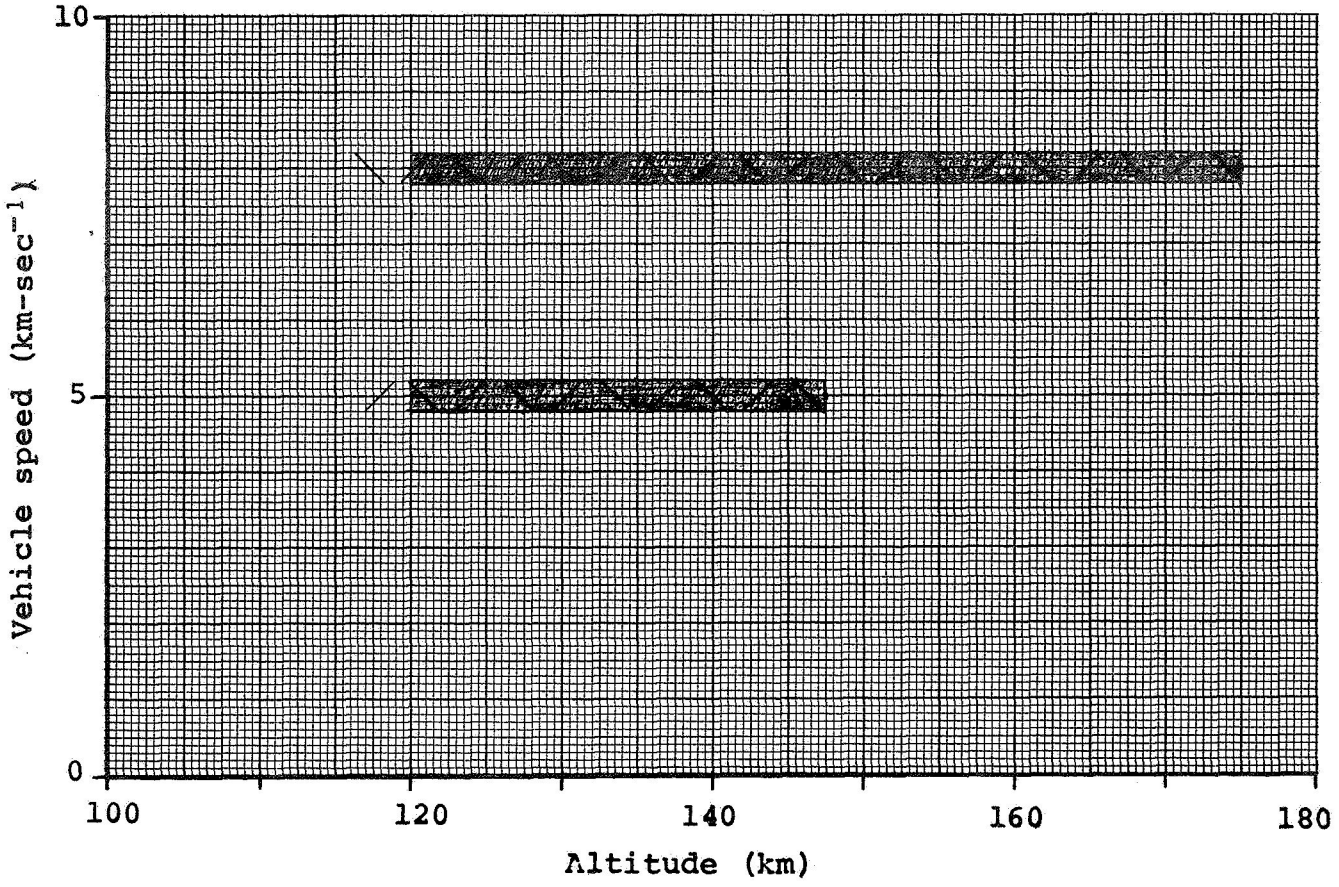

Fig. 28.- Range of MTOF detection system as a function of vehicle speed.

is determined by vehicle and instrument limitations. In the case of a satellite, the minimum perigee is limited to approximately 120 km and in any case the approach to transition flow occurs at approximately 100-110 km, depending on the vehicle dimensions.

3.2 FLUX ANGULAR DISTRIBUTION ANALYSIS

One of the basic characteristics of the flux transmitted through the inlet system of a high speed vehicle is that the differential flux into a given solid angle is a function of the speed ratio ($S \equiv U/v_m$) and is, therefore, inversely proportional to T since $v_m = (2kT/m)^{\frac{1}{2}}$. For decreasing values of the vehicle speed (U) and correspondingly lower values of S, the flux distribution is less dependent on the relative motion of the vehicle and more dependent on the thermal motion of the molecules. One would expect, therefore, that the flux distribution would be more diffuse for lower values of S and become increasingly lobe-like as S increases. This is, in fact, what happens and it is this character of the spatial distribution which yields information concerning the temperature of the gas, assuming that U is known.

In this section, the temperature dependence of the spatial distribution of the total transmitted flux will be considered. A measurement technique which will provide the necessary temperature information either by measuring the change in the magnitude of the differential flux into a fixed solid angle or by measuring the angular distribution of the flux as a function of solid angle will be analyzed. The former measurement requires constant or known detector sensitivity over the range of densities of the measurements, since the temperature information is determined from the relative change of the axial flux with speed ratio, the change in the speed

ratio arising as a result of the dependence of v_m on T. Since these measurements are made under changing inlet conditions, additional information concerning the total density and composition are necessary to compute the temperature. In the latter case, the measurement of the angular distribution, one requires only that the detector sensitivity remain constant during a given measurement, which can be made under constant inlet conditions. The temperature information is derived from the relative slopes of the angular distribution curves as a function of speed ratio.

For an inlet system similar to the one discussed in the previous section, consider the transmitted flux as though it is projected on a plane displaced a distance ℓ from the exit orifice of the skimmer. The data required is the differential flux contained in an element of solid angle $d\omega$ displaced from the system axis at an angle ϕ and passing through the plane at ℓ. Using a previously developed computer program (ref. 13), values of $dF/d\omega$ for various values of T were computed. Since these computations reflect the input parameters chosen for the calculations, they apply to a specific inlet geometry and inlet density. The input parameters used were: 1) $U = 4 \times 10^5$ cm/sec, 2) $n_o = 5 \times 10^{15}$ cm^{-3}, 3) molecular weight = 44, and 4) inlet radius = 5×10^{-3}cm. Presented in Fig. 29 are the computed results for $dF/d\omega$ as a function of ω for temperatures from 150 - 1000°K. It can be seen that there is a dependence of the axial flux on T as well as a dependence of the rate of change of $dF/d\omega$ on T. However, as discussed above, the more appropriate measurement to make is the angular distribution, since it is an instantaneous measurement under constant inlet conditions. Therefore, the remainder of the discussion will be limited to that measurement.

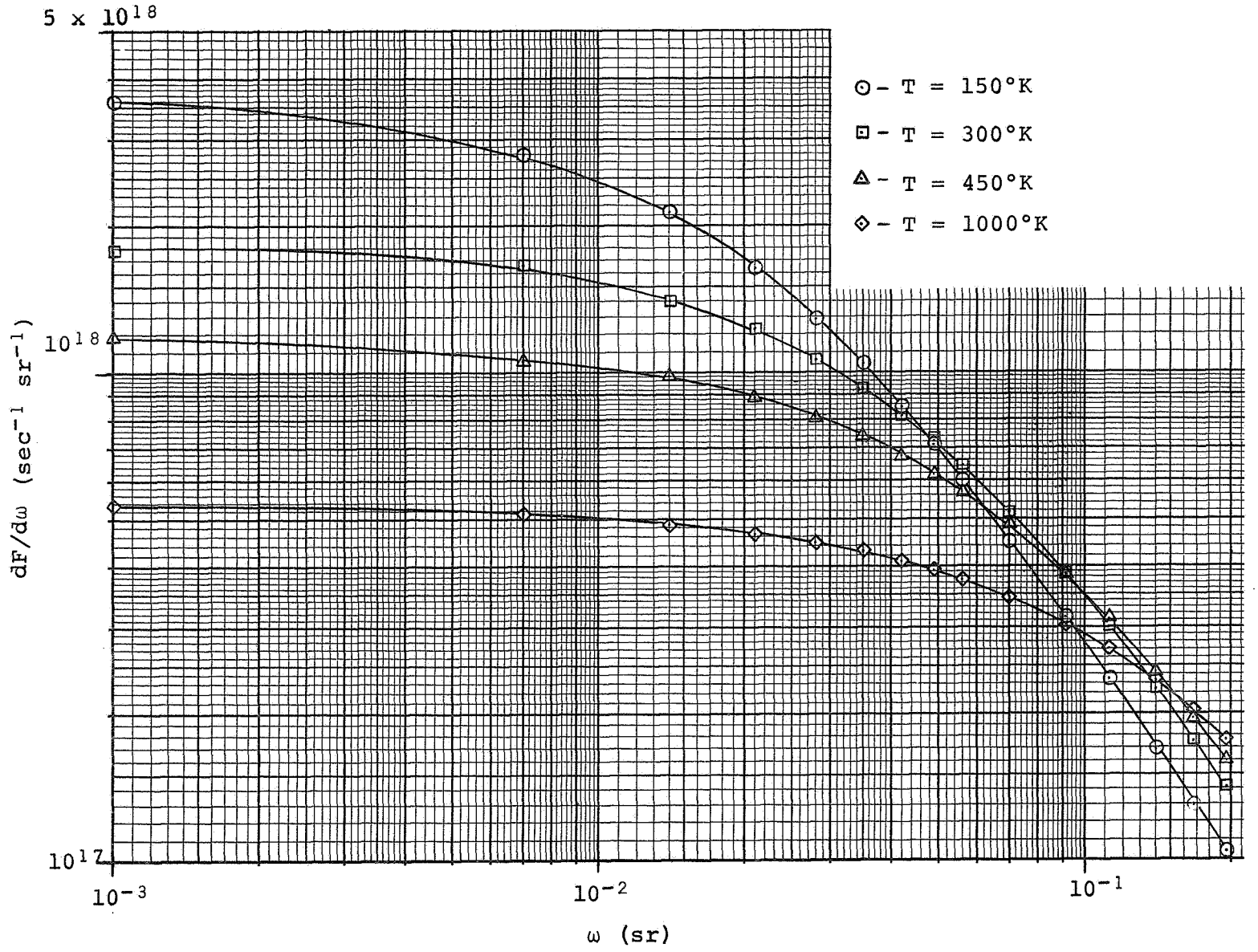

Fig. 29.- Variation of $dF/d\omega$ vs ω with temperature.

To visualize the dependence on T, each of the curves of Fig. 29 has been normalized with respect to the axial magnitude of $dF/d\omega$, and these curves are presented in Fig. 30. To express the data explicitly in terms of T, the data of Fig. 30 has been replotted as normalized flux per unit solid angle as a function of T and are presented in Fig. 31. It can be seen that the greatest temperature sensitivity occurs at the lower temperatures and for the larger solid angles. The limitation on choosing yet larger solid angles is that the signal is decreasing rapidly.

In considering possible methods for measuring the angular distribution of the flux, it must be realized that the requirements for choosing a suitable detection system are quite different than in the previous discussion. Some of these considerations are as follows:

1. In contrast to the previous detection system, which required good axial resolution, this measurement requires good radial resolution.

2. Since this is a differential measurement with respect to the spatial coordinates only, it being an integral measurement with respect to the velocity coordinates, the detector can be a continuously operating flux or density detector.

3. Since measurements are to be made at rather large solid angles, either the skimmer diameters and locations must be such as to prevent exterior molecular flux from impinging on the detector entrance apertures or the volume between the skimmer and the detector plane enclosed. This

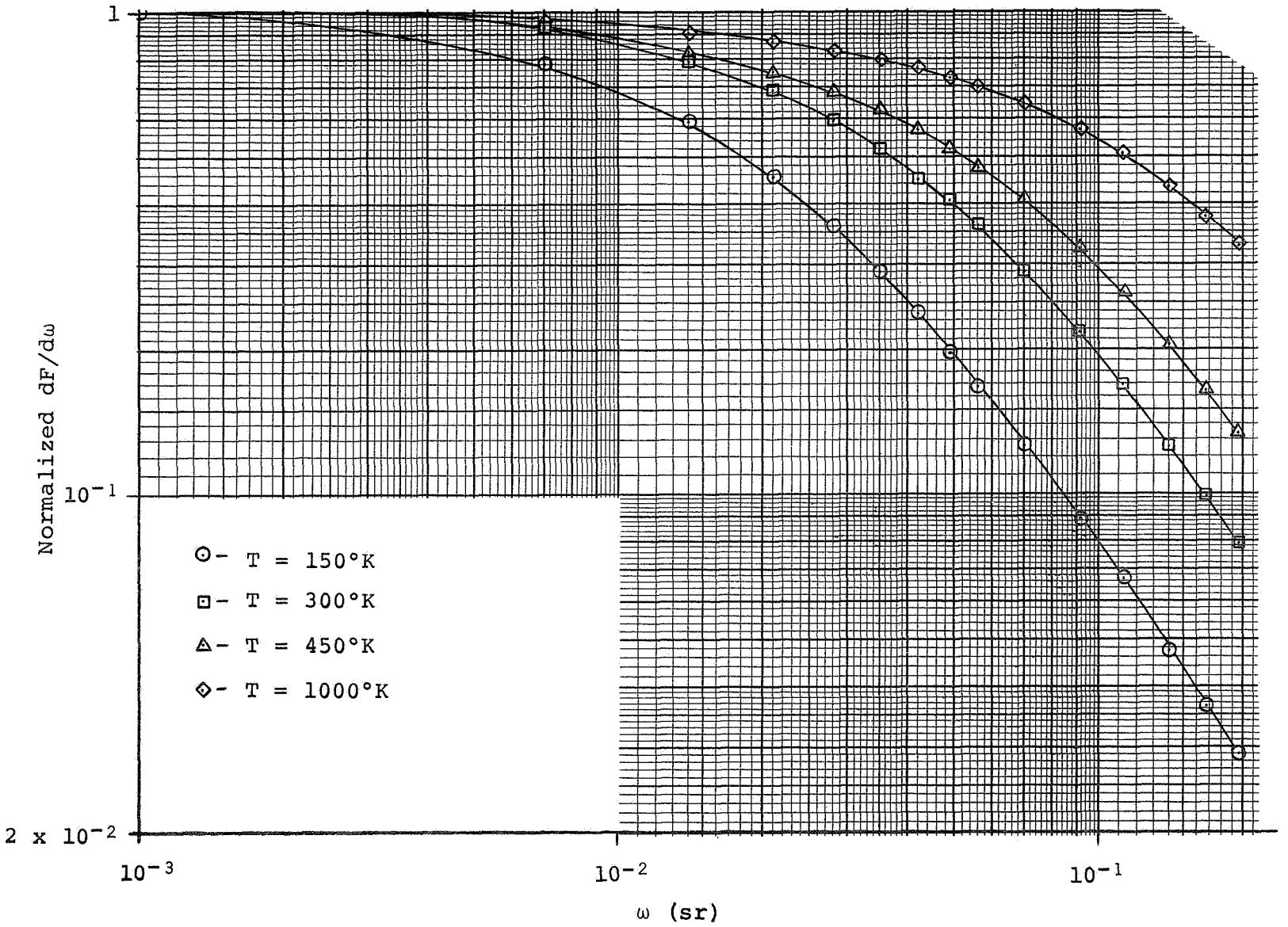

Fig. 30 .- Variation of dF/dω (normalized with respect to the axial value of dF/dω) with ω.

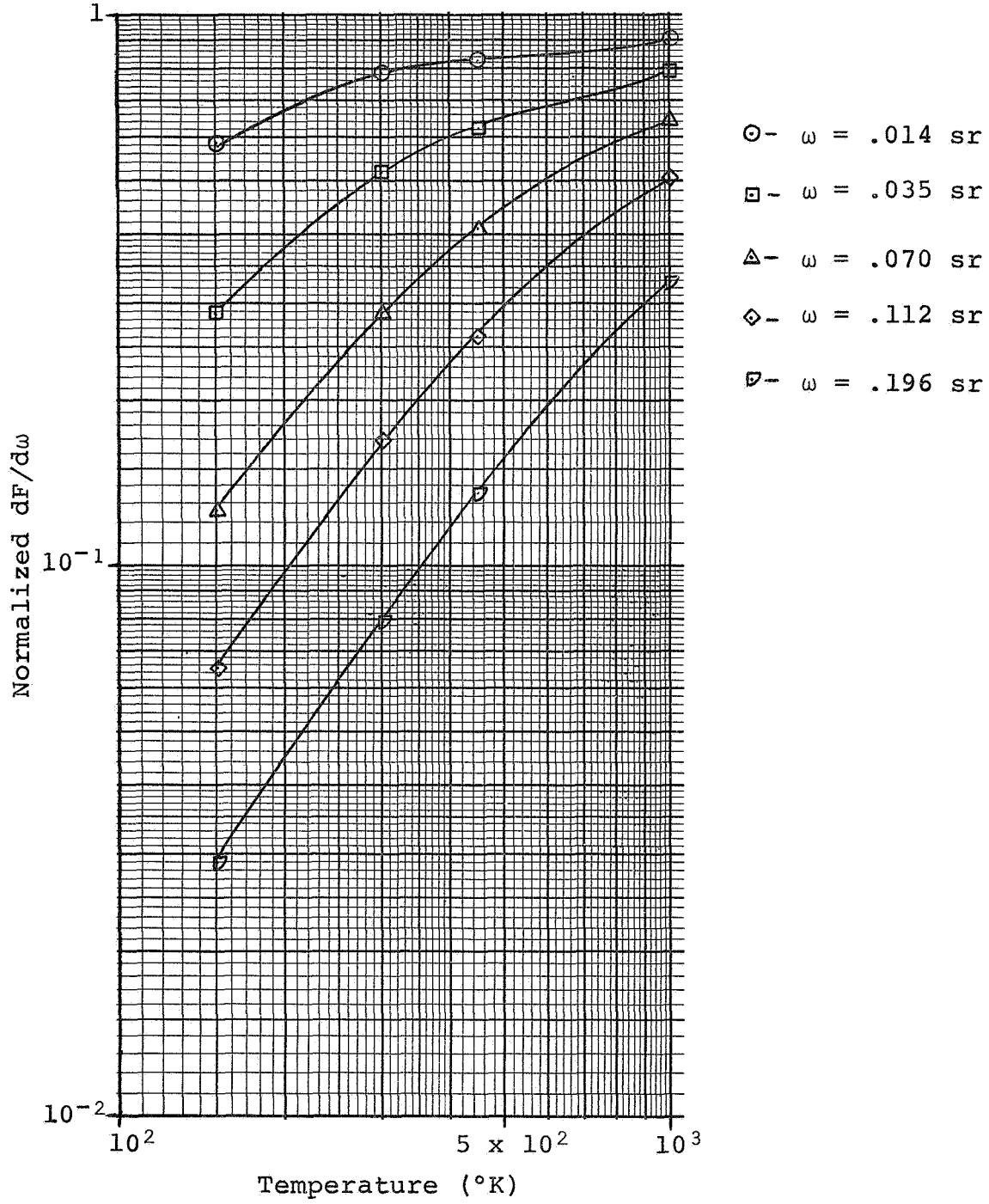

Fig. 31.- Normalized dF/dω vs temperature.

latter choice, of course, requires that the volume be pumped since, otherwise, the scattered gas density would be more than an order of magnitude greater than the unscattered beam density.

4. If total density detectors are used, precautions must be taken to prevent scattering of the flux at the grids and other electrodes.

Three possible detection schemes for establishing the angular flux distribution will be considered, each of which has essentially the same components except that the geometry of the collimating apertures is arranged differently in each case. Therefore, the arrangement of the components is shown only once and is presented schematically in Fig. 32 as a side view. To indicate the difference in the systems, a front view of the detector plane is shown for each detection system in Fig. 33 (a), 33 (b), and 33 (c). The system in Fig. 33 (a) utilizes a number of stationary, total density detectors arranged in a mosaic pattern. The signal of each, when normalized with respect to that of the axial detector, allows an instantaneous representation of the radial flux distribution. The system in Fig. 33 (b) is also a total density device, but the distribution is established by scanning the detector radially. The system represented in Fig. 33 (c) utilizes an array of flux detectors, such as thin foil enthalpy detectors or thermoelectric or pyroelectric detectors. Since flux detectors are sensitive to radiant energy inputs, the system must provide additional shielding from exterior radiant energy.

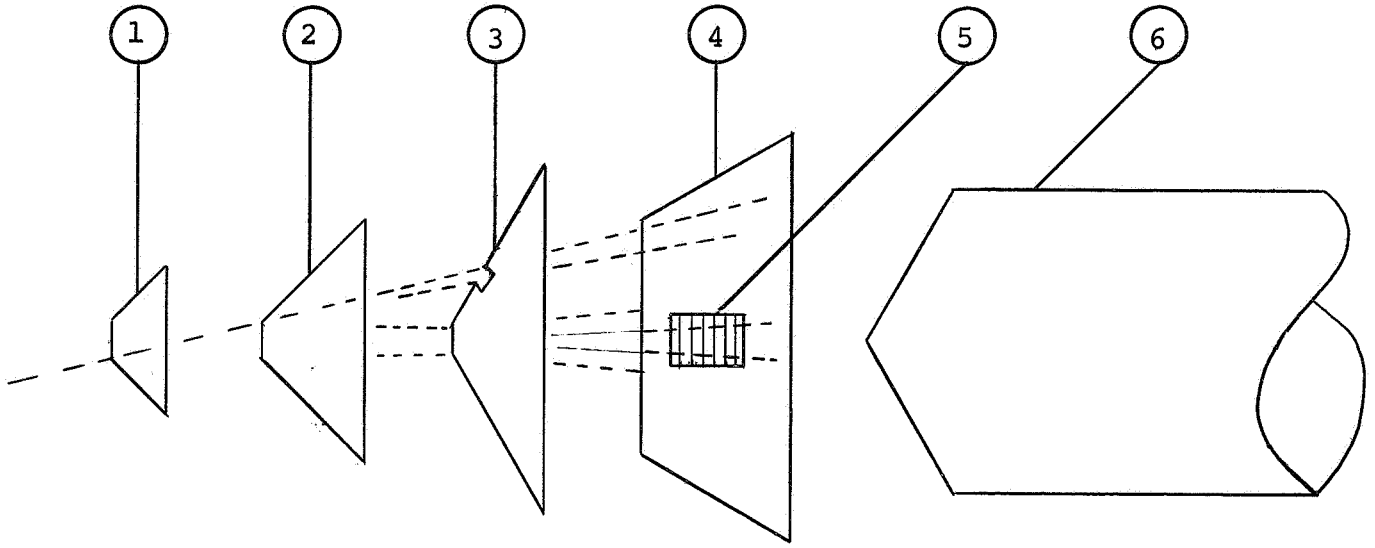

1. Inlet
2. Skimmer
3. Collimator I
4. Collimator II
5. Total density detector (typ.)
6. Interface to vehicle and instrumentation

*Support webs not shown

Fig. 32.- Schematic representation of an angular flux distribution measurement system.

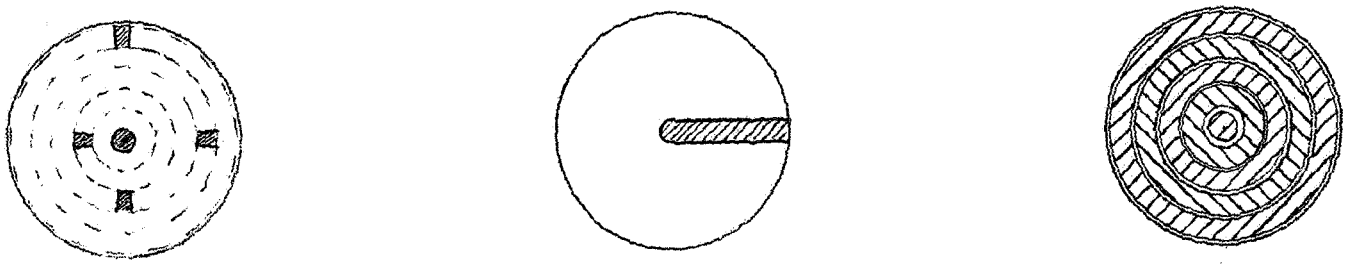

Fig. 33.- Schematic representation (front view) of the detector plane for the angular flux distribution measurement systems.

Estimates of the detector signal for the geometrical arrangement as shown in Fig. 33 (a) have been made. The input parameters used in the calculations are shown in Table III. These inputs, together with the flux distribution curves, yield a curve of detector ion current vs. solid angle as shown in Fig. 34. A detector sensitivity of 1.3×10^{-18} A per molecule/cm^3 (ref. 50) (equivalent to 4.55×10^{-2} A/Torr) has been used in the calculations.

3.3 RETARDING POTENTIAL ENERGY DISTRIBUTION ANALYSIS

In its simplest form, the retarding potential energy analyzer consists of a plane parallel diode, one surface being the emitter and the other the collector. If the potential difference between the emitter and collector is positive or zero (for the case of electrons), the collector current is saturated and registers a constant value. As the potential difference is made more negative, fewer of the electrons have sufficient energy to penetrate the potential barrier and reach the collector. If a plot is then made of collector current vs. retarding potential difference, the result is an integral display of the energy distribution of the electrons, the slope of the curve being inversely proportional to the temperature of the emitter.

TABLE III

Input parameters for estimating the system sensitivity for the total density, flux angular distribution measurement.

1. $n_o = 10^{10}$ cm^{-3}
2. S = 11.7, 6.53
3. U = 4 x 10^5 cm/sec
4. T = 300°K , T_∞ = 1000°K
5. $d\omega = 10^{-3}$ sr

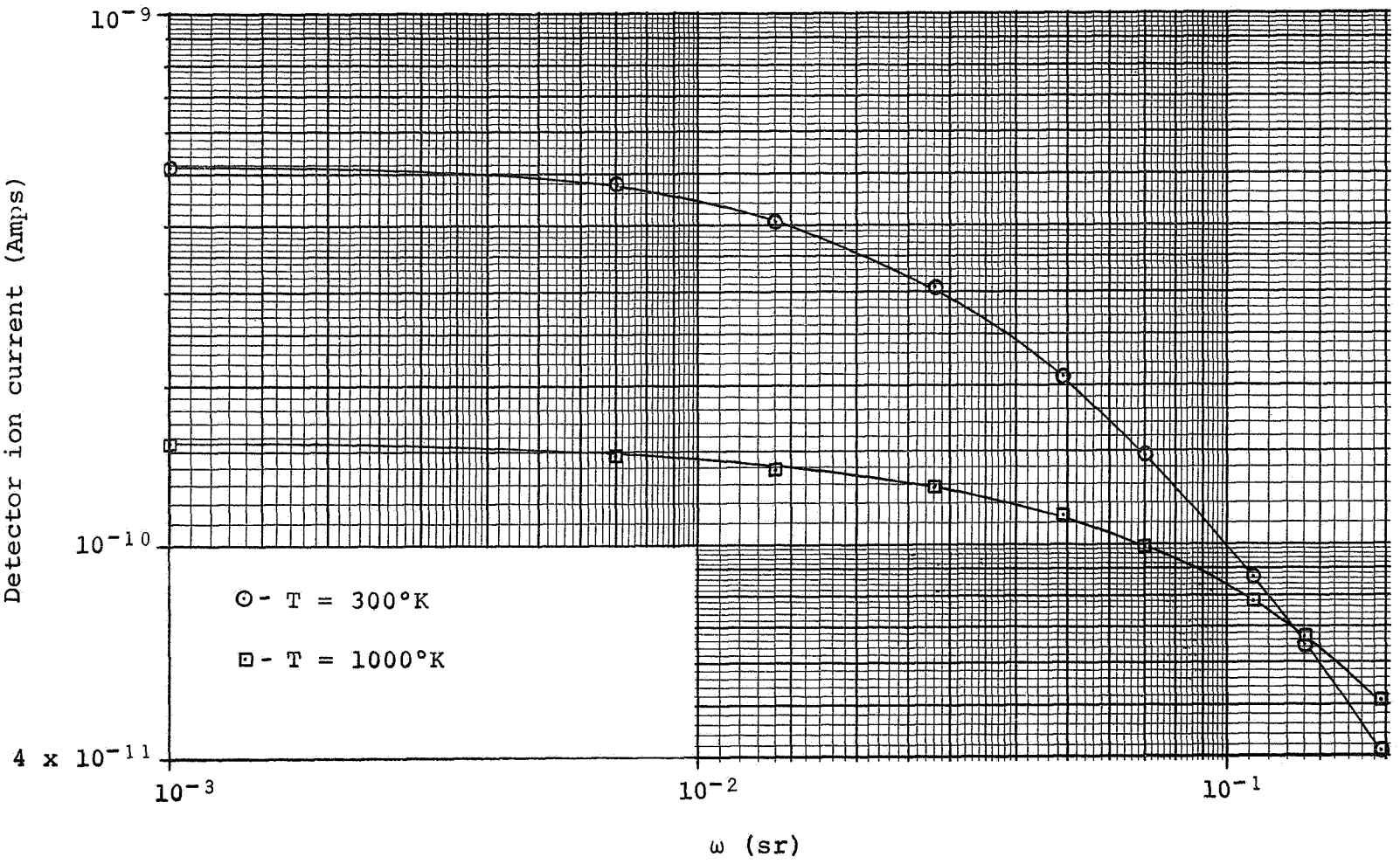

Fig. 34.- Detector current vs solid angle for a total density flight detection system.

The use of retarding potential methods for establishing the energy distribution of electron beams has been discussed in the literature, and the technique has been perfected sufficiently that quite accurate correlations between the temperature derived from the retarding potential data and direct measurements of the cathode temperature are found. However, the simplicity of the design and the accuracy does not completely apply when the same techniques are used to establish the temperature of an ion beam. Since the retarding potential technique affects only the axial component of the particle momentum, a means must be devised to reduce the effects of axial distortion of the energy distribution. This is usually accomplished, in the case of electron energy analysis, by applying an axial magnetic field of a few kilogauss. Such fields are neither practical in flight experiments nor effective for ion energy analysis. A practical solution is to use a total energy spectrometer, in which a converging-diverging lens system focuses the total flux into normal incidence on the plane of the retarding electrode. Discussions of a system and results obtained using this technique have been presented by Heil and Scott (ref. 12), both for electron and ion energy analysis. Factors influencing the electron energy resolution were lens aberrations, due to the finite extent of the source, the need of focusing particles of different energy, and field penetration through the openings in the retarding grid (screen). The energy resolution attained for the electron spectrometer was 10 meV, which corresponds to a temperature of approximately 50°K.

In the case of the ion energy spectrometer, an additional factor influencing the resolution is the effect of the electron space charge, which influences both the operation of the ion optical system and the energy of the particles as they arrive at the retarding electrode. This latter effect influences the establishment of the zero of the retarding voltage scale, which can be thought of as similar to the effect of the work function difference.

In applying the technique to the measurement of a cesium ion beam, Heil and Scott found that the temperature established from the retarding energy spectrum was 240°K lower than the temperature of the source. This difference is outside the limits of experimental error and the explanation for the result was not known.

The question of whether the effects of space charge actually change the velocity distribution of the ions with respect to the Maxwellian distribution of the neutral beam is not known with certainty and experimental evaluation of the effect of electron beams under varying conditions of space charge is required.

It is shown in Appendix A that for a 10^{-4} ampere electron beam of uniform density, having the dimensions characteristic of that required for space flight applications, the potential variation across the ion producing region is 0.15 volts. The uncertainty in temperature corresponding to this energy is 1800°K and the introduction of even a small fraction of that uncertainty into the ion production mechanism could lead to a distortion of the energy distribution of the molecules. These

space charge effects can be reduced by decreasing the ionizing electron current density. However, this results in a proportionally lower sensitivity and, thus, makes the retarding potential measurements less attractive than the previously discussed time-of-flight or flux distribution measurements.

4. DISCUSSION OF RESULTS AND CONCLUSIONS

The recent interest in the use of detection systems utilizing metastable energy states as opposed to ions is due not only to the fact that the neutral excited molecules are less susceptible to instrumental perturbations caused by stray electric and magnetic fields or charge distortion in general, but also that there is more selectivity in the production of a particular metastable gas species than there is for ion production. Since the production of metastables generally involves an electron exchange collision, the maximum cross-section occurs within a few tenths of an eV of threshold and decreases rapidly as the electron energy increases. This is to be contrasted with the broad maxima of the ionization cross-section. Additional discrimination in the production of metastables is possible due to the difference in energy separation of the metastable states from ground state for different gas species. In some cases, it is possible to selectively excite the components of a gas mixture by proper choice of the excitation energy. Furthermore, there is additional discrimination allowed at the detector when Auger detection is used. The possibility of capitalizing on these unique characteristics as applied to a detection system for probing the properties of planetary atmospheres, as evidenced by recent discussions in the literature,

provided additional stimulus for a thorough analysis of the technique and an evaluation of its applicability as a flight detection system.

This report presents the results of that feasibility study for establishing techniques to measure the atmospheric gas temperature in the Earth's thermosphere, although the techniques are not limited to that application. Primary emphasis was placed on the metastable time-of-flight technique, since little information is available to evaluate its applicability. However, two other methods, one based on the spatial distribution of the transmitted flux and the other based on the retarding potential energy spectrometer, were also investigated, since there is a need for defining techniques which produce direct or instantaneous measurements rather than indirect or inferred ones and which are applicable to the requirements of the variable operating conditions of anticipated flight experiments.

In deriving the expressions representing the signal of the MTOF detection system and the subsequent calculation of the signal for a specific molecular density, it was necessary to assign a value to the electron impact excitation cross-section and the secondary electron yield at the detector. In addition to other effects, both of these quantities are influenced by the large relative velocity of the vehicle; the high speed leads to a short flight time for the metastable molecules and, thus, an increased number of them which would otherwise have decayed by emission of photons will arrive at the detector and add to the total TOF signal. Since the excitation cross-section of these short-lived energy states (predominantly $E^3\Sigma_g^+$ and $a^1\pi_g$ and to a lesser degree $B^3\pi_g$) are such that they collectively add a

significant number of metastables to the high speed beam, it is to be expected that the total excitation cross-section would be greater than that for a thermal beam; thus, greater measurement sensitivity would also be attained. Based on the limited data available from Locke and French (ref. 10) on the total excitation cross-section-secondary electron coefficient product for a thermal beam of N_2 metastables, a comparison can be made between their value and that predicted for the high speed beam to see whether the estimated value is realistic. Locke and French report a value of 1.7×10^{-19} cm^2 for the total excitation cross-section-secondary electron coefficient product (designated as $Q\eta$ in ref.10) for an electron excitation energy of 9.8 eV and a "gas covered" tungsten detector. The corresponding estimated value (designated as $\sigma\gamma$) for the high speed beam for an electron excitation energy of 12 eV and a clean tungsten detector is 2.15×10^{-18} cm^2. For an oxygen covered tungsten detector, the estimated value is 6.0×10^{-20} cm^2. Thus, depending on the gas coverage, the estimated value may or may not be greater than that measured by Locke and French. Since the gas coverage was not specified by Locke and French, it is difficult to make a direct comparison; however, it is not unrealistic to expect that the increased excitation cross-section for the high speed beam, together with the increased secondary electron yield for a clean detector, would provide an order of magnitude increase in the sensitivity.

The selectivity of the MTOF detection system with regard to gas composition is a definite advantage for measurements in the thermosphere, since the measurements and the analysis can be treated as though the atmosphere were a single component gas. Therefore, the distribution established by the detection system is representative of the atmospheric temperature and is not distorted by the overlapping TOF signals of different molecular

weight components. The temperature resolution associated with the MTOF detection system was established in terms of the relative change of the pulse shape with temperature and was shown to be $\pm$ 5.5% over the range from 300-1000°K.

In those cases where the MTOF technique has inadequate sensitivity (i.e. measurements in the Martian atmosphere which is predominantly CO_2), some alternate detection scheme must be chosen. The flux distribution method, which is a total density detection system, was evaluated and the temperature measurement sensitivity and resolution were established for the same operating conditions as the MTOF system. In order to measure the temperature at an altitude of 170 km, the detector ion current would be approximately 10^{-10} amps and for 10% temperature resolution at this altitude (T = 850°K), the measurement of a change in the relative detector response of 10% is also required. As the density increases and the temperature decreases, both the ion current and the temperature resolution increase until at 300°K the resolution is such that for a 10% temperature change the relative detector response changes by 15%. Although knowledge of the probable error associated with a given relative detector output is required to indicate whether 10 or 15% changes in detector response can be adequately resolved, which involves an experimental evaluation of the detection instrumentation, one is left with considerable skepticism when anticipating such resolution in the 10^{-10}-10^{-11} ampere regions.

Likewise, an experimental evaluation of the effects of electron space charge on the ion energy resolution attainable with the retarding potential energy spectrometer is required before a final decision can be made regarding the temperature resolution which can be realized. However, even if resolution comparable

with the electron energy analysis is achievable, the temperature resolution is approximately $\pm$ 50°K.

Therefore, for measurements in the Earth's thermosphere, the MTOF detection system is seen to have the best temperature resolution of the methods evaluated. However, the other methods are suitable alternate choices, in particular when the MTOF system has inadequate sensitivity.

The advantages of atmospheric measurements based on the properties of an unscattered molecular beam as opposed to thermal equilibration measurements cannot be stressed too strongly and, although beam measurements are recognized as being plagued with low sensitivity, the flow properties and angular distribution of the beam flux for a high speed vehicle permit sensitivities which are greater than that associated with normal laboratory beams. It is concluded, as a result of the analyses presented in this report, that the detection systems discussed have sufficient sensitivity for measurements to approximately 170 km in the Earth's thermosphere. The certitude associated with the parameter evaluations is not known and, therefore, the next logical step in the evolution of a flight detection system would be the experimental verification of these parameters under conditions simulating the high speed vehicle environment, since the performance of the detection systems depend on, and are a result of, the high speed conditions.

APPENDIX A

Space Charge Potential Due To A Uniform Electron Beam

The following calculation provides an estimate of the magnitude of the space charge potential due to a uniform, cylindrical electron beam with operating parameters typical of those considered for a flight detection system. Consider the following beam geometry:

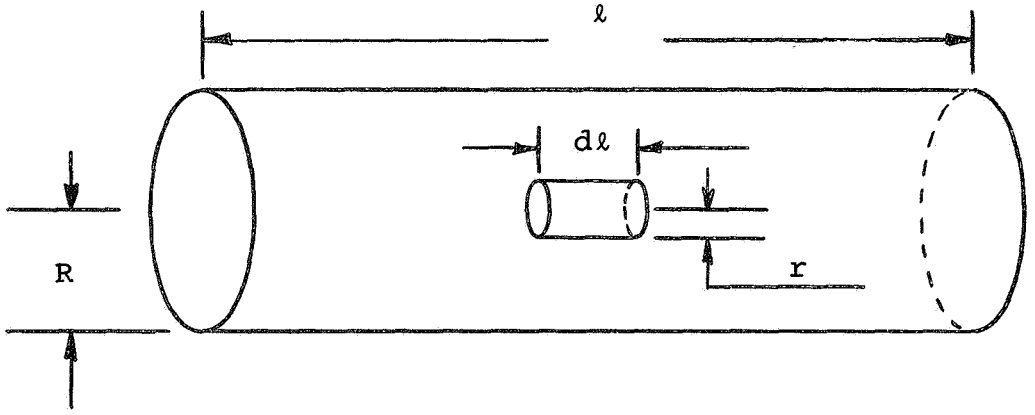

For a cylindrical Gaussian element located near the center of the beam (where its length $d\ell \ll \ell$), and because of the geometrical symmetry and the assumed uniform charge density, the only non-zero component of the electric field vector is E_r. Therefore, applying Gauss's Law yields

$$\int \bar{E} \cdot d\bar{s} = 4\pi q \qquad \text{(A-1)}$$

or

$$E_r 2\pi r d\ell = 4\pi\rho\pi r^2 d\ell \tag{A-2}$$

which reduces to

$$E_r = 2\pi\rho r \tag{A-3}$$

where ρ is the electron charge density. The gradient of the potential, dependent only on r, is

$$\bar{E} = -\nabla\phi \tag{A-4}$$

or

$$E = -\frac{d\phi}{dr} \quad . \tag{A-5}$$

Combining Eq. (A-3) and (A-5) and integrating from the center of the beam to R, the potential difference becomes

$$\Delta\phi = -\int_0^R 2\pi\rho r dr \tag{A-6}$$

or

$$\Delta\phi(R) = -\pi\rho R^2 \quad . \tag{A-7}$$

For a beam of uniform charge density, accelerated at a potential V_o, the total electron current becomes

$$i_e = \rho v_e A \tag{A-8}$$

or

$$i_e = \rho v_e \pi R^2 \quad . \tag{A-9}$$

However, equating the kinetic and potential energy, the electron velocity is

$$v_e = \left[\frac{2eV_o}{m_e}\right]^{\frac{1}{2}} \quad . \tag{A-10}$$

Substituting (A-10) into (A-9) and solving for ρ,

$$\rho = \frac{i_e m_e^{\frac{1}{2}}}{\pi R^2 (2eV_o)^{\frac{1}{2}}} \quad . \tag{A-11}$$

Therefore, using Eq. (A-11) and (A-7), it follows that

$$\Delta\phi(R) = i_e \left[\frac{m_e}{2eV_o}\right]^{\frac{1}{2}} \quad . \tag{A-12}$$

Using the following conditions, representative of parameters to be used in the detection system,

1. $i_e = 10^{-4}$ amperes
2. $V_o = 100$ volts

the potential difference from the center of the electron beam to that at R is calculated to be

$$\Delta\phi(R) = 0.15 \text{ volts} \quad . \qquad \text{(A-13)}$$

APPENDIX B

LIST OF SYMBOLS

$E(i\text{-}M)$	Interaction energy of an ion and a metal surface, eV.
$E(m\text{-}M)$	Interaction energy of a metastable and a metal surface, eV.
$E(n\text{-}M)$	Interaction energy of a neutral molecule and a metal surface, eV.
E_i	Ionization energy of a free molecule, eV.
E_i'	Effective ionization energy level, eV.
$E_k(e^-)$	Kinetic energy of ejected electrons, eV.
E_{th}	Threshold energy for electron ejection, eV.
E_x	Excitation energy of a free molecule, eV.
E_x'	Effective excitation energy level, eV.
e	Electronic charge, coul.
e^-	Free electron.
e_m^-	Metal electron.
dF	Differential flux, sec^{-1}.
$d\hat{F}$	Differential flux density, $cm^{-2}\text{-}sec^{-1}$.
$f(v)$	Maxwell-Boltzmann distribution function.
i_e	Electron current, amperes.

K	Attenuation coefficient.
k	Boltzmann constant, erg-$^{\circ}K^{-1}$.
L/D	Length-to-diameter ratio.
ℓ	Flight path length, cm.
m	Molecular mass, gm.
N^*	Number of metastables.
$\dot{N}^*$	Number of metastables per unit time, sec^{-1}.
n	Molecular density at the interaction region, cm^{-3}.
n_o	Atmospheric density, cm^{-3}.
n_i	Axial density of the transmitted flux, cm^{-3}.
P_c	Electron collision probability per unit path length, cm^{-1}.
$S \equiv U/v_m$	Speed ratio.
S/N	Signal-to-noise ratio.
s	Separation distance of metastable from a metal surface, cm.
s_c	Critical separation affecting the excitation energy levels of metastables, cm.
T	Gas temperature, $^{\circ}K$.
$T_g(S,X)$	Geometrical transmission function.

t	Flight time, sec.
dt	Detector delay gating interval, sec.
t'	Metastable drift time, sec.
Δt_e	Electron beam pulse duration, sec.
t_m	Time-of-flight corresponding to the maximum of the velocity distribution, sec.
U	Vehicle speed, $cm\text{-}sec^{-1}$
v	Particle velocity, $cm\text{-}sec^{-1}$
v'	Relative molecular velocity, $cm\text{-}sec^{-1}$
v_m	Most probable thermal molecular speed, $cm\text{-}sec^{-1}$
X	Ground state particle.
$X \equiv L/D$	Dimensionless length.
X^+	Ion.
X^m	Metastable molecule.
α	Angle of incidence, deg.
α, β	Fermi energy levels, eV.
γ	Total secondary electron yield.
γ_{kin}	Kinetic yield.
γ_{Pot}	Potential yield.
ε_F	Total depth of the Fermi energy levels, eV.
$\eta = K\gamma$	Detector sensitivity.

$\theta_o \equiv \tan^{-1} R/L$	Transmission angle.
λ_e	Electron path length, cm.
μ	Ratio of incident ion mass to target atom mass.
ρ	Electron pulse repetition rate, sec^{-1}.
σ	Total electron impact excitation cross-section, cm^2.
ϕ	Work function, eV.
$\phi \equiv \tan^{-1} D/L$	Transmission angle.
$d\omega$	Differential solid angle, sr.

REFERENCES

1. Schultz, F. V.; Spencer, N. W.; and Reifman, A.: Atmospheric Pressure and Temperature Measurement Between the Altitudes of 40 and 110 Kilometers, "Upper Air Research Program", Report 2, Engineering Research Institute, University of Michigan, July 1, 1948.

2. Patterson, G. N.: Theory of Free-Molecule Orifice-Type Pressures Probes in Isentropic and Nonisentropic Flows, UTIA Report 41, University of Toronto, 1956.

3. Hedin, A. E.; Avery, C. P.; and Tschetter, C. D.: An Analysis of Spin Modulation Effects on Data Obtained with a Rocket-Borne Mass Spectrometer, J. Geophys. Res., vol. 69, p. 4637, November 1964.

4. Niemann, H. B.; and Kreick, J. R.: Application of a Quasi-Open Ion Source for Neutral Particle Density Measurements in the Thermosphere, Scientific Report No. 3, Space Physics Research Laboratory, University of Michigan, 1966.

5. Nier, A. O.; Hoffman, J. H.; Johnson, C. Y.; and Holmes, J. C.: Neutral Composition of the Atmosphere in the 100-to-200 Kilometer Range, J. Geophys. Res., vol. 69, p. 979, 1964.

6. Hedin, A. E.; and Nier, A. O.: A Determination of the Neutral Composition, Number Density, and Temperature of the Upper Atmosphere from 120 to 200 Kilometers with Rocket-Borne Mass Spectrometers, J. Geophys. Res., vol. 71, p. 4121, September 1966.

7. Brock, F. J.: Feasibility Study of an Atmospheric Analysis Experiment, NASA-CR-66683, 1968.

8. Leonas, V. B.: A Possible Method for Measurement of the Temperature of the Upper Layers of the Atmosphere, Geomagnetism and Aeronomy, vol. 3, p. 465, 1963. Translation.

9. French, J. B.; and Locke, J. W.: A Time-of-Flight Velocity Analyzer Using Metastable Molecules, Proceedings 5th International Symposium on Rarefied Gas Dynamics, p. 1461, Oxford, 1966.

10. Locke, J. W.; and French, J. B.: A Critical Evaluation of the Metastable Time-of-Flight Technique for Obtaining Molecular Velocity Distributions, Presented at the 16th Annual Vacuum Symposium, Seattle, 1969.

11. Visentin, J.: Upper Atmospheric Neutral Particle Parameters Determination -- A Feasibility Study, Thesis Submitted to the University of Toronto.

12. Heil, J.; and Scott, B.: Temperature Measurements on Electron and Ion Beams, AD 643-532, 1966.

13. Hueser, J. E.; and Brock, F. J.: Development of a Gas Sampling System, Final Report, NAS1-5347 Task 15.

14. Ivanovskii, A. I.: Interaction Between an Instrument Cavity and a Flow of Rarefied Gas, Trudy Tsentral'noi Aerologicheskoi Observatorii, No. 56, pp. 49-96, 1964. Translation available CFSTI, AD658-028.

15. Kieffer, L.J.; and Dunn, G.H.: Electron Impact Ionization Cross-Section Data for Atoms, Atomic Ions, and Diatomic Molecules: 1. Experimental Data, Rev. Mod. Phys., vol. 38, p. 1, January 1966.

16. Francis, G.: Ionization Phenomena in Gases, Butterworths Scientific Publications, London, 1960.

17. Lichten, W.: Lifetime Measurements of Metastable States in Molecular Nitrogen, J. Chem. Phys., vol. 26, p. 306, February 1957.

18. Olmstead, III. J.; Newton, A.S.; and Street, Jr., K.: Determination of the Excitation Functions for Formation of Metastable States of Some Rare Gases and Diatomic Molecules by Electron Impact, J. Chem. Phys., vol. 42, p. 2321, April 1965.

19. Clampitt, R.; and Newton, A.S.: Studies on Electronically Excited Metastable States of Molecules with an Ultrahigh-Vacuum Molecular Beam Appraatus, UCRL-18032, CFSTI, December 1967.

20. Clampitt, R.; and Newton, A.S.: Surface Effects in the Ejection of Electrons by Electronically Excited Molecules, Surface Science, vol. 12, p. 92, 1968.

21. Freund, R.S.: Electron-Impact Excitation Functions for Metastable States of N_2 , J. Chem. Phys., vol. 51, p. 1979, September 1969.

22. Herzberg, G.: Molecular Spectra and Molecular Structure 1. Spectra of Diatomic Molecules, 2nd Edition, Van Nostrand, New York, 1951.

23. Freund, R. S.: Molecular-Beam Measurements of the Emission Spectrum and Radiative Lifetime of N_2 in the Metastable $E^3\Sigma_g+$ State, J. Chem. Phys., vol. 50, p. 3734, May 1969.

24. Stanton, P.N.; and St. John, R. M.: Electron Excitation of the First Positive Bands of N_2 and of the First Negative and Meinel Bands of N_2^+, J. Opt. Soc. Amer., vol. 59, p. 252, March 1969.

25. Zapesochyni, I. P.; and Skubenich, V. V.: The Cross Sections for the Excitation of Molecular Nitrogen Levels by Electron Collision, Opt. Spectrosc., vol. 21, p. 83, 1966.

26. Sheridan, J. R.; and Peterson, J. R.: De-excitation of Metastable Nitrogen Molecules in Collisions with N_2 and NO, J. Chem. Phys., vol. 51, p. 3574, October 1969.

27. Rempt, R. D.: Electron Impact Studies of Electron Capture and Excitation Near Threshold in Various Gases, AFCRL-69-0367, 1969.

28. McConkey, J. W.; and Simpson, F. R.: Secondary Effects in the Electron Impact Excitation of Nitrogen, Proceedings of VI ICPEAC, MIT, p. 419, 1969.

29. Green, A. E. S.; and Barth, C. A.: Calcualtions of Ultra-Violet Molecular Nitrogen Emissions from the Aurora, J. Geophys. Res., vol. 70, p. 1083, March 1965.

30. Stolarski, R.S.; Dulock, Jr., V.A.; Watson, C.E.; and Green, A.E.S.: Electron Impact Cross Sections for Atmospheric Species 2. Molecular Nitrogen, J. Geophys. Res., vol. 72, p. 3953, August 1967.

31. Holland, R.F.: Excitation of Nitrogen by Electrons: The Lyman-Birge-Hopfield System of N_2 , J. Chem, Phys., vol. 51, p. 3940, November 1969.

32. Kaminsky, M.: Atomic and Ionic Impact Phenomena on Metal Surfaces, Academic Press, New York, 1965.

33. Krebs, K.H.: Electron Ejection from Solids by Atomic Particles with Kinetic Energy, Fortschr. Phys., vol. 16, no. 8, p. 420, 1968.

34. Hagstrum, H.D.: Theory of Auger Ejection of Electrons from Metals by Ions, Phys, Rev., vol. 96, p. 336, 1954.

35. Hagstrum, H.D.: Auger Ejection of Electrons from Molybdenum by Noble Gas Ions, Phys. Rev., vol. 104, p. 672, November 1956.

36. Parker, Jr., J.H.: Electron Ejection by Slow Positive Ions Incident on Flashed and Gas-Covered Metallic Surfaces, Phys. Rev., vol. 93, p. 1148, March 1954.

37. MacLennan, D.A.; and Delchar, T.A.: Role of Work Function in Electron Ejection by Metastable Atoms: Helium and Argon on (111) and (110) Tungsten, J. Chem. Phys., vol. 50, p. 1772, February 1969.

38. Briglia, D.D.: Mass Spectrometer Studies of Ionization Processes in Nitrogen, AFCRL-64-259, AD 600 311, 1964.

39. Arifov, V.A.; Rakhimov, R.R.; and Dzhurakulov, Kh.: Secondary Emission in the Bombardment of Molybdenum by Neutral Atoms and Argon Ions, Soviet Phys. - Doklady, vol. 7, p. 209, September 1962.

40. Medved, D.B.; Mahadevan, P.; and Layton, J.K: Potential and Kinetic Electron Ejection from Molybdenum by Argon Ions and Neutral Atoms, Phys. Rev., vol. 129, p. 2086, March 1963.

41. Arifov, V.A.; and Rakhimov, R.R.: Variation of Ion-Electron Emission as a Function of Certain Parameters of the Target and the Bombarding Ions, Akad, Nauk S.S.S.R., Bull., Physic. Ser. 24, p. 666, 1960.

42. Magnuson, G.D.; and Carlston, C.E.; Electon Ejection from Metals due to 1-to 10-keV Noble Gas Ion Bombardment 1. Polycrystalline Materials, Phys. Rev., vol. 129, p. 2403, March 1963

43. Magnuson, G.D.; and Carlston, C.E.: Electron Ejection from Metals due to 1-to 10 keV Noble Gas Ion Bombardment II. Single Crystal, Phys. Rev., vol. 129, p. 2409, March 1963.

44. Fleischmann, H.H.; and Young, R.A.: Charge Production in Collisions Between Hydrogen Atoms and He, Ne, Ar, and H_2 in the Energy Range from 50-1000 eV, Phys. Rev., vol. 178, p. 254, February 1969.

45. Von Roos, O.: Theorie der Kinetischen Emission von Sekundärelektronen, Ausgelöst durch Positive Ionen, Z. Physik, vol. 147, p. 210, 1957.

46. Delchar, T. A.,; MacLennan, D. A.,; and Landers, A. M.: Adsorbate Effects in Electron Ejection by Rare-Gas Metastable Atoms, J. Chem. Phys., vol. 50, p. 1779, February 1969.

47. Berry, H. W.: Liberation of Electrons by Fast Neutral Helium Atoms from a Tungsten Target, J. Appl. Phys., vol. 29, p. 1219, August 1958.

48. Zorn, J. C.; and Pearl, J. C.: A Feasible Satellite Experiment for Gas Molecular-Solid Surface Interaction Studies, Final Report under NASA Contract NAS8-21096, The University of Michigan, 1968.

49. Scott, P. B.: Molecular Beam Velocity Distribution Measurements, AD614-230, 1965.

50. Knuth, E. L.; and Kuluva, N. M.: Performance of an Arc Heated Supersonic Molecular Beam and its Application to Molecule-Molecule Collision Studies, Recent Advances in Aerothermochemistry Vol. I, AD658-781, p. 277, 1967.

51. Alcalay, J. A.; and Knuth, E. L.: Molecular Beam Time-of-Flight Spectroscopy, Rev. Sci. Instr., vol. 40, p. 438, March 1969. See also Rev. Sci. Instr., vol. 40, p. 1652, December 1969.

52. Holt, H. K.; and Krotkov, R.: Excitation of n=2 States in Helium by Electron Bombardment, Phys. Rev., vol. 144, p. 82, April 1966.

53. Evans, R.: The Atomic Nucleus, McGraw-Hill Book Company, Inc., New York, 1955.

54. U. S. Standard Atmosphere Supplement, 1966.